Calibration and Validation of the RapidScat Scatterometer

Using Natural Land Targets

Nathan M. Madsen

A thesis submitted to the faculty of
Brigham Young University
in partial fulfillment of the requirements for the degree of

Master of Science

David G. Long, Chair
Brian A. Mazzeo
Shiuh-hua W. Chiang

Department of Electrical and Computer Engineering

Brigham Young University

September 2015

ABSTRACT

Calibration and Validation of the RapidScat Scatterometer
Using Natural Land Targets

Nathan M. Madsen
Department of Electrical and Computer Engineering, BYU
Master of Science

RapidScat is a Ku-band scatterometer that was launched September 2014 and is currently operating on the International Space Station. It estimates ocean vector winds through accurate measurement of the normalized radar coefficient (σ^0) of the ocean surface. In order to ensure the accuracy of σ^0 measurements and consistency with previous Ku-band scatterometers, post-launch calibration and validation is necessary. Calibration and validation is performed using natural land targets, namely the Amazon and Congo rainforests, to complement calibration efforts over the ocean. The σ^0 response of the targets is estimated with respect to viewing angle and time of year using previous Ku-band scatterometers. Taking advantage of the ISS orbit, the diurnal response of each target is estimated using RapidScat. Normalizing factors for incidence angle, azimuth angle, local time of day, and time of year are derived from these measured responses. RapidScat σ^0 measurements are found to be consistent throughout its mission life with instrumental drift less than 0.3 dB. The effectiveness of slice balancing is evaluated and found to be highly dependent on the pitch of the ISS. Understanding of the diurnal backscatter response and incidence response allow comparison of RapidScat measurements with measurements from the QuikSCAT, NSCAT, and Oceansat-II scatterometers. RapidScat σ^0 is found to be biased low compared to QuikSCAT by 0.1–0.3 dB.

Table of Contents

List of Tables

List of Figures

Chapter 1

Introduction

Wind scatterometers are space-borne radar systems designed to accurately measure the normalized radar cross-section (σ^0) of the earth. The primary application for these σ^0 measurements is vector wind retrieval over the ocean [5], but applications over both land and ice also exist.

Many scatterometers have operated since the launch of the Seasat scatterometer in 1978. Other NASA-built scatterometers include the NASA Scatterometer (NSCAT) in 1997, the SeaWinds scatterometer on QuikSCAT in 1999 and the SeaWinds scatterometer on ADEOS-II in 2002, all operating in the Ku-band. The next Ku-band scatterometer, the Oceansat-II scatterometer (OSCAT), was designed by the Indian Space Research Organization and was launched in 2009 [1].

In September 2014, the latest Ku-band scatterometer, RapidScat, was launched aboard a Falcon 9 rocket and mounted on the International Space Station (ISS), from which it is currently operating. RapidScat uses hardware originally created during the development of the SeaWinds scatterometer, so it is nearly identical to both of the previous SeaWinds scatterometers. Much of the processing software is also identical. The major difference between RapidScat and the previous SeaWinds scatterometers is the choice of platform. The nature of the ISS as a platform presents new challenges for accurate σ^0 measurement.

Post-launch calibration and validation are necessary to ensure that the scatterometer is working properly, and that its measurements are accurate and consistent with previous scatterometers. Considerable work has been done in calibrating and validating the retrieved vector winds over the ocean using in situ measurements, other sensors, and climate models. In this thesis, we focus on directly calibrating σ^0 using distributed land regions as

calibration targets. Measurements from these targets are used to validate the RapidScat σ^0 measurements and to cross-calibrate with other sensors.

Proper calibration and validation requires distinguishing variations in the target from biases and variation introduced by the instrument or σ^0 retrieval process. Even if relatively homogeneous and temporally stable regions are selected, there are still natural variations in the σ^0 response due to different factors. Measured σ^0 from various scatterometers are used to develop an empirical observation model that includes the response of our targets to such factors as, viewing angle, time of year, local time of day, and location within the mask. These models are then used during the calibration and validation of RapidScat.

Using RapidScat the diurnal component of the σ^0 response for natural land targets can be measured for the first time. This is due to the nature of its orbit. Previous wind scatterometers have all been placed in sun-synchronous orbits. As a result, they consistently measure σ^0 in low to middle latitudes at fixed local times for the entire mission. In contrast, the local time of day for RapidScat measurements is constantly changing, cycling through a full 24 hour cycle of local time every two months. This gives a unique opportunity for measuring diurnal cycles in σ^0 and the contributing geophysical processes. It also aids in calibration between sensors that take measurements at distinct local times.

Validation of RapidScat can be performed by comparing the behavior of RapidScat σ^0 measurements with behavior predicted by the observation model. Particular areas of concern are long term σ^0 drift and slice balancing. "Slices" are higher resolution σ^0 measurements created by applying range-Doppler processing to a measurement. Azimuthally dependent biases in the slice measurements were found when validating QuikSCAT [6] and so are also likely to be found in RapidScat. It is also necessary to check for consistency in σ^0 measurements with respect to attitude changes, an issue of particular import when the ISS is concerned.

Cross-calibration, by estimating instrumental biases, allows σ^0 datasets from different sensors to be used together in long-term studies. QuikSCAT is a good target for cross-calibration, because it has a decade long dataset and other Ku-band scatterometers have already been calibrated to QuikSCAT. The empirical observation model is used to com-

pensate for differences in the target response before estimating biases. The estimation of instrumental biases between QuikSCAT and RapidScat is a primary result of this thesis.

1.1 Thesis Statement

In this thesis, we use distributed natural land targets to validate RapidScat σ^0 and to estimate the relative calibration between RapidScat and QuikSCAT. Two targets in particular are selected, the Amazon and the Congo rainforests. These areas are selected because of their size, temporal stability, and homogeneity [7]. Spatial masks derived from QuikSCAT average σ^0 are used to define the targets.

The σ^0 response of the targets is estimated with respect to various factors by using different sensors. QuikSCAT with its long, consistent data record is used to estimate the seasonal σ^0 response. It is also used to evaluate the existence of an azimuthal response in the targets. Taking advantage of the orbit of the ISS, the diurnal cycle in σ^0 is evaluated using RapidScat. RapidScat and NSCAT are both used to estimate the incidence dependence of the target. Inter-dependencies are found to exist between the diurnal and seasonal cycles. These dependencies are used to create an empirical observation model.

Using the observation model, we evaluate the consistency of RapidScat σ^0 and estimate instrumental biases between RapidScat and QuikSCAT. Instrumental drift over the RapidScat mission is estimated to be less than 0.3 dB. Slice balancing is found to be effective for limited ranges of instrument pitch, but can have biases of several dB at extreme pitches. RapidScat σ^0 is estimated to be biased low compared to QuikSCAT by 0.1-0.3 dB.

1.2 Motivation

This thesis complements calibration and validation efforts over the ocean with calibration and validation using natural land targets. Validation will assure the scientific community that the RapidScat dataset is generally accurate and bring forward any considerations when using the dataset including long-term stability and slice balancing. Calibration between QuikSCAT and RapidScat will enable the continuation of the QuikSCAT σ^0 record. Comparison with other sensors will give the first estimates for instrument biases after taking into account local time of day. Understanding these biases will be a first step in creating

combined datasets of geophysical parameters from all the Ku-band scatterometers. This will facilitate research into multi-decadal trends in climate and geography.

1.3   Thesis Organization

We begin in Chapter 2 with background information on scatterometers, RapidScat, scatterometer calibration, and the datasets used in this thesis. RapidScat's unique ability to measure diurnal cycles is covered in Chapter 3. In Chapter 4, we define spatial masks for the target areas, and develop an observation model for the targets which includes variations with azimuth angle, incidence angle, location, local time of day, and time of year. These responses are used to arrive at several results in Chapter 5. Results include the discovery of imperfections in one of the data quality flags, estimation of instrument stability, evaluation of the slice balancing for varying pitches of the ISS, and estimation of mean biases between RapidScat and QuikSCAT. A conclusion is given in Chapter 6.

Chapter 2

Background

2.1 Scatterometers

Scatterometers are radars specifically designed to accurately measure the normalized radar cross-section (σ^0) of a distributed target such as the surface of the earth. They operate by transmitting a microwave pulse towards the surface and measuring the power scattered by the surface back to the scatterometer, as illustrated in Figure 2.1. The amount of power received from a given scatterer is a function of the incidence angle (θ), the azimuth angle, and the slant range to the target (R) in addition to the σ^0 of the target. The incidence angle and the azimuth angle determines the amount of antenna gain (for both transmit and receive) and range affects the amount of propagation loss (more range, more loss). These two terms can be used to define the spatial response function, which is the relative contribution of a point on the ground to the measured power [1].

These relations are summarized in the radar equation. The power received (P_r) is related to the average σ^0 of the target by:

$$P_r = \sigma^0_{\text{avg}} \frac{P_t}{(4\pi)^3} \iint \text{SRF}(x, y) \, dx \, dy,$$
$$\text{SRF}(x, y) = \frac{G(x, y)^2 F(x, y) g(x, y)}{R(x, y)^4}, \tag{2.1}$$

where SRF is the spatial response function, G is the antenna gain, R is the slant range to the target, and P_t is the transmitted power. Also note the inclusions of F and g in the equation for the SRF. F is a gain factor related to range-Doppler processing, and g is another term related to losses from range-gating. In practice, the integral can be solved ahead of time and stored in a look-up table [8]. An overview of the development of such a look-up table for
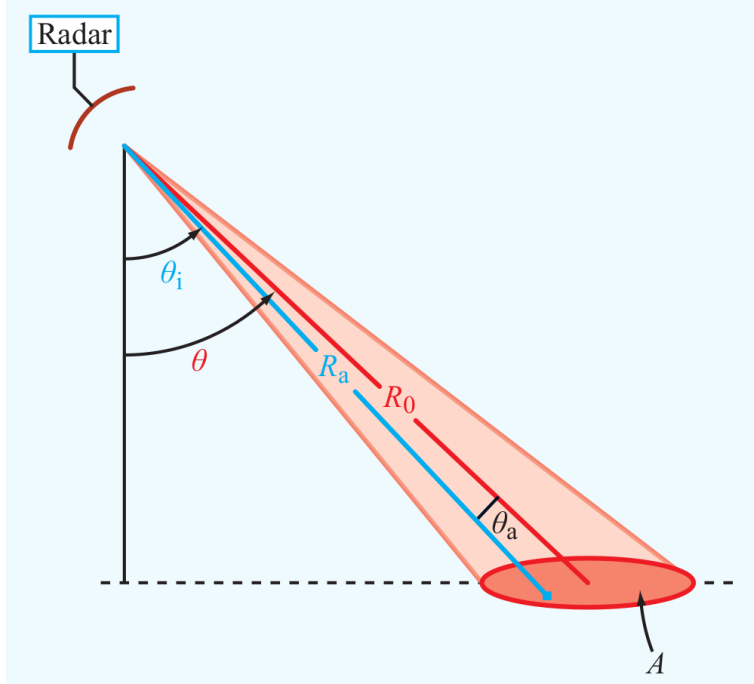
Figure 2.1: Measurement geometry for a radar [1].

RapidScat is given in Appendix A. The process of obtaining σ^0 from P_r is called σ^0 retrieval. Errors can occur in this process due to inaccuracies in the model or due to tabulation.

In this thesis, we deal exclusively with wind scatterometers. Wind scatterometers are space-borne scatterometers whose primary application is the retrieval of near-surface ocean vector winds [5]. Over the ocean, wind speed and direction can be inferred from σ^0 measurements. This is due to centimeter-scale capillary waves caused by the wind interacting with the ocean surface. Multiple measurements from different azimuth angles can be used to invert an empirical geophysical model function (GMF) that relates wind speed and direction to σ^0 [5]. These vector winds are used as inputs to weather models for forecasting [9–12] and specifically tropical cyclone tracking and prediction [13, 14]. Other geophysical parameters that can be estimated from scatterometer data include soil moisture [15], sea ice extent [16] and age [17,18], leaf area index [19], vegetation type [20,21], freeze-thaw cycles [22,23], snow accumulation [24,25], oil spills [26,27], and iceberg tracking [28].

An advantage of wind datasets from scatterometers as opposed to in situ measurements is coverage and consistency. A scatterometer dataset can last for years with a single

sensor. During that time, it covers almost the entire surface of the earth every day. It can make measurements without regard to cloud cover or local lighting conditions. This makes scatterometer datasets ideally suited to long term studies on the global scale.

2.2 RapidScat

RapidScat is the most recent scatterometer operated by NASA. It was preceded by the Seasat scatterometer in 1978, the NASA scatterometer (NSCAT) in 1997, the SeaWinds scatterometer on QuikSCAT in 1999 and the SeaWinds scatterometer on ADEOS-II in 2002, all operating in the Ku-band. The next Ku-band scatterometer, OSCAT, was developed by the Indian Space Research Organization and was launched in 2009. RapidScat continues the series of Ku-band scatterometers with its launch in 2014.

The primary goal of the RapidScat mission is to "demonstrate the agile reuse of flight-worthy hardware and demonstration of the capability to deploy and host a science class instrument" [29] while measuring global wind vectors. In keeping with this goal, the RapidScat instrument is actually a refurbished engineering model originally built during the development of the SeaWinds instruments. Much of the processing code is reused from the QuikSCAT mission. Instead of being mounted on its own platform, it is mounted on the International Space Station (ISS).

Though the RapidScat mission does not have specific science requirements, it does have science goals. These goals are: 1) enable cross-calibration for various scatterometers, 2) study diurnal cycles, and 3) provide wind data for weather models and storm forecasting. The third goal is standard for any scatterometer, but RapidScat is uniquely suited for the second goal, being the only scatterometer able to measure the full diurnal cycle as discussed in Chapter 3. This ability to measure the full diurnal cycle also supports the first goal, cross-calibration. Previous cross-calibration attempts were limited by potential differences due to local time of day of the measurement.

Another difference between the ISS and other scatterometer platforms is the inclination angle of its orbit. The ISS has an inclination angle of 51.65°. This limits the latitudes it can view to between $\pm 60°$ latitude. Previous scatterometers have all been in polar orbits where they covered almost the whole earth and, in particular, observed the polar regions

several times a day. This lent itself to various cryosphere related studies. These are not possible with RapidScat.

2.3 Calibration

Previous post-launch scatterometer calibration attempts using natural targets can be broadly divided into two types. The first is calibration over the ocean using vector winds, and the second is calibration over land using σ^0 measurements [30, 31].

Calibration over the ocean using vector winds has advantages and disadvantages. The first advantage is the size of the ocean; no other calibration target can come close. Larger targets mean more samples for comparison. Also vector winds are a geophysical parameter that is not specific to the characteristics of the sensor. This means that it can be compared with winds measured by other sensors such as buoys and scatterometers in other frequency bands. A disadvantage is that wind changes quickly. Collocated measurements with small time displacements are rare between different scatterometers and limited to polar regions due to the nature of most scatterometer orbits [31]. Instead of using collocated measurements, winds can be compared with global numerical weather models such as ECMWF [32], though this relies on the accuracy of the weather model. Winds are also the primary parameter of interest in scatterometry so their calibration and validation is an important outcome.

Calibration over land using σ^0 also has its own advantages and disadvantages. Unlike the ocean, the backscatter response of a land target is typically temporally stable [7]. There is relatively little variation from measurement to measurement. However, differences in the local time of day of measurements can create biases between measurements from different sensors [33]. Also in calibration over land, the σ^0 measurements themselves are being calibrated. This is a disadvantage in that it limits cross-calibration to other sensors with similar system characteristics, in particular, frequency. On the other hand using σ^0 ensures that the σ^0 measurements themselves are accurate. Calibrating using only winds can end up calibrating to the geophysical model function giving accurate winds but not necessarily accurate σ^0 measurements which are necessary for the estimation of other geophysical parameters. In practice, absolute calibration of σ^0 is not feasible due to the complexity of the targets. As a result, cross-calibration of σ^0 between sensors is performed. This allows for continuous

8

σ^0 data records between different sensors by calibrating different sensor measurements to a single reliable sensor.

Calibration and validation for scatterometers using natural land targets and specifically the Amazon rainforest have been performed for much of the history of scatterometry. The Amazon rainforest was first proposed as a calibration target in [34] after considering measurements from the Seasat scatterometer and Skylab. Studies of other potential calibration targets using Seasat data was performed in [35]. The Amazon rainforest response has been used to propose time, beam, and cell dependent corrections for Seasat data in [36]. The Amazon rainforest has also been used in beam balancing for NSCAT [30, 37], beam and slice balancing in QuikSCAT [6, 38], inter-calibration between QuikSCAT and SeaWinds on ADEOS-II [39], and inter-calibration between QuikSCAT and OSCAT [40, 41]. In most of these studies another region is used in addition to the Amazon to confirm the results from the Amazon.

2.4   Datasets

Datasets from three different scatterometers are used for calibration in this thesis. Each sensor and its dataset have unique characteristics that allow the study of backscatter response with respect to different variables.

The earliest dataset is from the NASA Scatterometer (NSCAT). NSCAT was launched in August 1996 aboard the Japanese Advanced Earth Observing Satellite [29] and operated until June 1997 to yield a 10 month dataset. NSCAT operated at 13.995 GHz in the Ku band and has a fan-beam configuration for its antennas. A fan-beam scatterometer has multiple beams at fixed azimuth angles each covering a wide range of incidence angles. The long antenna footprint is divided using Doppler processing. The measurement geometry is shown in Figure 2.2. There are 8 beams at six distinct azimuth angles, four on either side of the flight path. It can be noted that there are not any beams directly perpendicular to the flight path because Doppler processing is used to define finer resolution cells. Another point to note is that antennas 1, 3, 4, and 6 cover higher incidence angles than antennas 2 and 5. These higher incidence angles are those covered by RapidScat V-pol so beams 2V and 5V are not used for RapidScat calibration. NSCAT operated in a sun-synchronous orbit
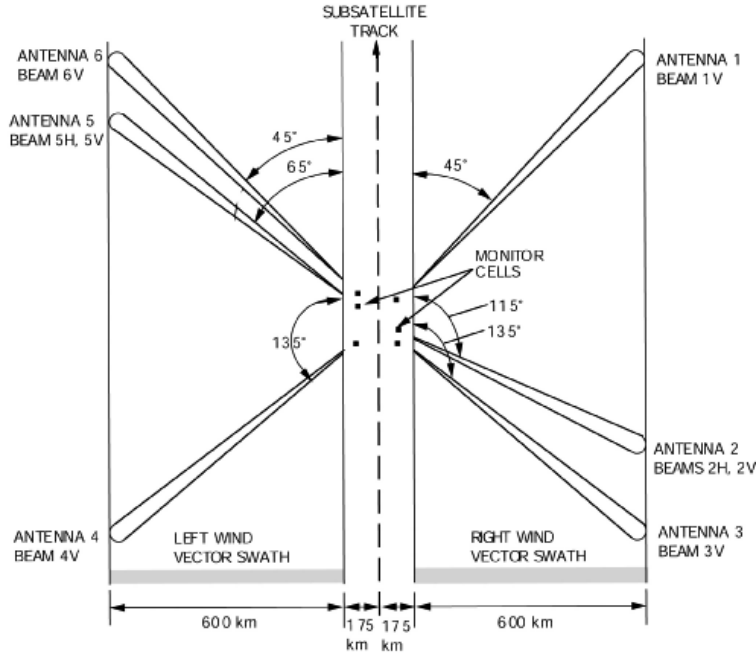
Figure 2.2: Measurement geometry for NSCAT [2].

that crossed the equator at 10 p.m. local time for ascending passes and 10 a.m. local time for descending passes. The level 1.5 data (time ordered σ^0 measurements) from the entire mission is used for analysis done in this thesis.

The next dataset considered comes from QuikSCAT. QuikSCAT was a "quick recovery" mission to compensate for the loss of NSCAT. It was launched in June 1999 and measured winds until November 2009 when the antenna stopped scanning due to a mechanical failure. This makes QuikSCAT's dataset the longest continuous dataset available. QuikSCAT operates at 13.4 GHz and had two rotating pencil-beam antennas at fixed incidence angles, 46.25 degrees for the horizontally polarized (H-pol) beam and 54 degrees for vertically polarized beam (V-pol) as seen in Figure 2.3. Like NSCAT, QuikSCAT has a sun-synchronous orbit, crossing the equator at 6 a.m. and 6 p.m. local time for ascending and descending passes respectively [29]. The level 1B data (time ordered σ^0 measurements) from the entire mission is used for analysis done in this paper.

After November 2009 QuikSCAT entered what is termed post-wind mission (PWM) mode. Though unable to scan in azimuth, it continues to accurately measure σ^0 with a much narrower but denser swath. This data, though not well-suited to wind retrieval, still provides
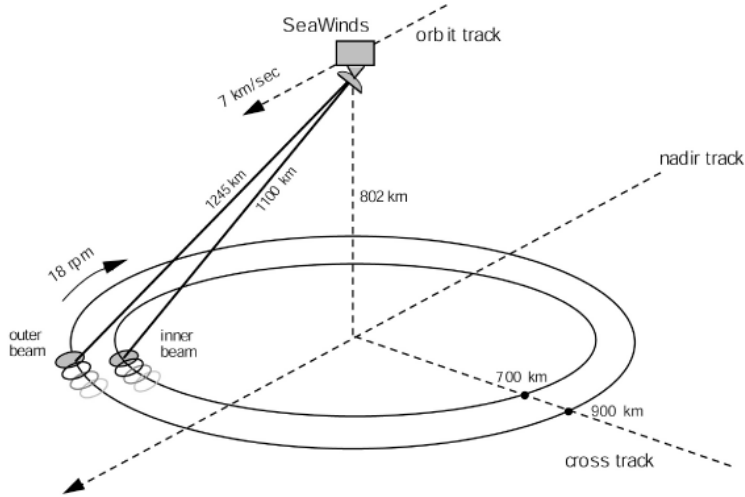
Figure 2.3: Measurement geometry for QuikSCAT [3].

Table 2.1: Time coverage, incidence angles, and azimuth angles of the QuikSCAT PWM data available at BYU. Listed incidence angles are average incidence angles over the listed data for H-pol and V-pol. Azimuth angles are average azimuth angles measured over ascending and descending passes (clockwise from north).

Start Day	End Day	Inc. H	Inc. V	Azi Asc	Azi Des
160, 2011	263, 2011	46.25	54.00	38.46	236.35
263, 2011	82, 2012	62.37	62.35	38.09	236.31
148, 2013	309, 2013	48.98	57.67	219.63	56.49
98, 2014	295, 2014	47.75	55.60	219.61	56.44

accurate measurements of σ^0. The instrument has been adjusted to different attitudes for months at a time to give σ^0 measurements at different incidence and azimuth angles [42]. The data used is provided by JPL in the form of "Repointed QuikSCAT files". It is to be noted that these files have considerably fewer measurement in a given time period when compared to corresponding level 1B files.

The last dataset comes from RapidScat. RapidScat was launched in September 2014 and is currently operational. The instrument hardware is almost identical to QuikSCAT since it was originally built as an engineering model for QuikSCAT. The primary differences in the RapidScat and QuikSCAT datasets is due to the nature of RapidScat's platform. RapidScat is mounted on the International Space Stations (ISS) which was not designed

11

specifically to host RapidScat. The ISS is not in a sun-synchronous orbit, meaning that the local time of day for measurements changes with each orbit. The local time of day of RapidScat measurements is discussed further in Chapter 3. Another feature of the ISS is the attitude. The RapidScat instrument is not directly pointed at nadir, so as it scans in azimuth, the incidence angle changes as well. Also, as the ISS attitude changes the range of measured incidence angles change as well. This behavior is shown in Figure 2.4.

The RapidScat dataset is ongoing. Unless otherwise, mentioned the analysis is performed using "nrt_delayed" level 1B data from revolution 161 (4 Oct. 2014) to revolution 3933 (3 Jun. 2015). Only data flagged as usable from revolutions classified by JPL as "good" are used.

Where appropriate, for each sensor the data is divided into four "flavors" depending on the polarization/beam and whether the measurement was taken during an ascending or descending pass. Division based on polarization/beam is because each beam could have its own biases and the σ^0 response for a target varies with polarization of the incident beam. Ascending and descending passes are measured at different local times of day, which could cause differences in the response of the target.

Each dataset can be used to understand how backscatter responds to different variables. Due to its fan beams, NSCAT naturally measures backscatter over a range of different incidence angles with every pulse. RapidScat can measure the full diurnal response unlike any of its sun-synchronous predecessors. QuikSCAT, with a long dataset at fixed incidence angles and fixed local times of day, can provide good estimates of seasonal variations. Differences in the datasets are summarized in Table 2.2.
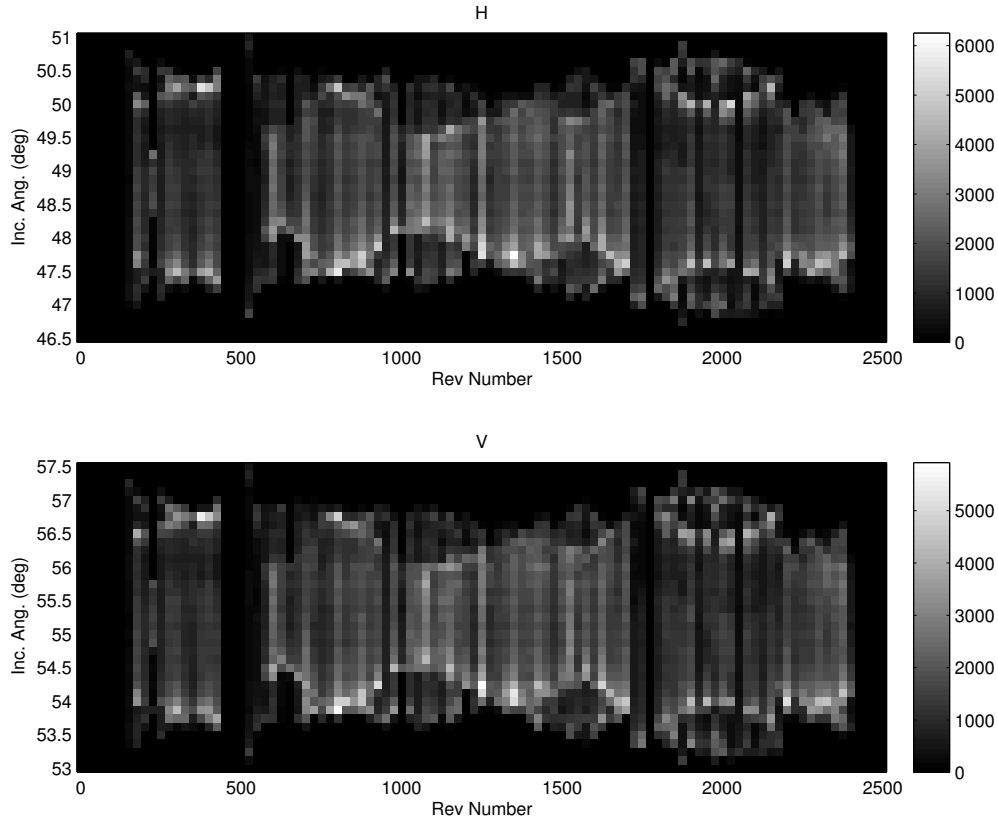
Figure 2.4: Histogram of incidence angle for different revolutions over the Amazon throughout the RapidScat mission. Top is horizontally polarized. Bottom is vertically polarized.

Table 2.2: Summary of key features of each scatterometer and its dataset. Local time is the local time for at the equator crossings.

Parameter	NSCAT	QuikSCAT	QuikSCAT PWM	RapidScat
Duration	Aug 1996 - Jun 1997	Jun 1999 - Nov 2009	Nov 2009 - Present	Sep 2014 - Present
Frequency	13.995 GHz	13.4 GHz	13.4 GHz	13.4 GHz
Incidence Ang.	10° - 55°	46.25° H 54° V	Various	47-50.5° H 53-57° V
Azimuth Ang.	Fixed	All	Various	All
Local Time	10 p.m. Asc 10 a.m. Desc	6 a.m. Asc 6 p.m. Desc	6 a.m. Asc 6 p.m. Desc	All

13

Chapter 3

Local Time of Day Measurement

RapidScat is the first wind scatterometer capable of measuring σ^0 at all local times of day for low to middle latitudes. This is because prior wind scatterometers have all been placed in sun-synchronous orbit. A sun-synchronous orbit always views certain latitudes at fixed local times of day. RapidScat is not in a sun-synchronous orbit and so the measurement local time of day varies over time. In the following sections, we review the orbital mechanics of sun-synchronous orbits and how RapidScat in particular can measure diurnal cycles.

3.1 Orbital Mechanics

A sun-synchronous orbit is an orbit whose orbital plane precesses around the earth exactly once per year. The precession is due to the oblateness of the earth and is governed by the following equation:

$$\Delta\Omega = -2\pi\frac{J_2}{\mu p^2}\frac{3}{2}\cos(i), \tag{3.1}$$

where $\Delta\Omega$ is the angular precession per orbit, J_2 is a term related to the oblateness of the earth, μ is the gravitational constant of the Earth, p is the semi-latus rectum of the orbit, and i is the inclination of the orbit. When an orbit is selected such that $\Delta\Omega$ divided by the orbital period is 360° per year the orbit is termed sun-synchronous. An example sun-synchronous orbit and orbit with no precession are shown in Figure 3.1 [43].

As can be seen in Figure 3.1, the orientation of the sun-synchronous orbit with respect to the sun is constant. At any given point in the satellite's orbit the sun is at approximately the same position relative to the satellite and the earth. This means that the local time of day on the earth's surface below is approximately the same. For example, when QuikSCAT crosses the equatorial plane heading northward (the ascending node), the local time is 6 a.m. for every revolution. Likewise, when it crosses the equator heading southward (the
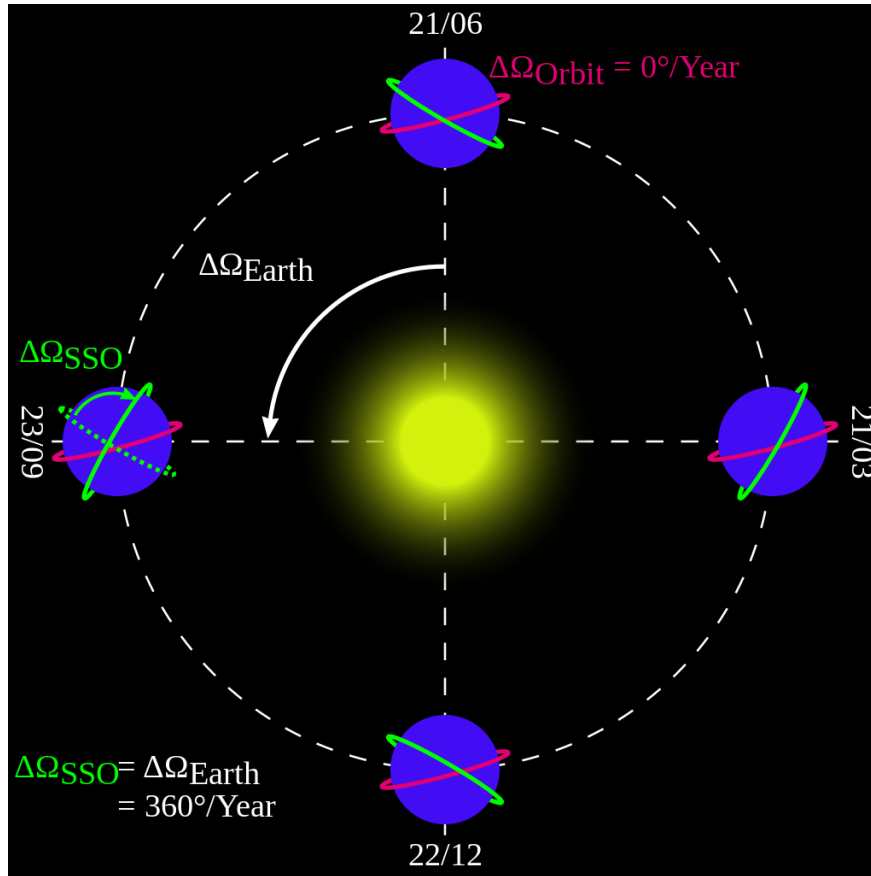
Figure 3.1: An illustration of the orbital planes for a sun-synchronous orbit (green) and an orbit without precession (red) [4].

descending node) the local time is 6 p.m. for every revolution throughout its mission. These orbits are often chosen for earth observing satellites to provide consistency to the dataset, at the expense of the possibility of diurnal studies.

In general though, sun-synchronous orbits are the exception. If the rate of precession is anything but 360° per year the local time of day varies. If there is no precession (for example, if the inclination angle is exactly 90°) then the local time of the ascending node and any other position in the orbit goes through a full 24 hour cycle in a year. Different values for the precession result in the local time of day changing more or less quickly.

3.2 RapidScat Local Time of Day Measurement

The ISS on which RapidScat is mounted is not in a sun-synchronous orbit. In fact, the orbital precession is in the opposite direction as that for QuikSCAT. The precession and
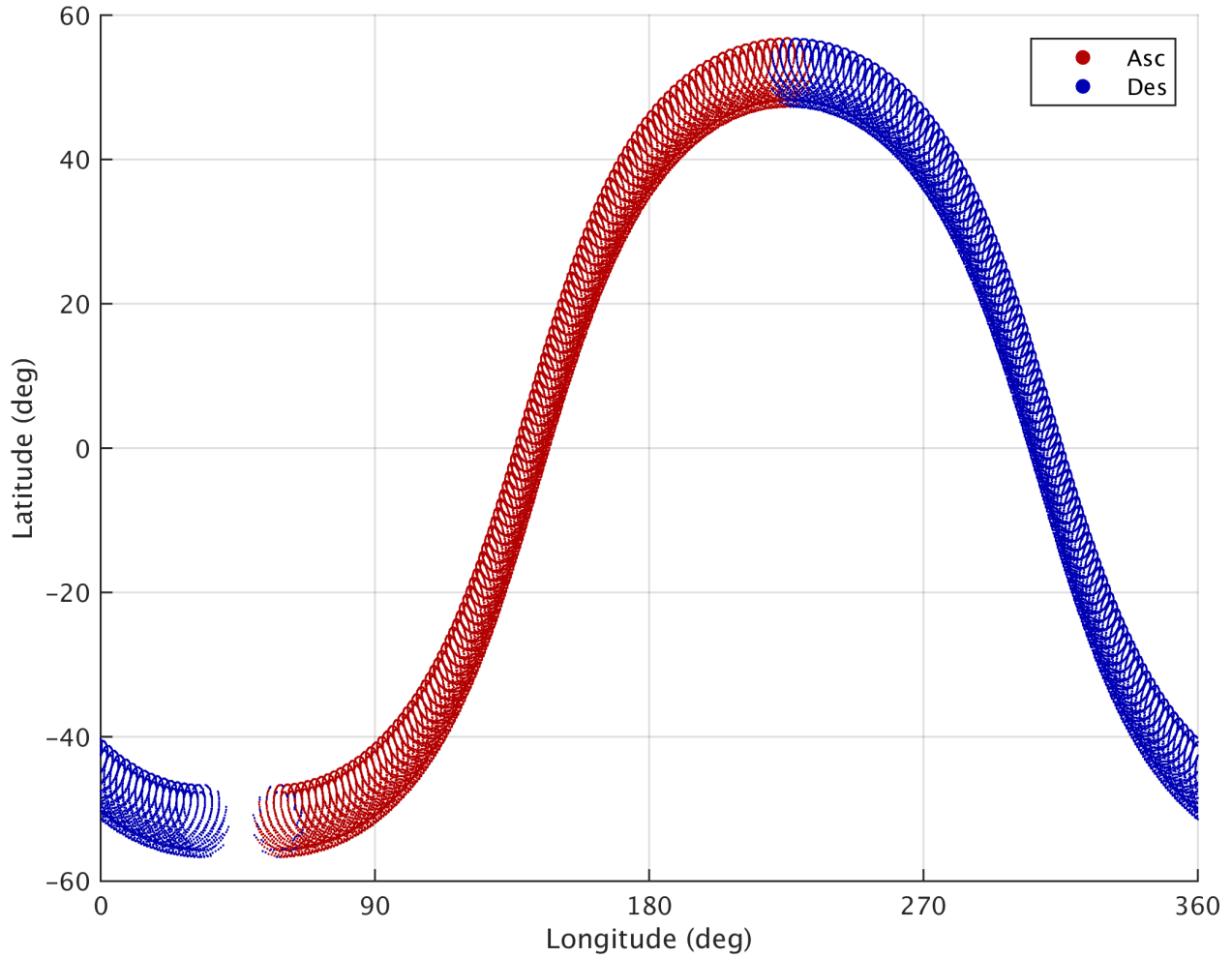
Figure 3.2: Latitudes and longitudes of every 25th sample from revolution 01192 of RapidScat.

the revolution of the earth around the sun combine to produce a complete precession with respect to the sun every two months. This implies that the local time for a particular point in the ISS orbit goes through a 24 hour cycle every 2 months.

In a single revolution, RapidScat scans the surface of the earth starting in the southern hemisphere, crosses the equator heading north, reaches the high point of its orbit, then returns to the south at a different longitude as seen in Figure 3.2. The change in longitude is primarily a result of the earth's rotation. RapidScat repeats this orbit 14 times per day. Over a single day, RapidScat covers most of the earth's surface between 60° S and 60° N latitude as the earth rotates beneath it.

Within a single day the orbit does not precess much, nor does the earth move much with respect to the sun. As a result, within a single day the orbital plane has a similar position with regard to the sun and each position in the orbit has a corresponding local time of day. Most latitudes are viewed from two distinct positions in the orbit for each revolution, one in the ascending pass and one in the descending pass. For latitudes near the equator these passings are separated by about 12 hours local time as shown in Figure 3.3(a). At higher latitudes the local times for the ascending and descending passes come together until they become the same time at the highest longitudes measured by the sensor. This is shown in Figures 3.3(b) and 3.3(c). This behavior is the same whether the latitude increases in the northern or southern direction. On a longer time scale, as the orbit precesses and the earth revolves around the sun, the local time of day for viewing at each latitude goes through a two month cycle.

The two-month cycle in local time of day is unique to RapidScat among wind scatterometers. With this cycle in local time of day, RapidScat is the first scatterometer capable of measuring the full σ^0 diurnal cycle. Various diurnal geophysical mechanisms can affect the σ^0 response of a target. Examples of such mechanisms over land include evapotranspiration, dew formation, and leaf orientation [44]. Measurements of diurnal σ^0 cycles can provide insight into these geophysical phenomena on a global scale.

Understanding diurnal cycles of σ^0 is also of interest for calibration and validation of scatterometer systems. Previous scatterometers each made measurements at distinct times of day. When comparing measurements between different sensors during previous calibration attempts there has been an unknown diurnal σ^0 dependency. RapidScat can measure the diurnal dependence of calibration targets allowing us to distinguish between relative instrument biases and diurnal biases in the calibration target.
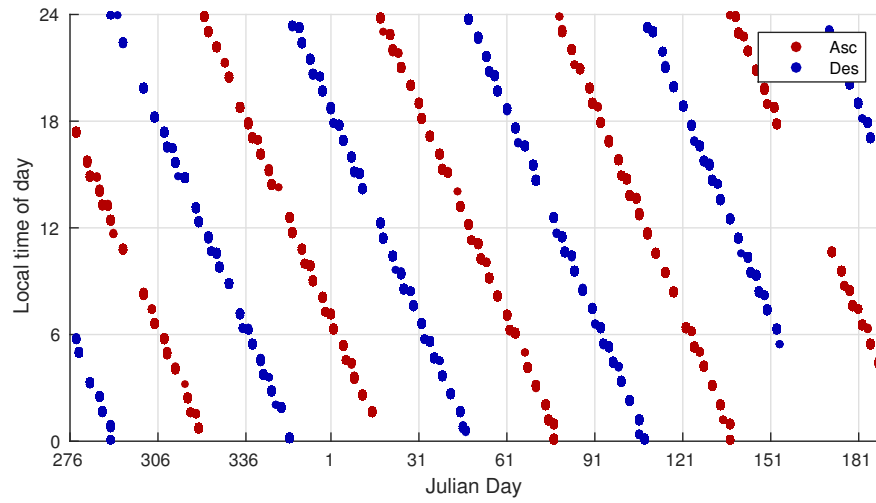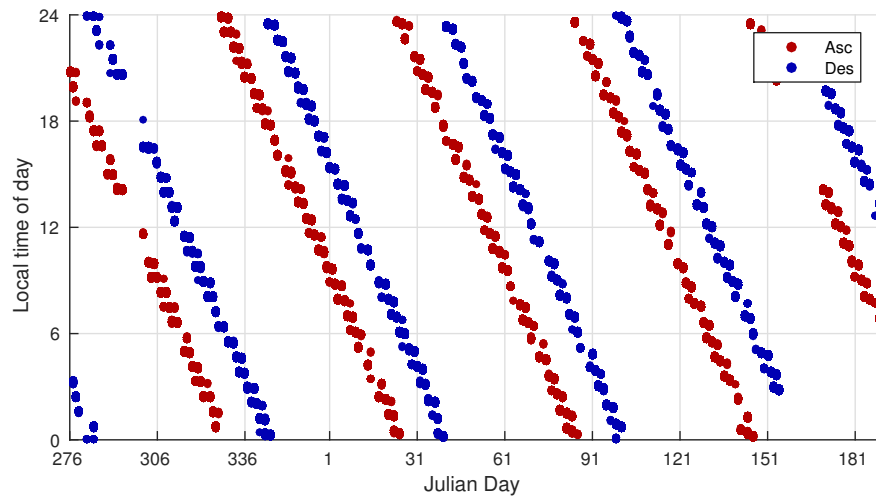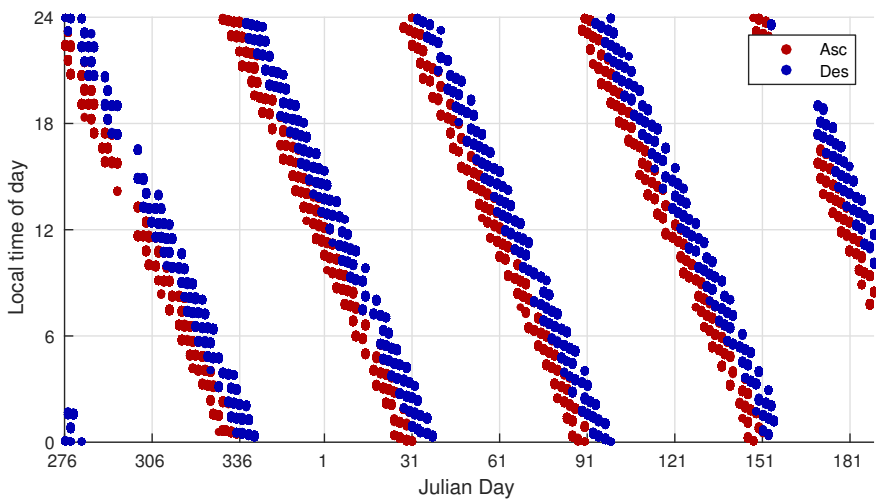
Figure 3.3: Local time of measurements for 2° latitude by 2° longitude regions over the RapidScat mission life. (a) is for a region at the equator, (b) is for a region at 40° N latitude, and (c) is for a region at 50° N latitude.

19

Chapter 4

Observation Model

The goal of calibration and validation is to estimate biases in RapidScat. Biases can be a function of the antenna beam, time of measurement, incidence angle, and azimuth angle. Ideally these biases would be identified by comparing σ^0 measurements to the true σ^0 of a target with known scattering characteristics. However, such a target does not exist.

Instead distributed, natural, land targets are used. Natural targets, like instrument biases, vary with time, incidence angle, and azimuth angle. A distributed land target also has spatial variations within itself. In order to isolate variations in the target from biases in the instrument, targets are selected for which these variations are relatively small, well understood, or both. These dependencies can not be determined analytically so they are empirically estimated using various scatterometers.

Likewise, the absolute calibration cannot be analytically determined, so a single scatterometer's measurements are chosen to be "truth." For this thesis, we use QuikSCAT σ^0 as a truth value. QuikSCAT operated for an unequaled 10 years in wind mission mode and continues to operate in post wind mission mode. QuikSCAT has been noted for being consistent throughout its mission [40]. The goal is a relative calibration by estimating the average bias between QuikSCAT and RapidScat σ^0. This will provide consistency with the QuikSCAT dataset as well as other sensors that have been calibrated to it, enabling long-term studies.

The discussion above is summarized into an observation model. We begin with the model development in [36]. A measurement from the target can be modeled as the "true" σ^0 with biases and noise,

$$\sigma^0_{\text{meas}} = \sigma^0_{\text{true}}(\theta, \phi, t) + B(b, t, \theta, \phi) + n, \tag{4.1}$$

where σ_{meas}^0 is the σ^0 measurement and σ_{true}^0 is the "true" normalized radar cross-section of the target and a function of the incidence angle θ, the azimuth angle ϕ, and the time of the measurement t. B is a bias term due to retrieval errors and instrument hardware biases and is a function of the beam b and the time of the measurement, incidence angle, and azimuth angle. The last term n is a zero-mean noise term which stems from retrieval errors and instrument noise. Each of these terms in in decibels. This reflects the multiplicative nature of variations with viewing angle or time.

In the view of Equation 4.1, the goal becomes to select a target, estimate the function $\sigma_{\mathrm{true}}^0(\theta, \phi, t)$ and compare that with σ_{meas}^0 as measured by RapidScat, and then estimate $B(b, t, \theta, \phi)$. In the following sections, we select two targets and then create empirical models for their "true" σ^0 response.

4.1 Target Selection

For a distributed calibration target there are three characteristics in particular that are desirable: homogeneity, size, and temporal stability. By homogeneity it is meant that the entire target has a similar backscatter response both in magnitude and in how it changes with respect to other factors. Homogeneity is balanced by size. Increasing the size of the target gives more samples for comparison, but also may result in including areas that are less homogeneous. Temporal stability allows comparison of temporally disjoint samples. Tropical rainforests have these attributes as noted in [7, 34, 36, 39, 40]. In this thesis, we specifically use the Amazon rainforest and the Congo rainforest.

The calibration target regions are defined by creating a spatial mask. In mask creation, the competing demands of homogeneity and size must be balanced. We follow the examples in [36, 37] by selecting a region that has a 1 dB range of mean σ^0. The mean σ^0 is determined by using high-resolution σ^0 images generated with the SIR algorithm [45] from QuikSCAT data. Images from the entire QuikSCAT mission are averaged together to generate a single σ^0 image for each of the four "flavors" of QuikSCAT data, namely: H-pol ascending passes, V-pol ascending passes, H-pol descending passes, and V-pol descending passes. The average image of the Amazon for H-pol ascending passes is shown in Figure 4.1.
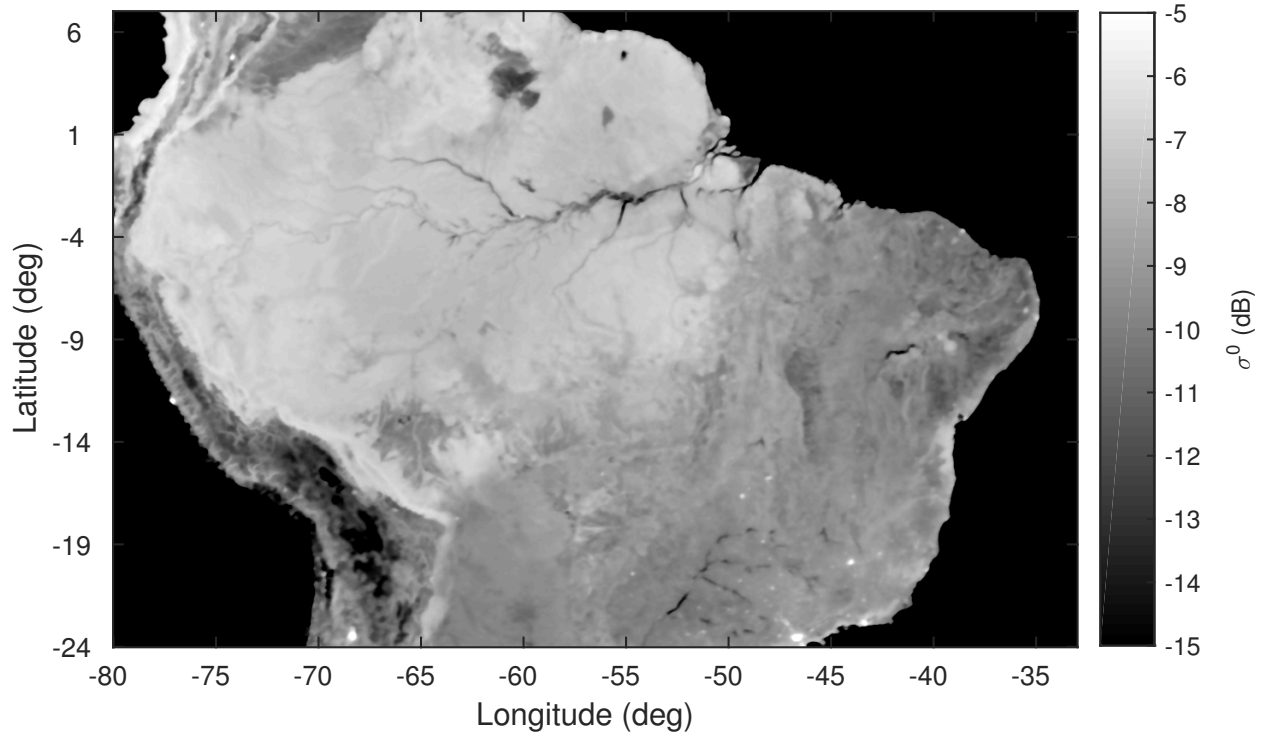
Figure 4.1: Average measured σ^0 over QuikSCAT mission life. Note the higher σ^0 over the Amazon rainforest. Only H-pol Ascending passes were used.

After generating the average images, a single pixel is selected from within the rainforest and the σ^0 value of that point is taken. All pixels with σ^0 within ±0.5 dB of that value are then selected and the mean σ^0 of the selected pixels is calculated. With this new mean σ^0, a new region is selected and the average is taken again. Iterating this process tends toward the largest area that fits within a 1 dB range of average σ^0. It can be visualized as moving the average till it reaches the peak of the histogram shown in Figure 4.2. This process is performed for each of the four "flavors" resulting in four masks. The iterative process also results in all four masks being extremely similar. The final spatial mask is composed of the points that fall within all four masks. The final masks for the Amazon and Congo are shown in Figures 4.3 and 4.4 respectively. In both masks features such as river and lakes are masked out, yielding a mask covering a homogeneous area.

The masks are applied to the data conservatively. With NSCAT data each cell measurement comes with latitude and longitude pairs corresponding to the center of the cell and four corners. Only if all 5 of these points fall within the mask is the measurement kept.

23
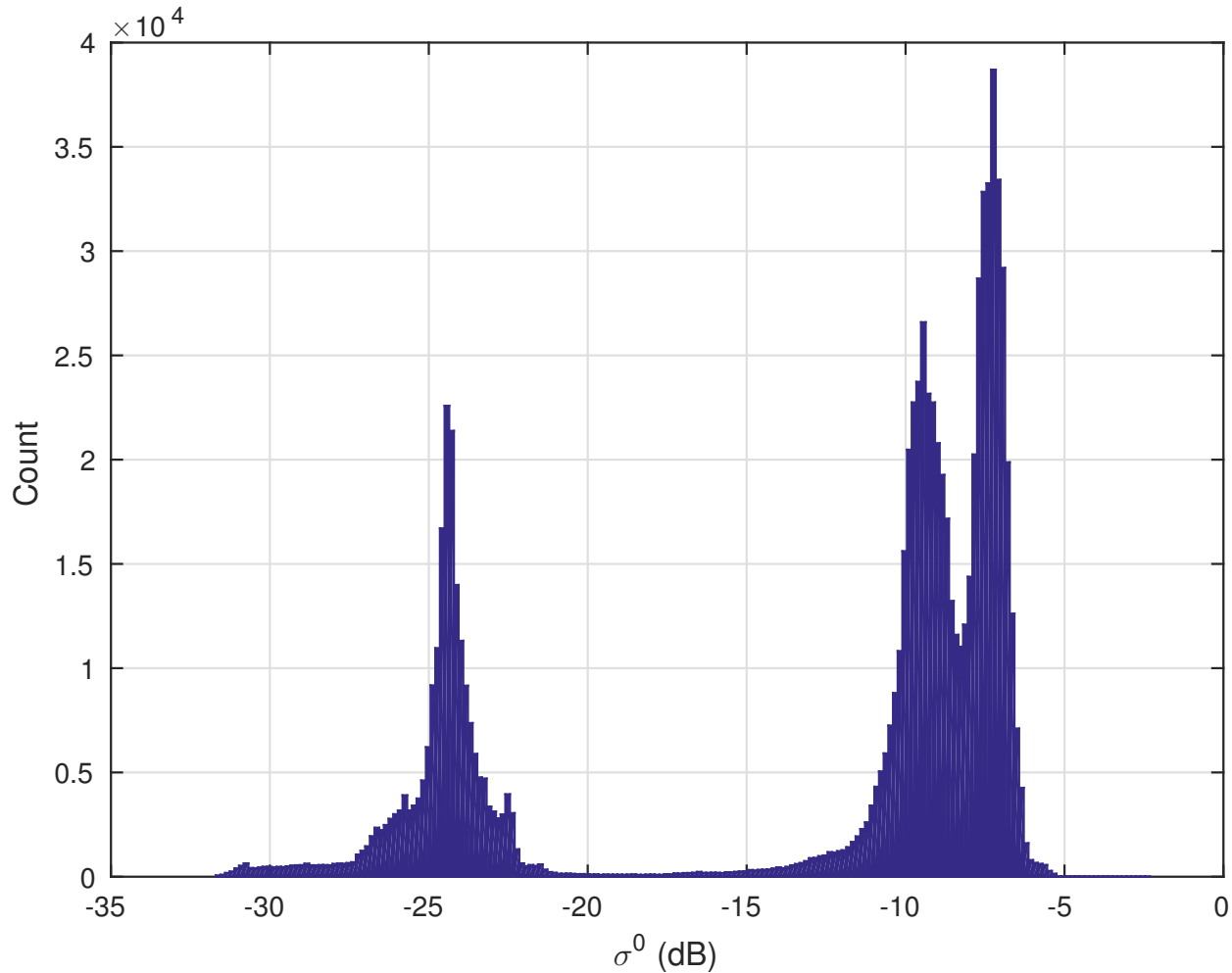
Figure 4.2: Histogram of QuikSCAT H-pol σ^0 averages in Figure 4.1. Note the peak at about -7 dB corresponding to the Amazon rain forest. The other two peaks are non-rainforest land and ocean.

With QuikSCAT, OSCAT, and RapidScat the center of each cell measurement as well as the center of each slice are reported. If all of these fall within the mask, the measurement is kept. This helps to ensure that only measurements entirely in the mask are used in the calibration process.

4.2   Azimuth Dependence

Previous studies such as [34, 36, 38] have shown that the Amazon rainforest is considered azimuthally isotropic. This can be confirmed for our Amazon and Congo masks by using the QuikSCAT dataset. QuikSCAT has a ten year record that is very stable and so can
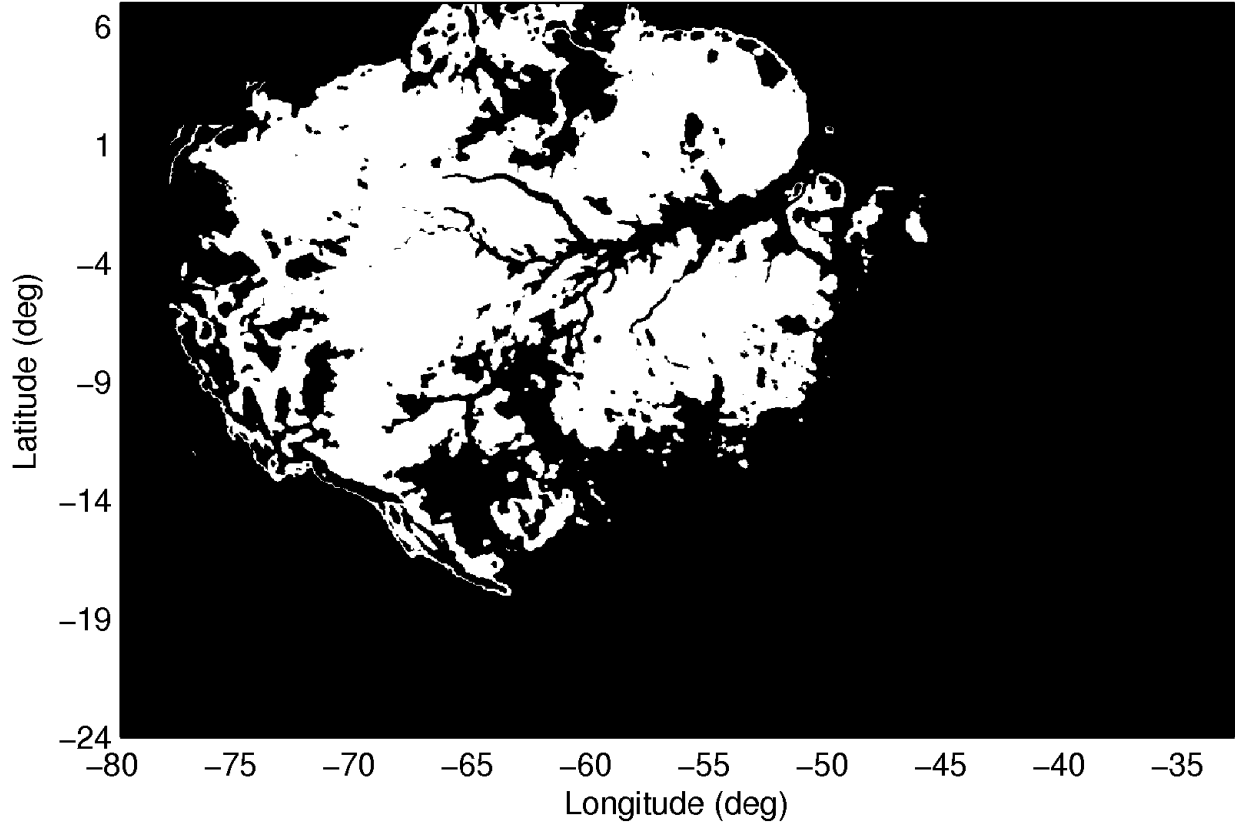
Figure 4.3: Final mask used for Amazon region.

be used to estimate the azimuth dependence very accurately. The average azimuth responses over the QuikSCAT mission for the Amazon and Congo are shown in Figures 4.5, 4.6, 4.7, and 4.8. Figures 4.5 and 4.6 show the antenna azimuth angle which is measured from a fixed reference direction relative to the sensor. Figures 4.7 and 4.8 is measured from local north and so is fixed with respect to the target.

From these four figures, three important points can be noted. First is the magnitude. The difference between the peak azimuth response and the trough is about 0.1 dB. This is very small and is within the range of acceptable error for scatterometer measurements. The second thing to note is the positions of the peaks and troughs of the overall pattern. They correspond more closely between ascending and descending passes in Figures 4.5 and 4.6 where the azimuth is measured relative to the spacecraft. This suggests that the larger general trend is related more to the instrument than the target. These findings agree with [6] where it is stated that the azimuth imbalance was found to be less than 0.1 dB so no

25
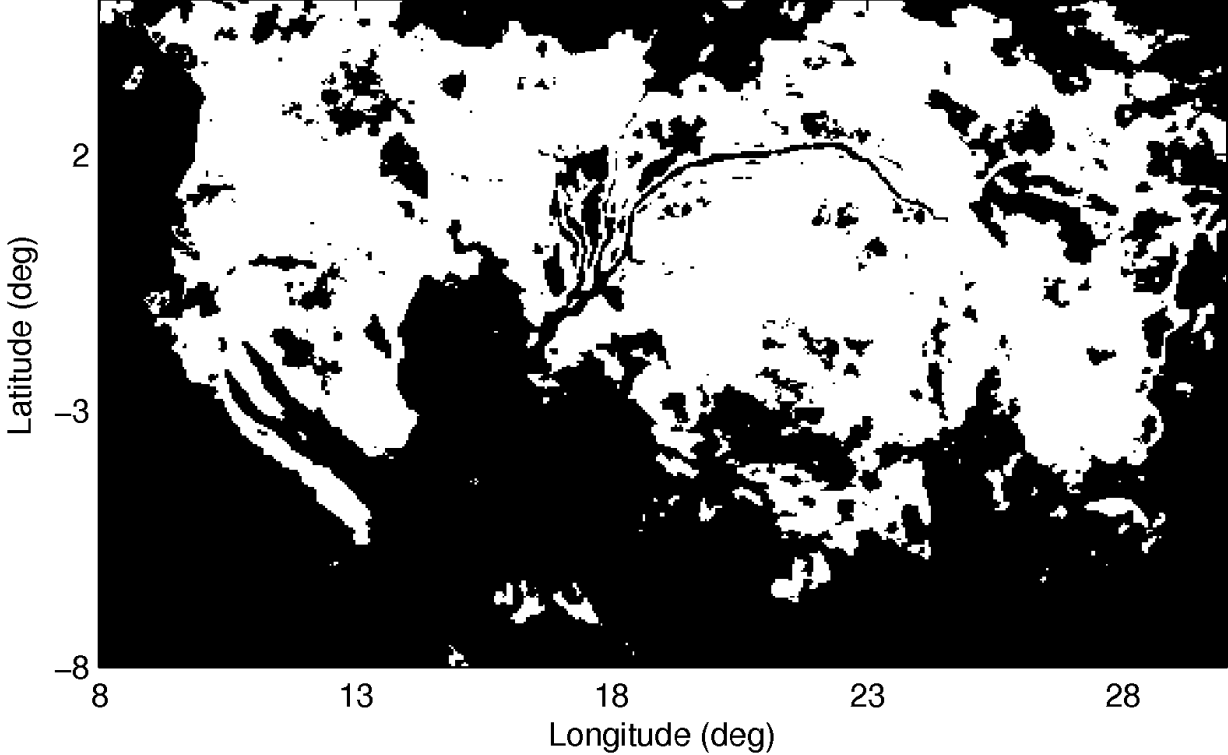
Figure 4.4: Final mask used for Congo region.

corrections were made to the QuikSCAT data record. Thirdly, though the overall trends are largely a function of antenna azimuth, there are also differences in the azimuth dependence for ascending and descending passes, and there is structure in the differences for each time of year. It is unlikely that instrumental biases have a distinct seasonal pattern, indicating that likely there is some azimuthal dependence in the target itself.

Considering how small the azimuth dependence is, we assume for the sake of calibration that the Amazon and Congo are azimuth independent. Fortunately, sampling is relatively uniform in azimuth even for small sample sizes so most azimuth dependence can be eliminated by averaging. As such, we can revise our observation model in Equation 4.1 by removing the azimuth dependency in the bias and the target response:

$$\sigma_{\mathrm{meas}}^0 = \sigma_{\mathrm{avg}}^0(\theta, t) + B(b, t, \theta) + n + \eta, \tag{4.2}$$
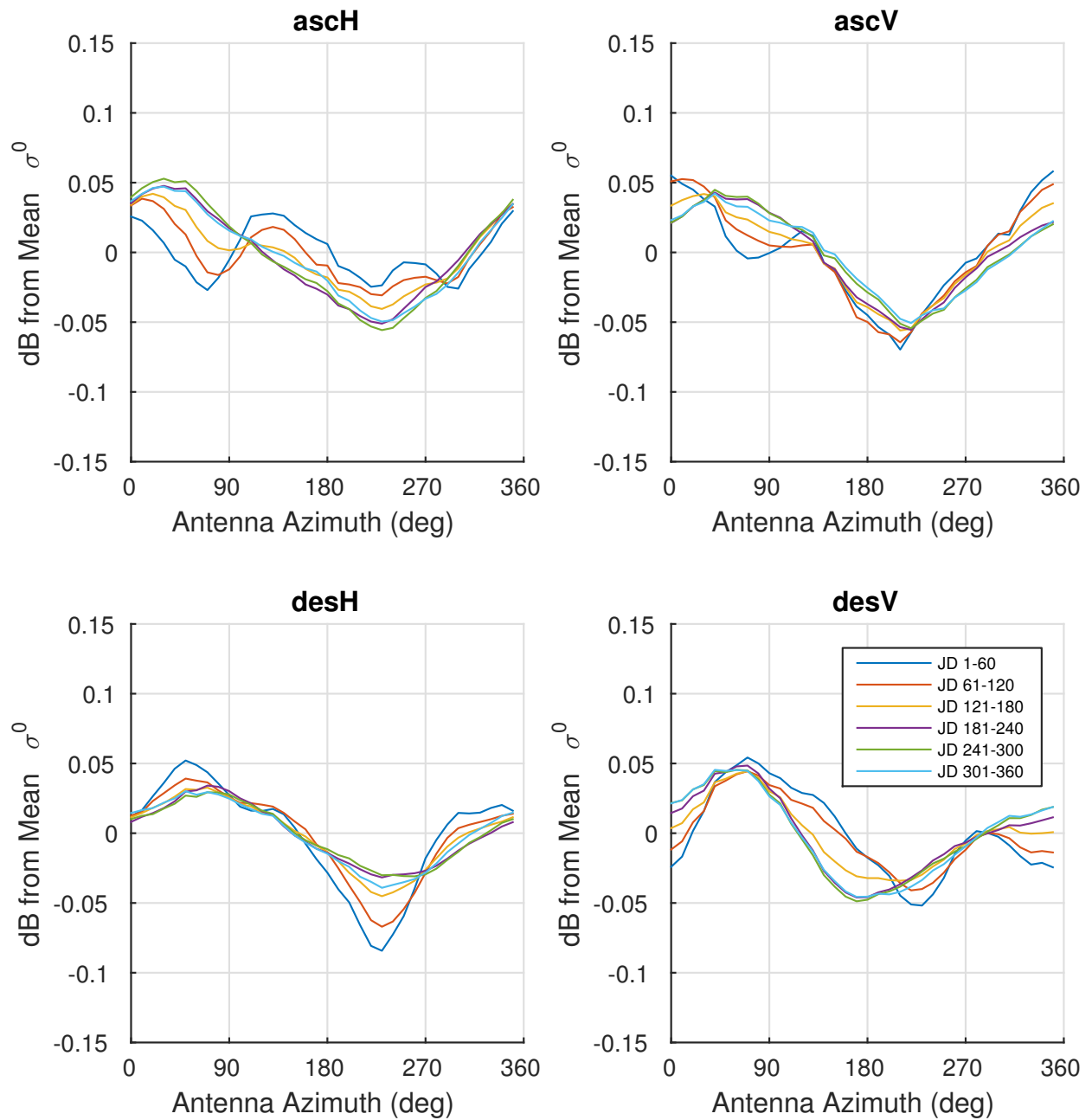
Figure 4.5: Azimuth σ^0 response of the Amazon rainforest. Separate lines shown for different times of the year. Azimuth angle is measured clockwise from a fixed direction relative to the sensor.
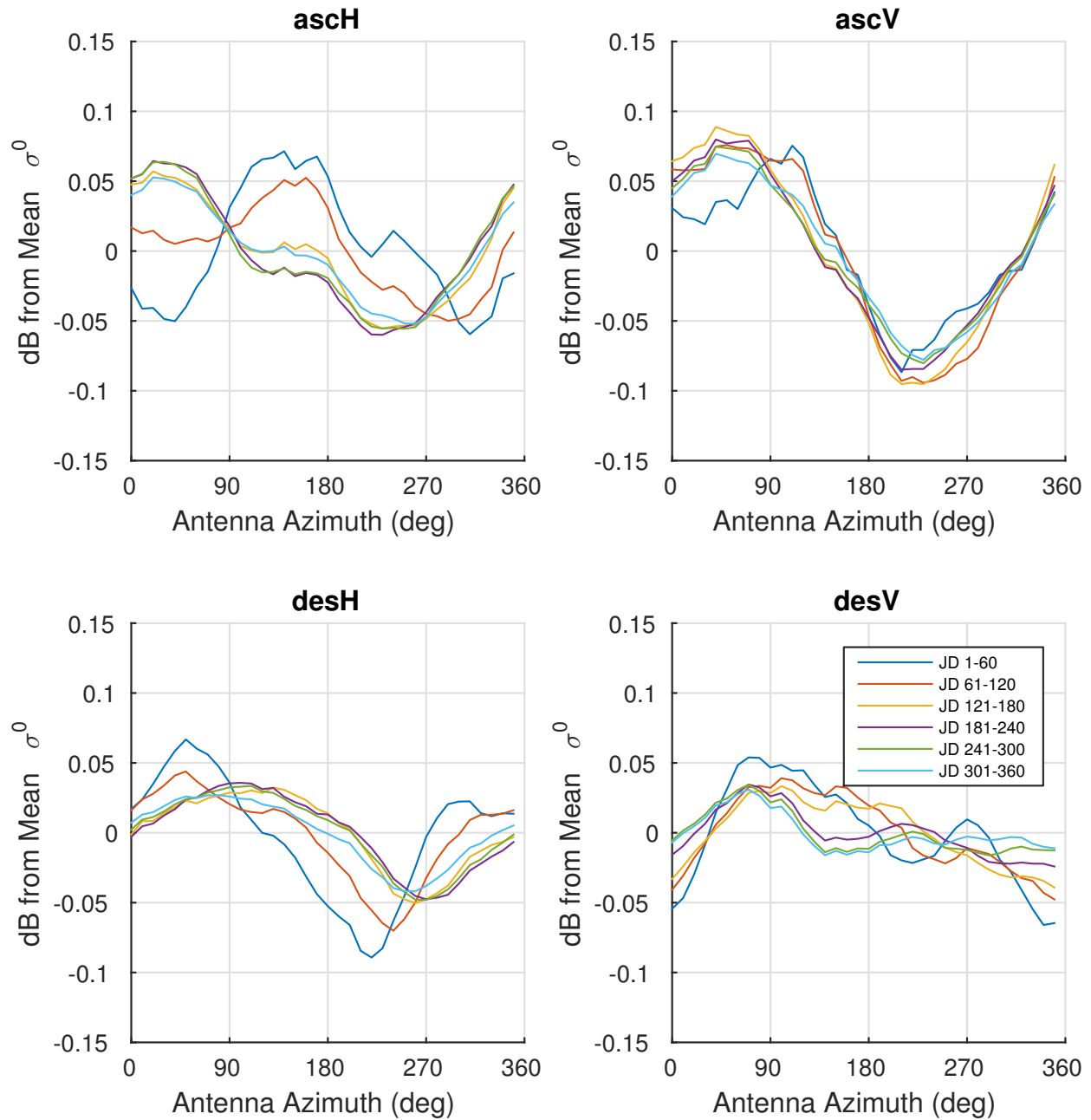
Figure 4.6: Azimuth σ^0 response of the Congo rainforest. Separate lines shown for different times of the year. Azimuth angle is measured clockwise from a fixed direction relative to the sensor.
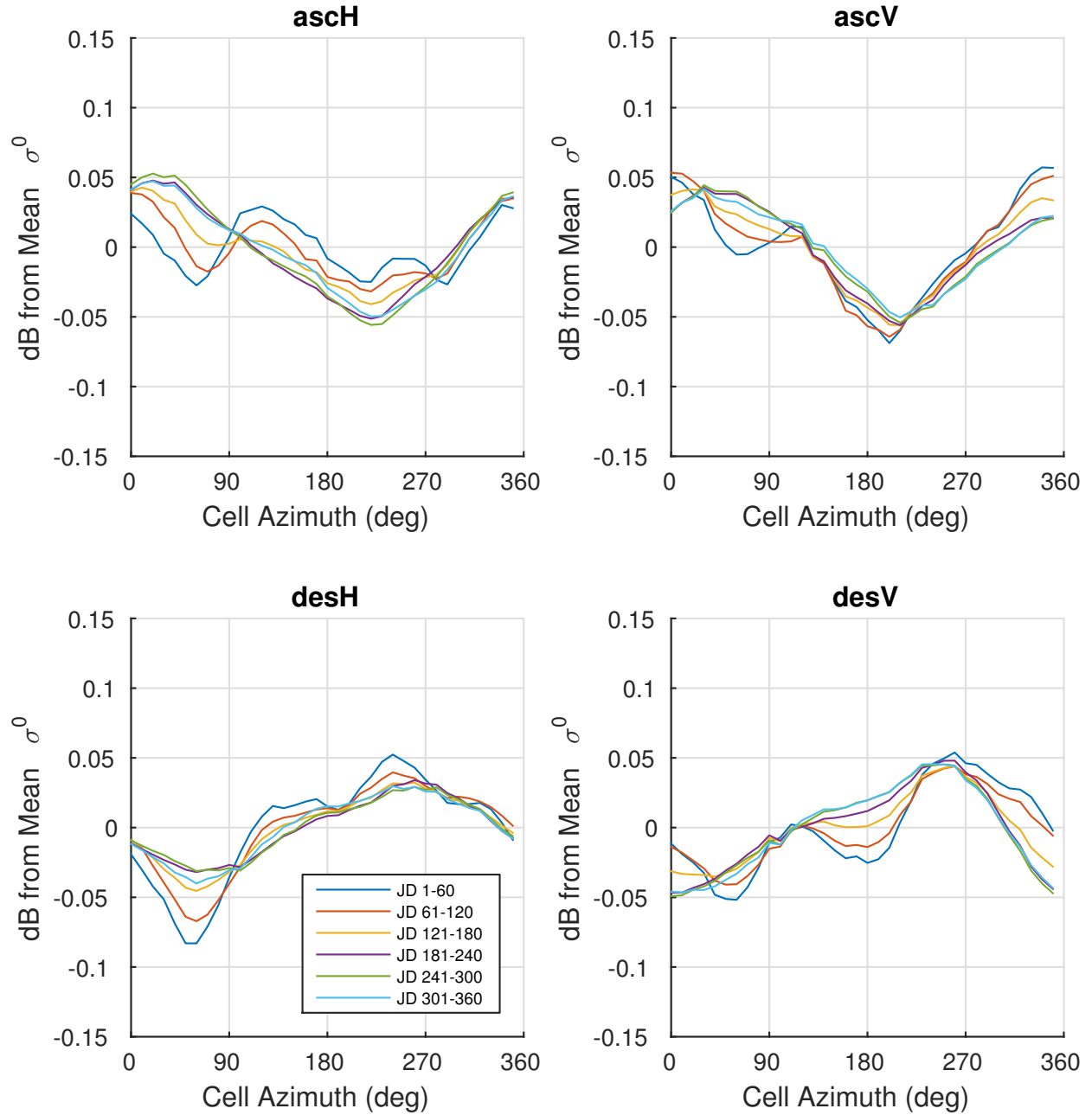
Figure 4.7: Azimuth σ^0 response of the Amazon rainforest. Separate lines shown for different times of the year. Azimuth angle is measured clockwise from north.
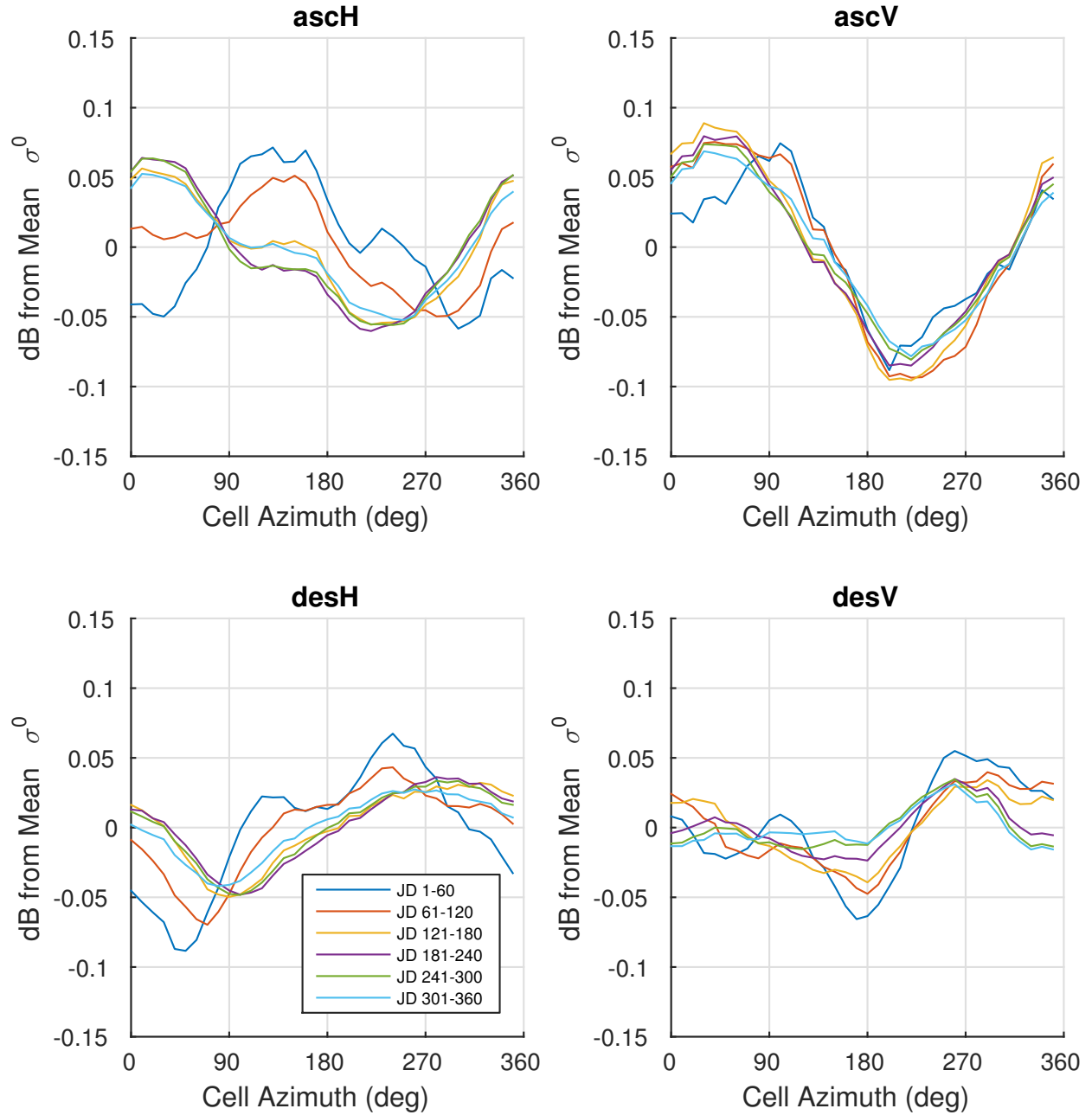
Figure 4.8: Azimuth σ^0 response of the Congo rainforest. Separate lines shown for different times of the year. Azimuth angle is measured clockwise from north.

where σ^0_{ave} is the σ^0_{true} term from Equation 4.1 averaged in azimuth. Note the inclusion of η, which is a term representing the azimuth dependency in the target and the azimuth biases in the target. When averaged over a set of data uniformly distributed in azimuth the term is zero mean by definition of σ^0_{ave}.

4.3   Incidence Dependence

The backscatter response over the rainforest targets is dependent on the incidence angle. The incidence angle for the purposes of this thesis is defined as the angle between the look vector and the vector normal to the surface of the earth. Three of the datasets measure σ^0 at multiple incidence angles, NSCAT, QuikSCAT PWM, and RapidScat. The QuikSCAT wind mission measured σ^0 at a constant incidence angle. These datasets are used to estimate the incidence angle dependence and whether that dependence changes with time.

NSCAT as a fan-beam scatterometer measures σ^0 over a wide range of incidence angles with every pulse. A scatter plot of σ^0 and incidence angle for NSCAT is shown in Figure 4.9. It can be seen that the response of σ^0 to incidence is generally non-linear but can be approximated as linear in dB over the region of interest for RapidScat calibration.

The NSCAT dataset is used to explore the possibility that incidence dependence may change over time. This is the only dataset available that is suited for estimating incidence dependence evolution with season. The local time of RapidScat data is constantly changing which can obscure any seasonal dependence and QuikSCAT PWM data only has a fixed incidence angle for any given season. Results for estimating incidence dependence for fifty day non-overlapping windows are shown in Figures 4.10 and 4.11. The estimates are almost all in the same range of -0.1 to -0.16 dB per degree. Within that range there is considerable variation between the estimates from different beams. It cannot be conclusively stated what the relation between season and incidence dependence is.

Without an adequate seasonal variation estimate a single average incidence dependence is sought for the entire mission. The first strategy is to take the data for each beam and fit a single least squares line to it, then average the slopes of those lines. Another strategy is to calculate a best-fit line for each pulse then average each of those estimates. This has the advantage of having a lot of estimates, all at the same time and adjacent locations. On
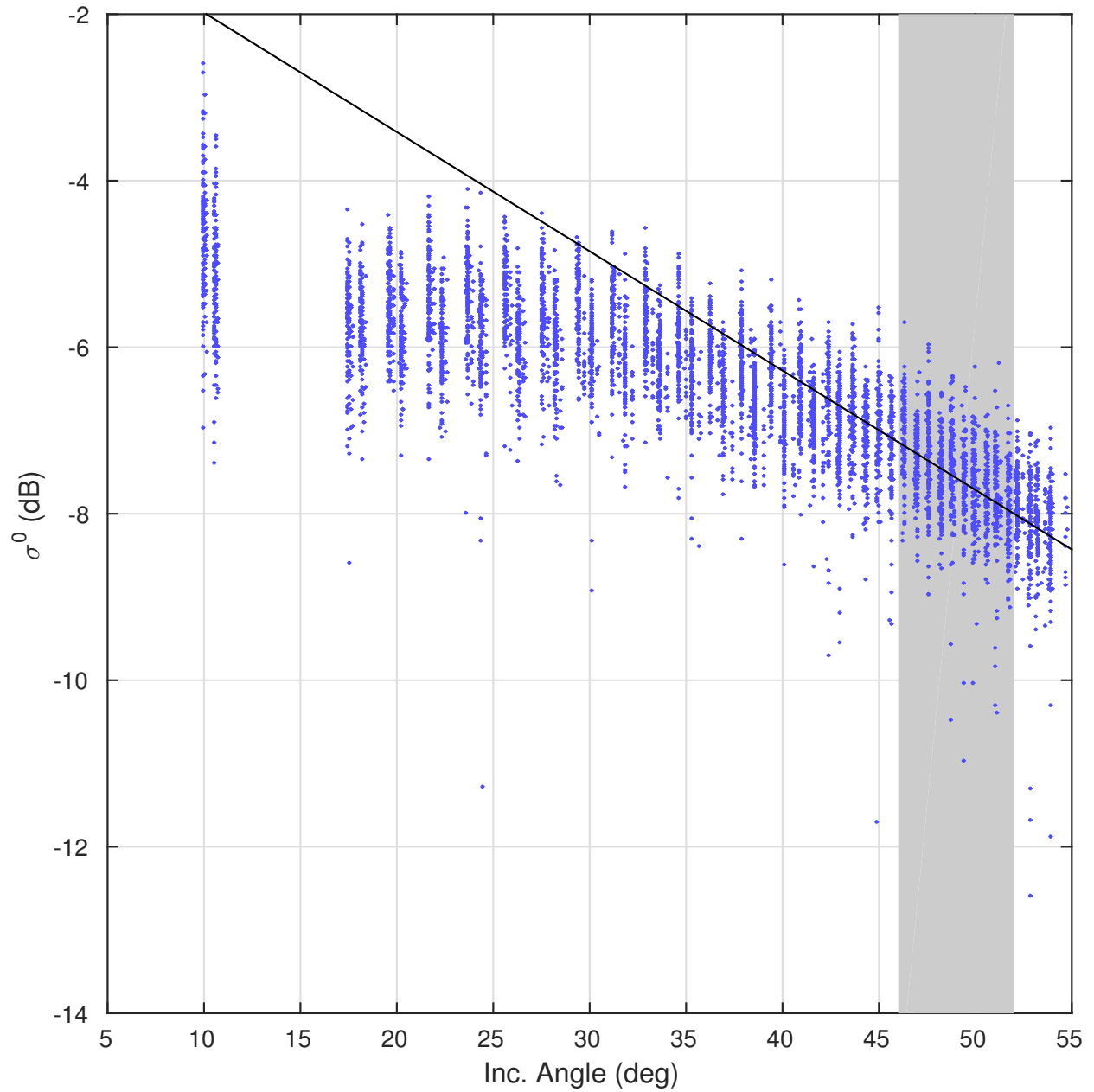
Figure 4.9: Scatter plot of incidence angle versus σ^0 measured over the NSCAT mission life. Amazon mask. H-pol. Ascending passes only. Shaded area indicates incidence angles of interest for RapidScat calibration (H-pol). Linear least squared error line for shaded area is also shown.
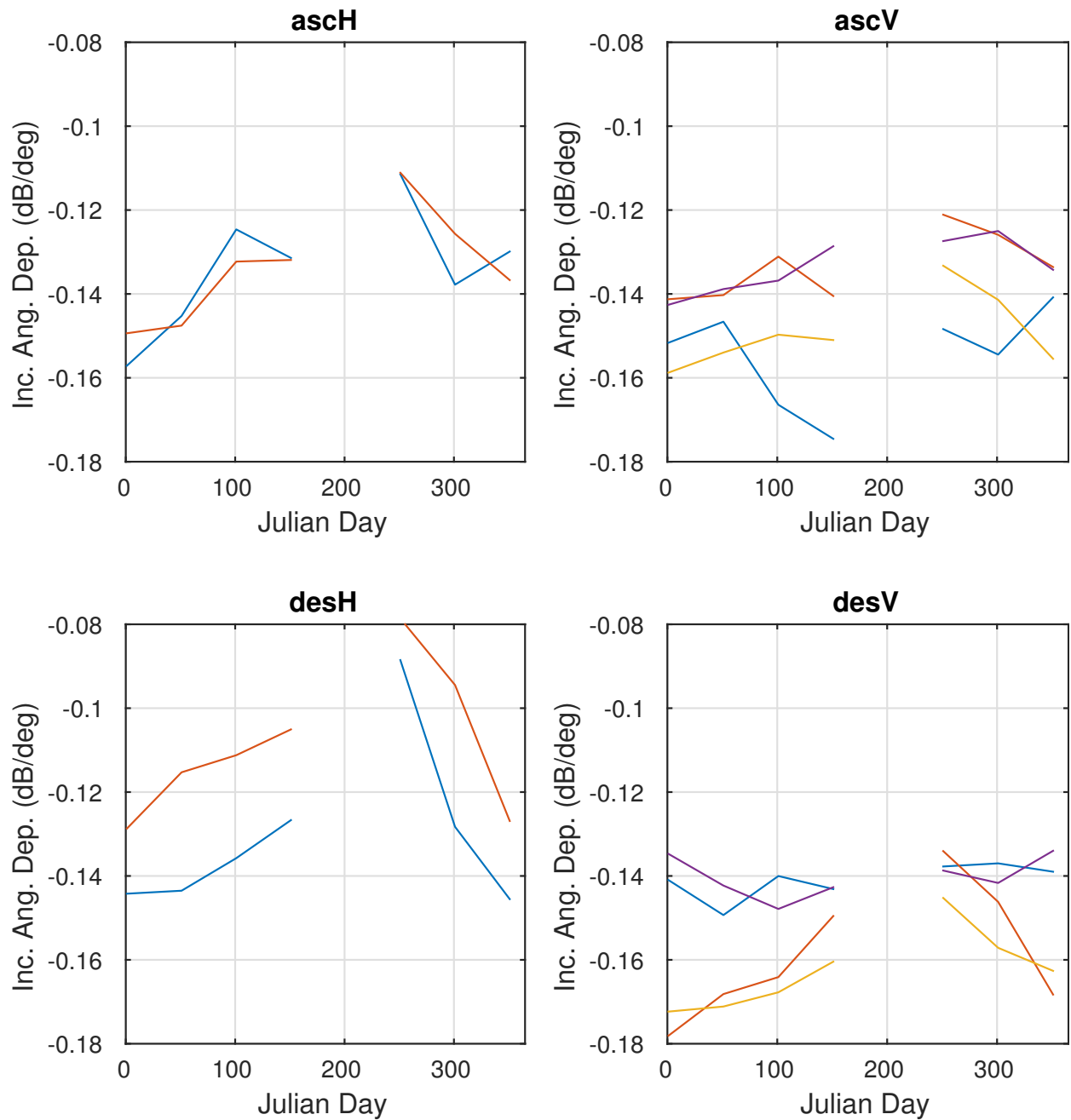
Figure 4.10: Amazon incidence angle dependence for 50 day blocks of the NSCAT dataset calculated by taking the slope of a single least-squares fit line to the data. Data used for dependence estimation is limited to a 6° range around the nominal RapidScat incidence angle for each polarization. A separate line is shown for the estimate from each beam. NSCAT has two H-pol beams and 6 V-pol beams. Estimates are only shown if at least 1000 points are present for the least-squares fit.
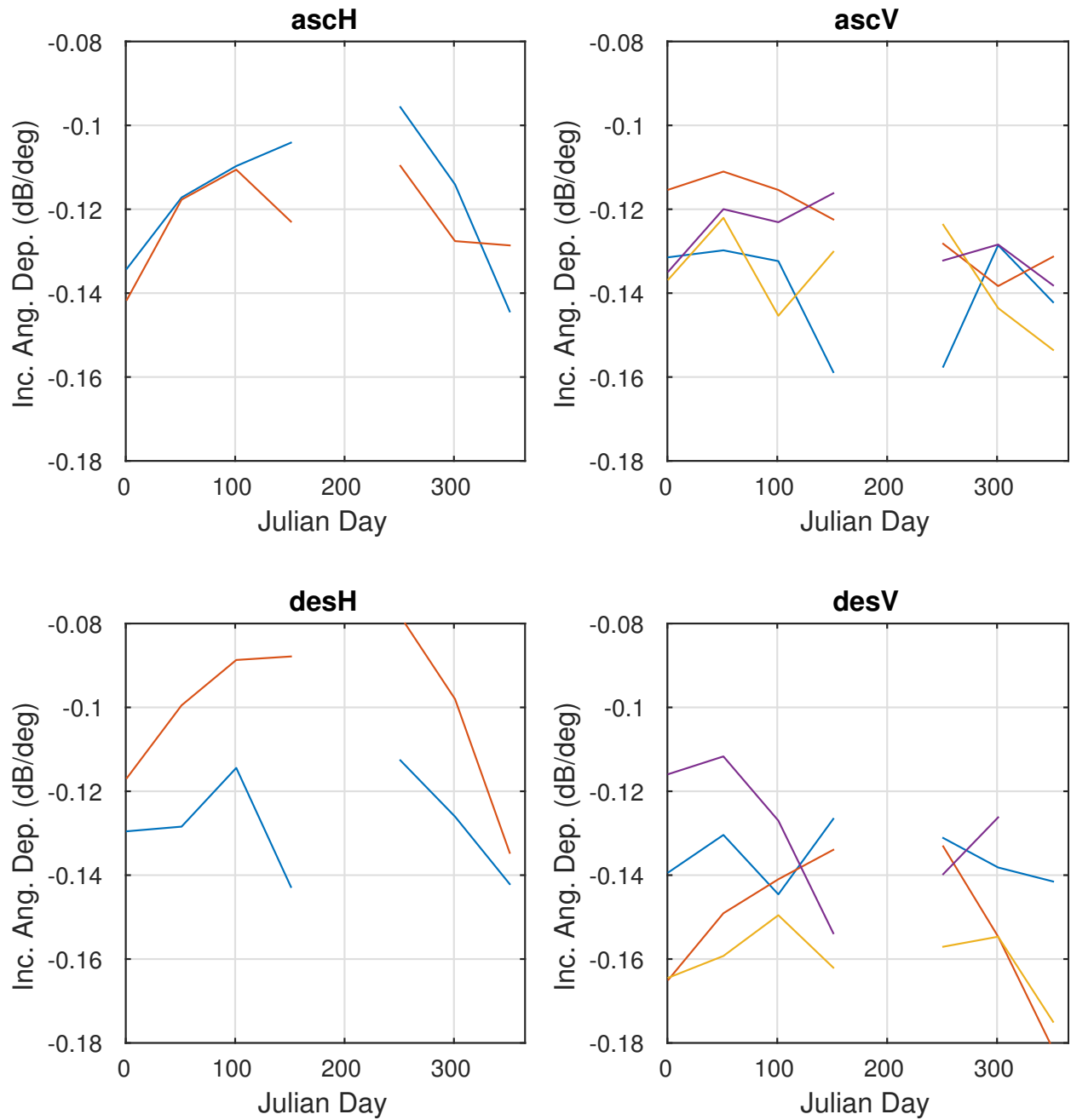
Figure 4.11: Congo incidence angle dependence for 50 day blocks of the NSCAT dataset calculated by taking the slope of a single least-squares fit line to the data. Data used for dependence estimation is limited to a 6° range around the nominal RapidScat incidence angle for each polarization. A separate line is shown for the estimate from each beam. Estimates are only shown if at least 1000 points are present for the least-squares fit.

the other hand, noisy measurements can cause extremely large swings in the the estimate of the slope. Both methods are tried and give very similar results as shown in Table 4.1.

QuikSCAT PWM data can also be used to estimate incidence angle dependence. The QuikSCAT PWM data measures σ^0 at distinct incidence and azimuth angles for months at a time. Even small biases due to azimuth or time of year can greatly impact the accuracy of the incidence angle estimate. For example, one set of incidence angles is measured at $220°$ cell azimuth (ascending) and another at $40°$ cell azimuth (ascending). From Figures 4.7 and 4.8 it can be seen that there is an azimuth bias between those two values of around 0.1 dB. If left uncorrected, this could result in a bias in the incidence angle estimate of 0.05 dB. To mitigate this, corrective factors for azimuth and seasonal biases (see Section 4.4) are applied before estimating incidence angle dependence. The estimates for incidence angle dependence are included in Table 4.1.

RapidScat data is also used for measuring incidence dependence. As with NSCAT two methods are used to estimate incidence angle dependence. In the first, data is binned by local time, then the linear regression is performed on all data within that bin. In the second method, an estimate of the incidence dependence is calculated for each revolution. These estimates are averaged for each local time using the product of the number of points and the range of incidence covered as a weighting factor. This method is found to produce slightly more consistent estimates of incidence dependence and so are shown in Figures 4.12 and 4.13. The average incidence dependence averaged across all local times are included in Table 4.1.

There are a number of things to note in Figures 4.12 and 4.13. First is that the RapidScat estimate of incidence dependence is relatively flat. There is some variation, but considering the standard error bars on the estimates, the variation may be primarily noise. Another thing to note is that generally the estimates from NSCAT data correspond reasonably well with RapidScat. The QuikSCAT PWM data is less consistent. This could be due to the lack of samples in each estimate, inaccuracies in the correction factors applied, and also year to year variation in the target. NSCAT incidence dependence estimates are consistently lower than the RapidScat estimates. This could also be due to instrument specific biases in the retrieval process for either sensor, so it cannot be conclusively stated that one is
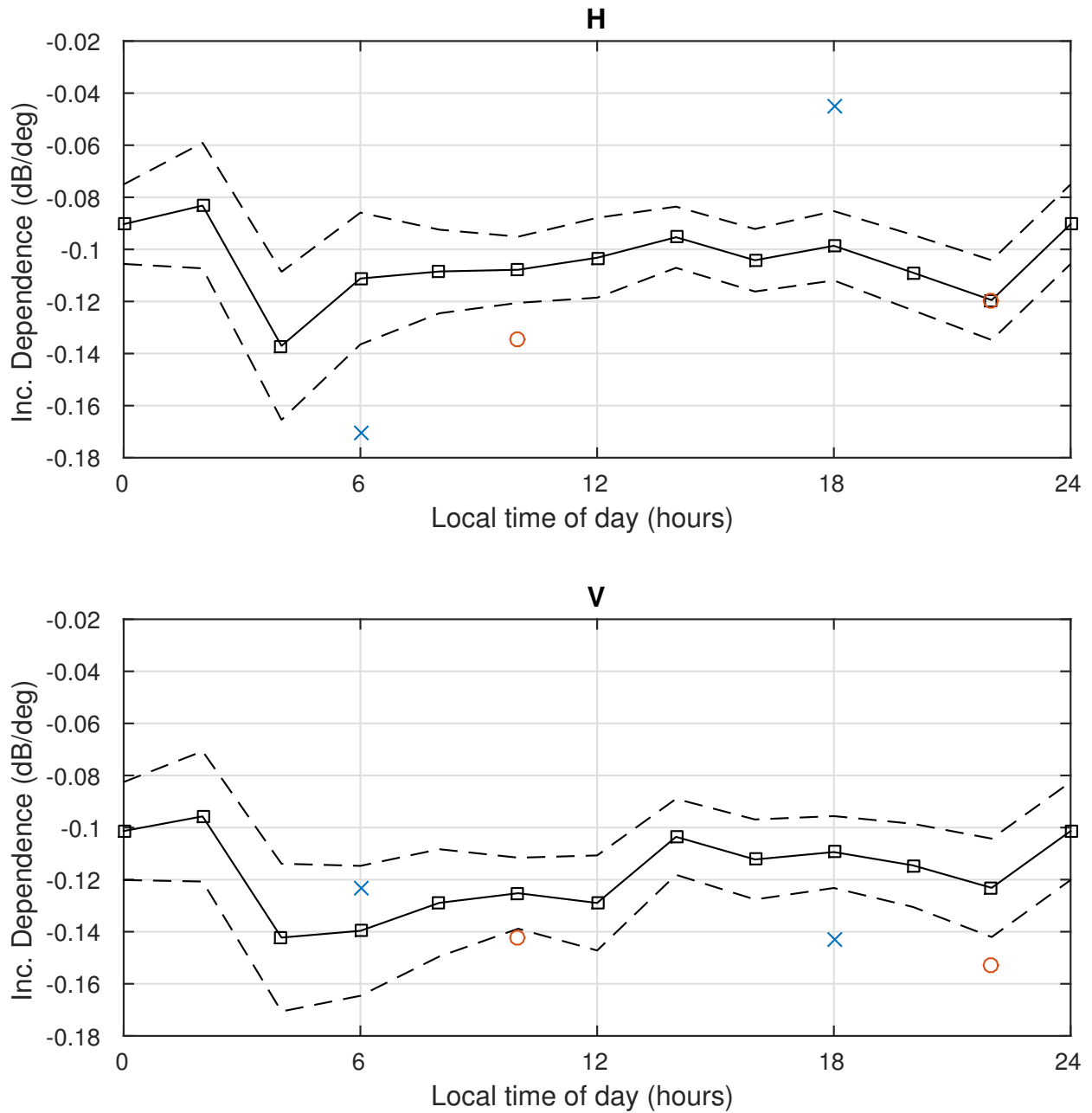
Figure 4.12: Incidence angle dependence as a function of local time of day over the Amazon. Solid line with □ indicates RapidScat estimate of incidence dependence. Dotted lines indicate the weighted standard error of the estimate. QuikSCAT PWM estimates (×) and NSCAT estimates (○) are also shown.
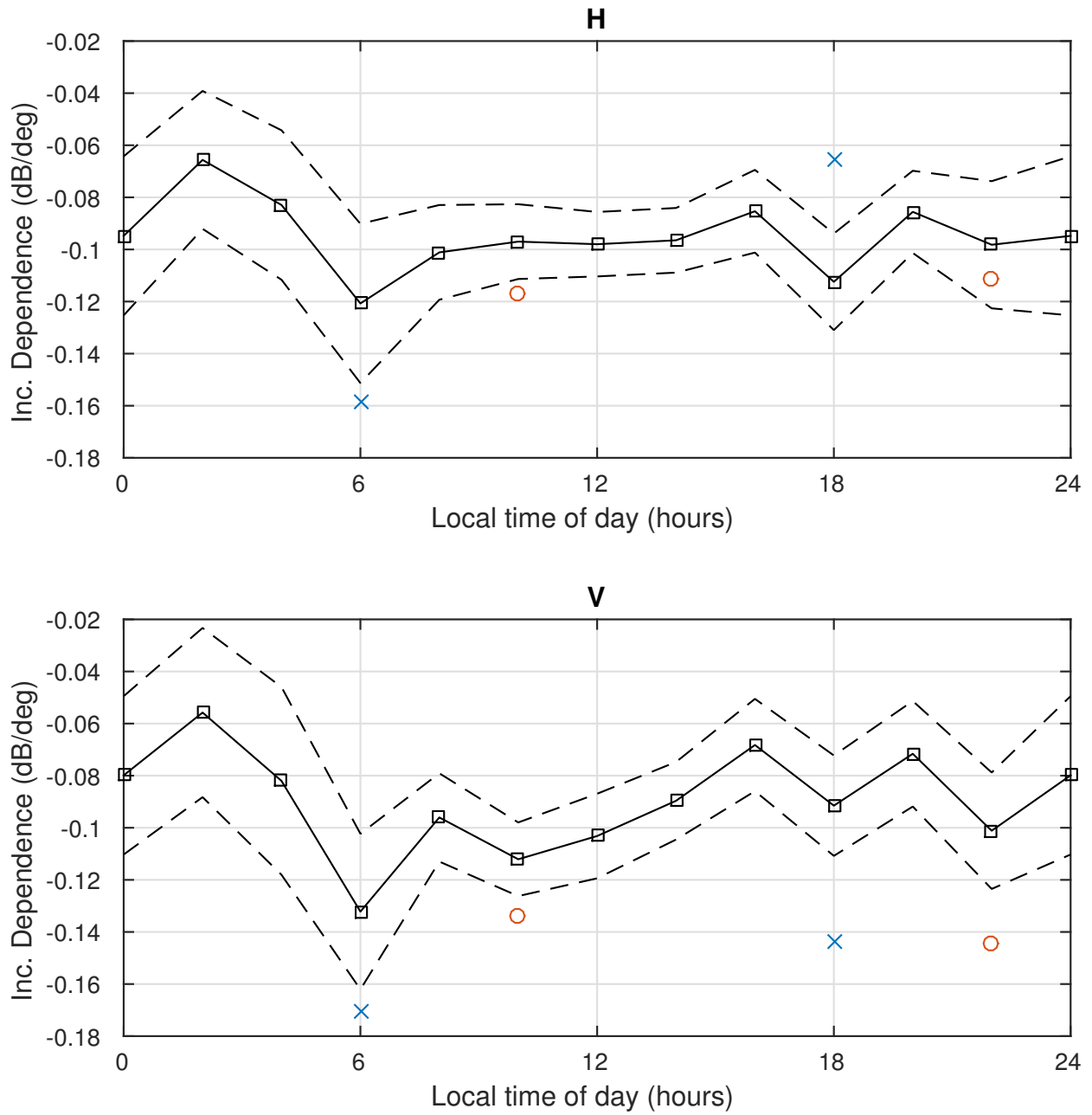
Figure 4.13: Incidence angle dependence as a function of local time of day over the Congo. The solid line with □ indicates RapidScat estimate of incidence dependence. Dotted lines indicate the weighted standard error of the estimate. QuikSCAT PWM estimates (×) and NSCAT estimates (○) are also shown.

correct or incorrect. As a result, an average of the NSCAT incidence dependence estimates are used to normalize NSCAT incidence and RapidScat incidence dependence estimates are used for RapidScat data. The QuikSCAT PWM estimates vary too greatly to be used.

Accuracy of the incidence correction is important. The average difference between RapidScat incidence angle and the QuikSCAT nominal incidence angle is about 1.1° for H-pol and 2.5° for V-pol. Meanwhile estimates for the incidence angle dependence vary by as much as 0.04 dB/degree. If the incidence dependence estimate were used to compare RapidScat and QuikSCAT a 0.04 dB/degree difference translates into a mean σ^0 difference of 0.04 dB for H-pol and 0.1 dB for V-pol. This is considerable and should be considered when applying incidence corrections in order to compare sensors with different mean incidence angles.

We again update the observation model. The incidence dependence is approximated as linear in dB. From Figures 4.10, 4.11, 4.12, and 4.13, it is decided that any variations in incidence dependence with time are not large enough to reliably measure with any of the datasets currently available. With these considerations we separate the incidence dependence from that the σ^0_{avg} and instrument bias terms from Equation 4.1 to give,

$$\sigma^0_{\text{meas}} = \sigma^0_{\text{nom}}(t) + m(b) \times (\theta - \theta_{\text{nom}}) + B(b,t) + n + \eta, \tag{4.3}$$

where m is the linear (dB/deg) incidence dependence for the polarization and instrument, θ is still the incidence angle of the measurement and θ_{nom} is the nominal incidence angle. The term σ^0_{nom} now indicates the σ^0_{avg} from Equation 4.1 at the nominal incidence angle. The η term now includes imperfections in the incidence dependence estimate. There are different incidence dependence estimates for each beam due to the incorporation of the incidence component of the bias term. The incidence dependence estimates are shown below for NSCAT, QuikSCAT PWM, and RapidScat.

4.4 Time Dependence

The σ^0 response of the rainforests change with time. There are natural cycles both seasonal and diurnal that affect the scattering properties of the target. These can be estimated using QuikSCAT and RapidScat, respectively. There are other variations in the target

Table 4.1: Incidence angle dependence as measured by different sensors. The methods column indicates at which level linear regression was performed.

Sensor	Method	Mask	AscH	DesH	AscV	DesV
NSCAT	Beams	Ama	-0.1354	-0.1205	-0.1427	-0.1516
		Con	-0.1196	-0.1121	-0.1308	-0.1434
	Pulses	Ama	-0.1336	-0.1191	-0.1415	-0.1543
		Con	-0.1146	-0.1110	-0.1368	-0.1449
QSCAT PWM	All	Ama	-0.1702	-0.0453	-0.1231	-0.1427
		Con	-0.1582	-0.0655	-0.1705	-0.1440
RapidScat	Revs	Ama	-0.1060		-0.1190	
		Con	-0.1013		-0.0946	
	Local Times	Ama	-0.0971		-0.1243	
		Con	-0.1227		-0.1376	

response due to daily weather and other phenomena. These cannot easily be corrected for and so are considered noise terms to be averaged out. There is also long term drift from year to year in both the target and the instrument. It is difficult to distinguish drift in the target and drift in the instrument without measurements from multiple instruments overlapping for years. Regardless of the source, drift should be taken into consideration when comparing samples taken years apart. QuikSCAT over its 10 year mission life had yearly averages that vary by as much as 0.1 dB.

QuikSCAT can be used to estimate average seasonal variations over its mission life. To estimate the seasonal variation the data is divided into ten-day bins. For each year of data, the yearly average is subtracted to give the deviation from the yearly average. These deviations are then averaged across the ten years of QuikSCAT's mission. The results are shown in Figures 4.14 and 4.15. It is noted that seasonal variations differ between the descending and ascending passes. This suggests that seasonal and diurnal variations are linked, since descending and ascending passes are measured at different local times.

Diurnal variation is measured using RapidScat. RapidScat observes the calibration target at a particular local time of day every month if ascending and descending passes are used, so for a given local time the average σ^0 is effectively sampled every month. Averaging these monthly samples gives the graphs seen in Figures 4.16 and 4.17. There is a clear peak in average σ^0 near sunrise in both the Amazon and the Congo. This can be attributed to
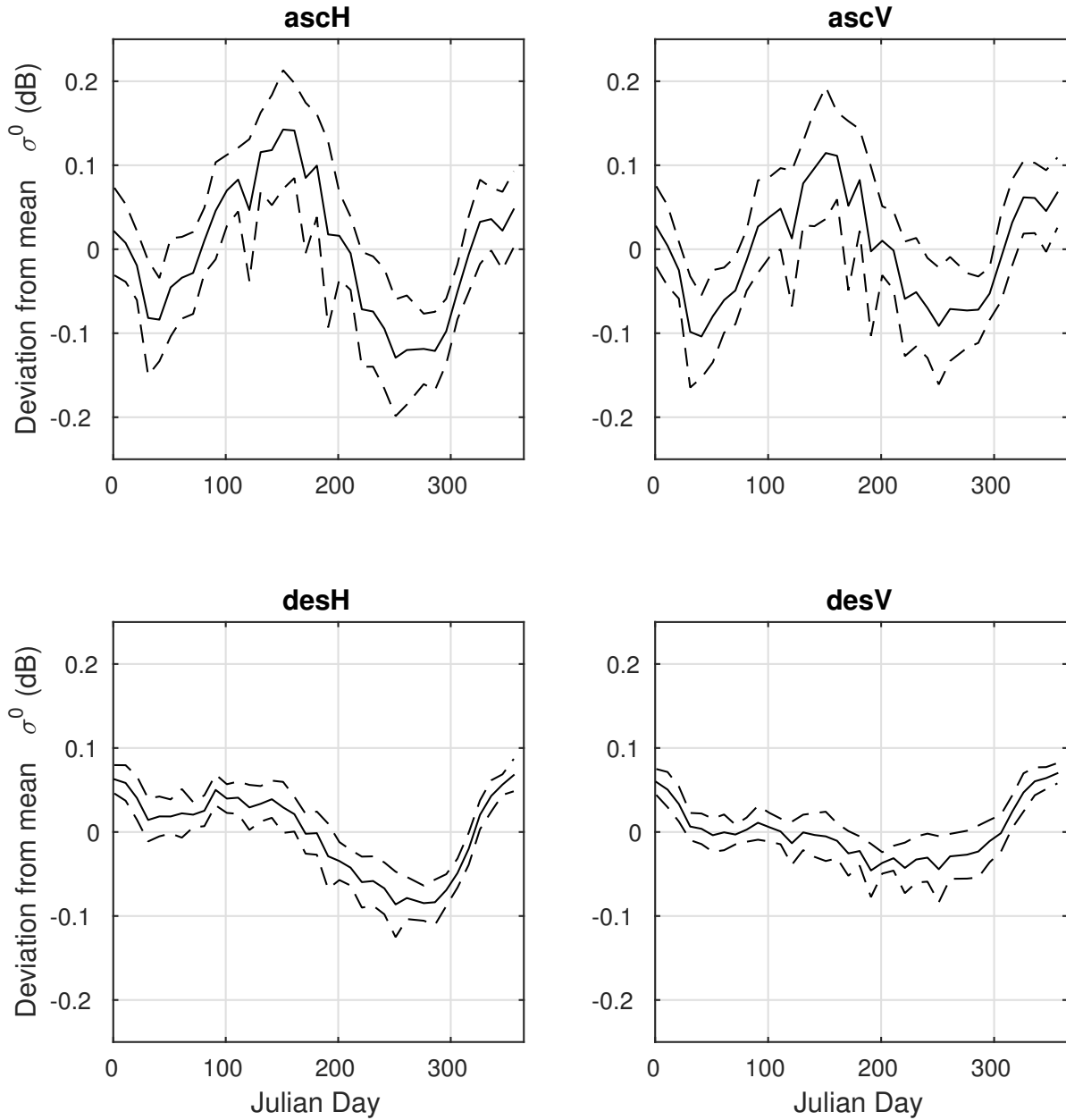
Figure 4.14: Mean deviation from the yearly average for ten day bins for the Amazon. The standard deviation of the yearly averages is indicated with dotted lines.
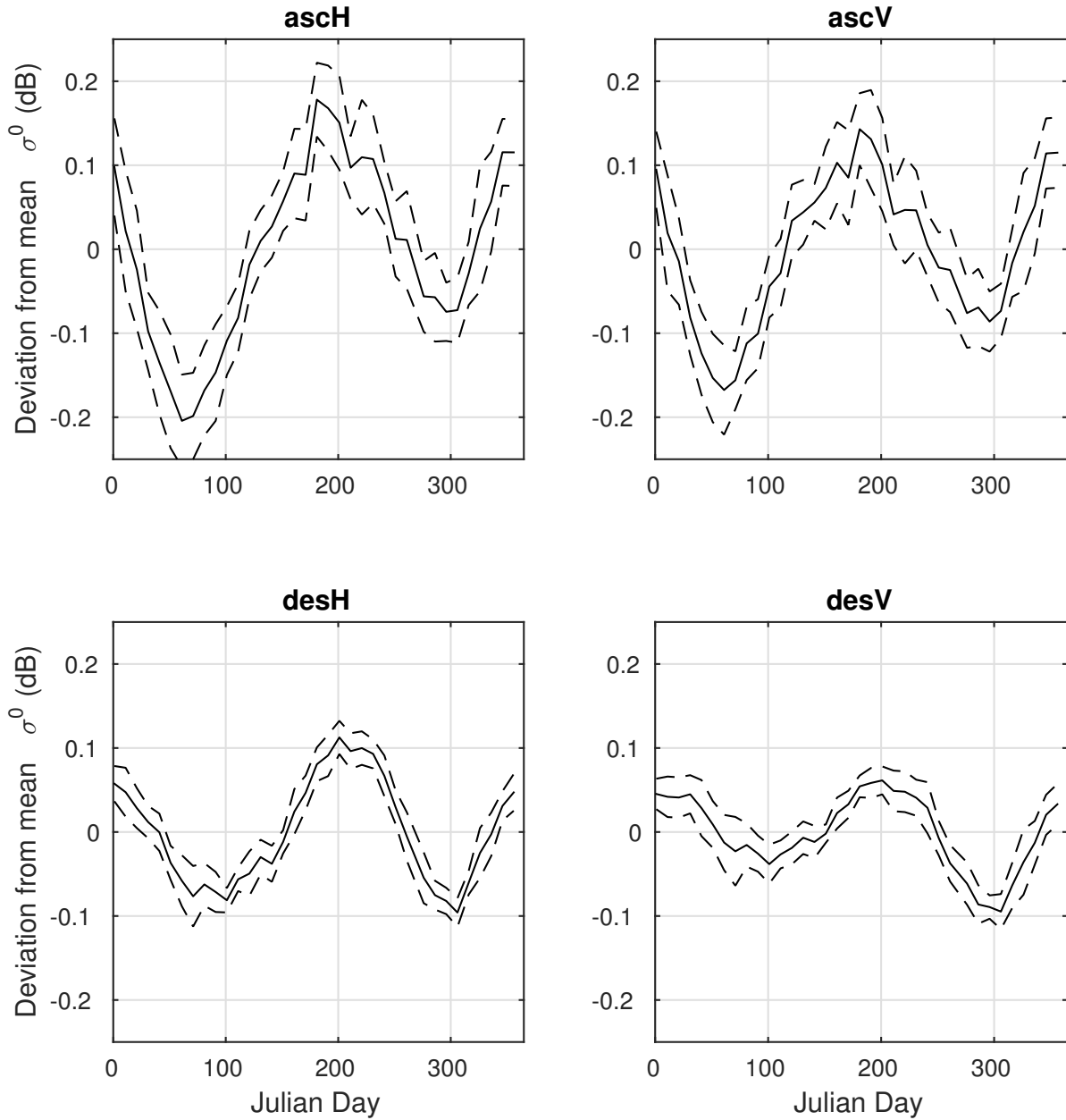
Figure 4.15: Mean deviation from the yearly average for ten day bins for the Congo. The standard deviation of the yearly averages is indicated with dotted lines.

dew accumulation on the leaves of the canopy [39]. Taking the standard deviation of the monthly samples gives a rough estimate for the magnitude of the seasonal variation at that local time of day. This standard deviation is shown with the dotted lines in Figures 4.16 and 4.17. It can be seen that at least for the Amazon the deviation is greater around 6 a.m. where the seasonal variation measured by QuikSCAT is greater.

This is the first time the full diurnal σ^0 cycle of the Amazon or the Congo has been measured with a single sensor. Figures 4.16 and 4.17 also show the averages for QuikSCAT ascending and descending passes. The difference between the averages is well predicted by the diurnal signal measured by RapidScat.

Temporal dependencies are complex and interconnected. It is seen that there are general seasonal cycles and diurnal cycles and that the two are connected. The inter-dependencies between seasonal and diurnal variations can cause considerable biases during comparison. To mitigate this, comparisons are limited to narrow ranges of local time of day. We update our observation model to:

$$\sigma^0_{\text{meas}} = \sigma^0_{\text{ave}} + m(b) \times (\theta - \theta_{\text{nom}}) + T(t_{\text{seas}}, t_{\text{diurn}}) + B(b, t) + n + \eta, \qquad (4.4)$$

where σ^0_{ave} is the true σ^0 averages across all times of year and local times at the nominal incidence angle. T is the combined seasonal and temporal variation, leaving other temporal variations as part of the η term.

The observation model in Equation 4.4 can be used "normalize" σ^0 measurements from different sensors at different times. By taking σ^0_{meas} and subtracting out the incidence dependence we can get the corresponding σ^0_{meas} at the nominal incidence:

$$\sigma^0_{\text{nom}} = \sigma^0_{\text{meas}} - m(b) \times (\theta - \theta_{\text{nom}}). \qquad (4.5)$$

Further, subtracting out the time dependence leaves the true σ^0 with the noise and bias terms. Comparing these "normalized" σ^0 from different sensors gives estimates for the sensor-dependent biases. Comparing the "normalized" σ^0 for the same sensor from different times gives an estimate of time-dependent biases such as instrument drift.
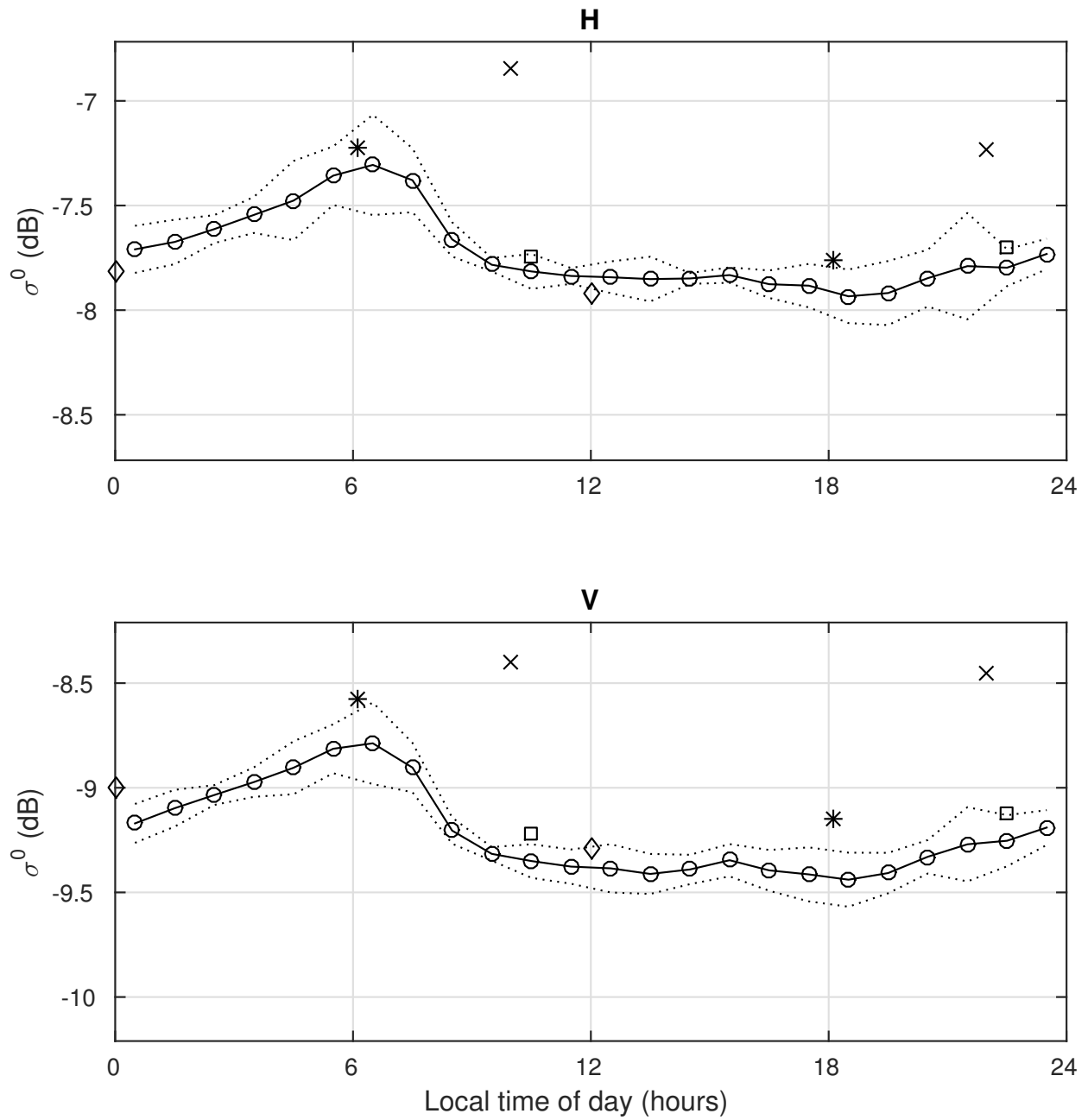
Figure 4.16: Diurnal σ^0 response of the Amazon. Dotted lines indicate standard deviation of the averages of each monthly sample of the diurnal signal. Asterisks indicate QuikSCAT mission average σ^0 for the region and the times of year covered by RapidScat. Diamonds and X's indicate OSCAT and NSCAT averages respectively. Both have been normalized to QuikSCAT incidence angles.

43
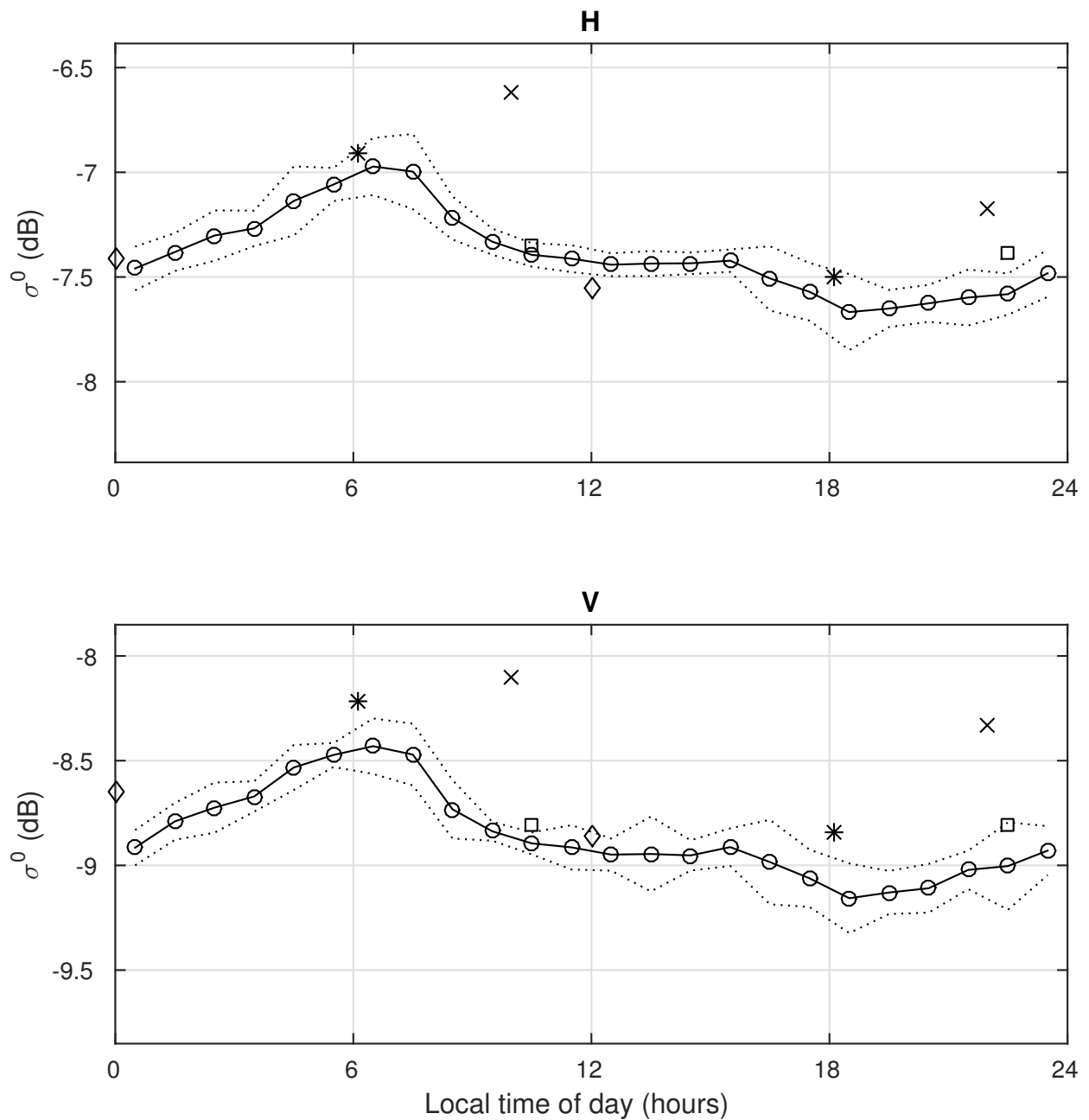
Figure 4.17: Diurnal σ^0 response of the Congo. Dotted lines indicate standard deviation of the averages of each monthly sample of the diurnal signal. Asterisks indicate QuikSCAT mission average σ^0 for the region and the times of year covered by RapidScat. Diamonds and X's indicate OSCAT and NSCAT averages respectively. Both have been normalized to QuikSCAT incidence angles.
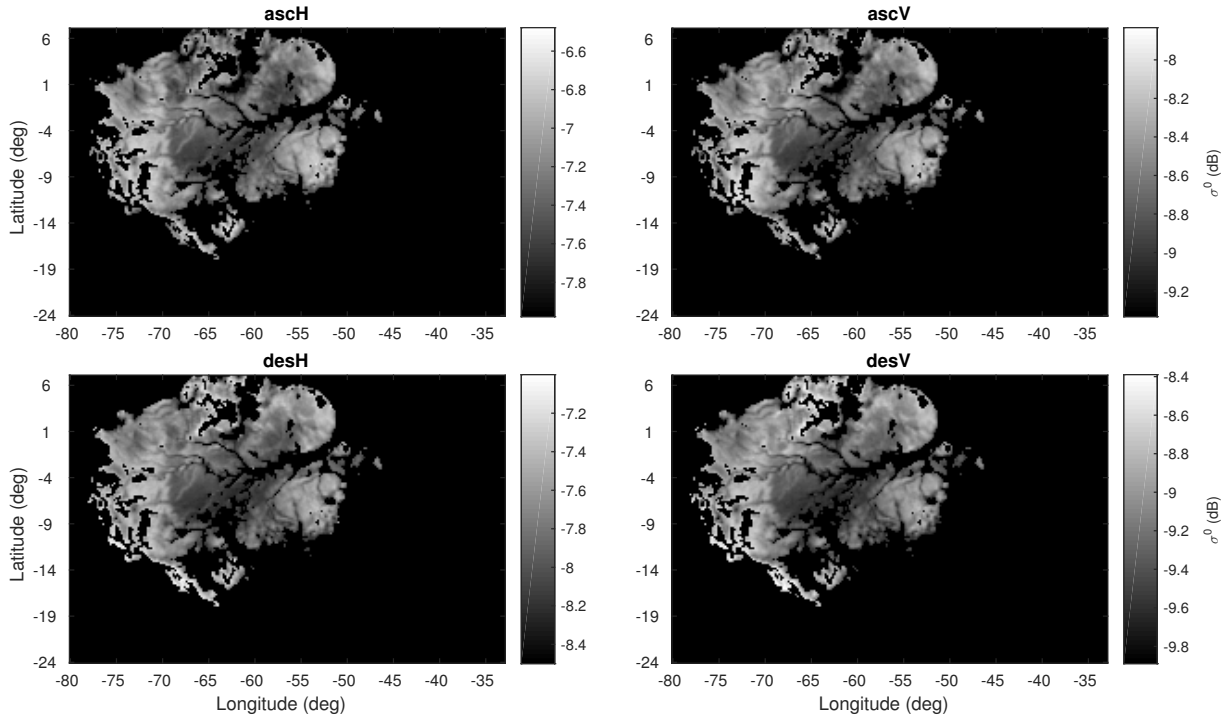
Figure 4.18: Plot of QuikSCAT average σ^0 values for $0.2°\times0.2°$ latitude-longitude spatial bins over the Amazon for each "flavor."

4.5   Spatial Variation

Up until this point, the entire region covered by the mask has been treated as a uniform target. This is is in part because, like an azimuth dependency, the different regions are sampled often. As a result even for relatively small sets of data the spatial distribution is the same as for larger sets. An exception is the QuikSCAT PWM data, where the swath is so narrow that weeks of data must be combined to cover the entire mask. Spatial variations in vegetation and climate can cause mean differences between different areas, and also cause them to vary differently with season, time of day, azimuth, and incidence.

First we examine spatial variations in mean σ^0 within the mask. The mask was selected to minimize the variation to 1 dB. We examine this variation by binning the data within the mask by latitude and longitude into $0.2°\times0.2°$ bins, then taking the averages. The spatial averages can be seen in Figures 4.18 and 4.19. These figures show structure in the mean σ^0, a result of variations in terrain, vegetation, and climate within the mask.
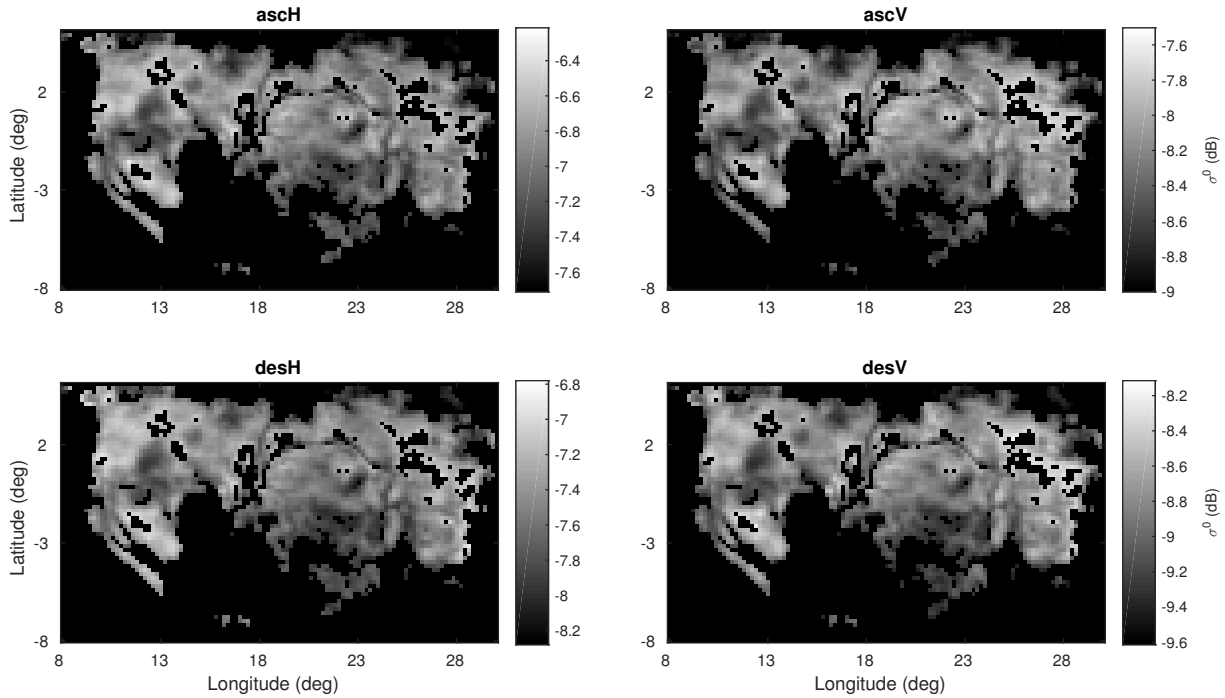
Figure 4.19: Plot of QuikSCAT average σ^0 values for $0.2° \times 0.2°$ latitude-longitude spatial bins over the Congo for each "flavor."

In addition to variations in mean σ^0, different areas within the mask may each have a distinct seasonal, diurnal, azimuthal, or incidence responses. These potentially different responses are explored by breaking the mask into sub-masks and examining the response of each sub-mask with respect to these variables. Though not used in calibration, these responses are shown in Appendix B.

Chapter 5

Results

In this chapter, we use the observation model developed in Chapter 4 to validate RapidScat σ^0 and to estimate biases relative to other sensors. In Section 5.1, we discuss the discovery of imperfections in one of the data quality flags. In Section 5.2, instrument stability over the RapidScat mission is evaluated. Calibration for "slice" measurements is considered in Section 5.3. In Section 5.4, RapidScat σ^0 measurements are compared with measurements from other instruments with an emphasis on the relative bias between RapidScat and QuikSCAT.

5.1 Solar Panel Flag

The Amazon rainforest has much less variance in its response than most areas of the earth making it a good region to notice invalid σ^0 readings. Some, abnormally low σ^0 values were found in RapidScat measurements over the Amazon during the calibration process. These abnormal measurements were found to be limited to a range of antenna azimuth angles as shown in Figure 5.1. After consultation with JPL, it was determined that this was due to imperfections in the solar panel obstruction flag. Changes were made in the computation of the flag at JPL, and as a result, data processed after the fix will have these corrupted measurements flagged as unusable.

5.2 Instrument Stability

Instrument drift is the gradual change in σ^0 measurements due to attributes of the instrument as opposed to variations in the target itself. Sources of instrument drift can include hardware degradation, orbit changes, or attitude changes. The Amazon and Congo rainforests are relatively stable temporally and so can be used to estimate instrument drift.
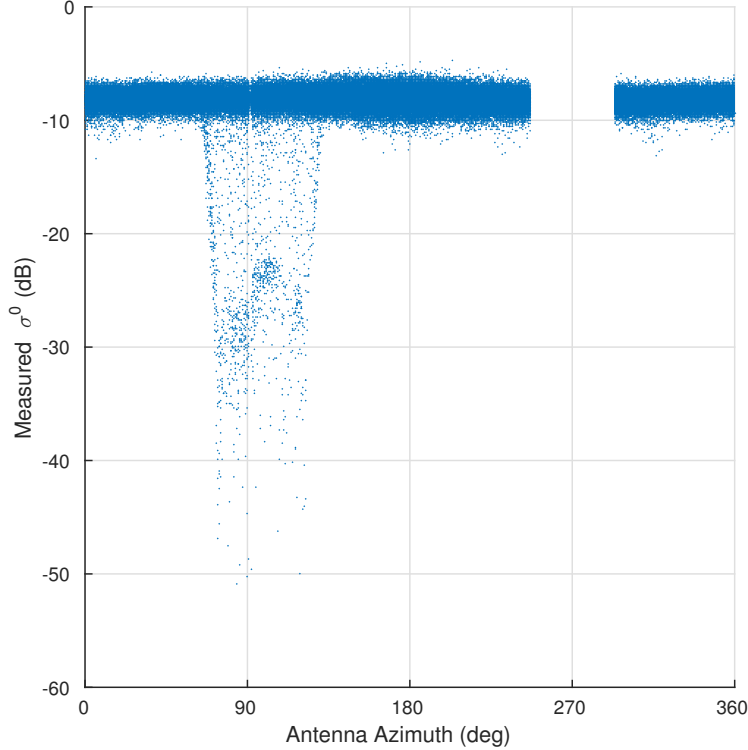
Figure 5.1: Scatter plot of antenna azimuth angle and σ^0 for RapidScat measurements within the Amazon mask for Julian days 330-340, 2014. Note the clearly abnormal σ^0 readings between 70 and 120 degrees antenna azimuth.

A major obstacle in the estimation of instrument drift for RapidScat is the changing local time of day of measurements as discussed in Chapter 3. This results in a ten-day average that peaks every month as shown in Figures 5.2 and 5.3. The peaks correspond with either ascending or descending passes having a local measurement time of 6 a.m. which is the maximum of the diurnal cycle.

The diurnal cycle can be removed by applying a local time of day correction based off the results in Section 4.4. Seasonal variation is corrected for using the seasonal variations measured by QuikSCAT also in Section 4.4. QuikSCAT is only able to measure seasonal variation at two local times of day, while the RapidScat measurements are taken at all local times. A rough correction for all local times is arrived at by averaging in dB the seasonal variations measured by QuikSCAT at 6 a.m. and 6 p.m. Applying the both the diurnal and seasonal correction gives the averages seen in Figures 5.4 and 5.5.

The remaining variations can be attributed to variations in the target not related to diurnal or seasonal cycles, imperfections in the corrections, and instrument drift. Variations from year to year for a given ten day period is generally much smaller than that seen in Figures 5.4 and 5.5 as (see Figures 4.14 and 4.15). The primary imperfections with the corrections lie in the inter-dependency between seasonal and diurnal variation. Since the diurnal variation is an average over the entire mission, it is possible that the diurnal signal is different during certain times of the year. It is also possible the seasonal correction is inaccurate when applied to measurements at all local times of day. These explanations are more likely than instrument drift, because instrument drift would be expected to affect the Amazon and the Congo average σ^0 is the same way.

In the end, the cause of the variability in Figures 5.4 and 5.5 is unknown, but the averages are quite stable with variation over the entire mission under 0.3 dB. This is in spite of considerable changes in the attitude and position of the platform.

5.3 Slice Balancing

All the work up until this point has focused on cell or "egg" measurements. Here we consider another type of measurement, termed "slice" measurements. The terms egg and slice refer to the shapes of the spatial response functions for the measurements as shown in Figures 5.6 and 5.7 respectively. The spatial response function shows how much of the response comes from any given point on the ground. The egg spatial response function is dominated by the antenna response giving an elliptical shape. The slice measurement has range-Doppler processing applied to select a slice of the antenna response and so has a narrower spatial response function in one dimension.

We point out that the slice and egg σ^0 measurements should be the same after correcting for incidence. The process of calibrating the slice measurements so this is true is called slice balancing. RapidScat average σ^0 as a function of azimuth for each slice and the egg before slice balancing are shown in Figure 5.8. Results are similar for the Congo. It can be clearly be seen that the slice biases are a function of azimuth. The slices values vary widely for the aft looking azimuth angles, with the largest disparity of several dB between slices at
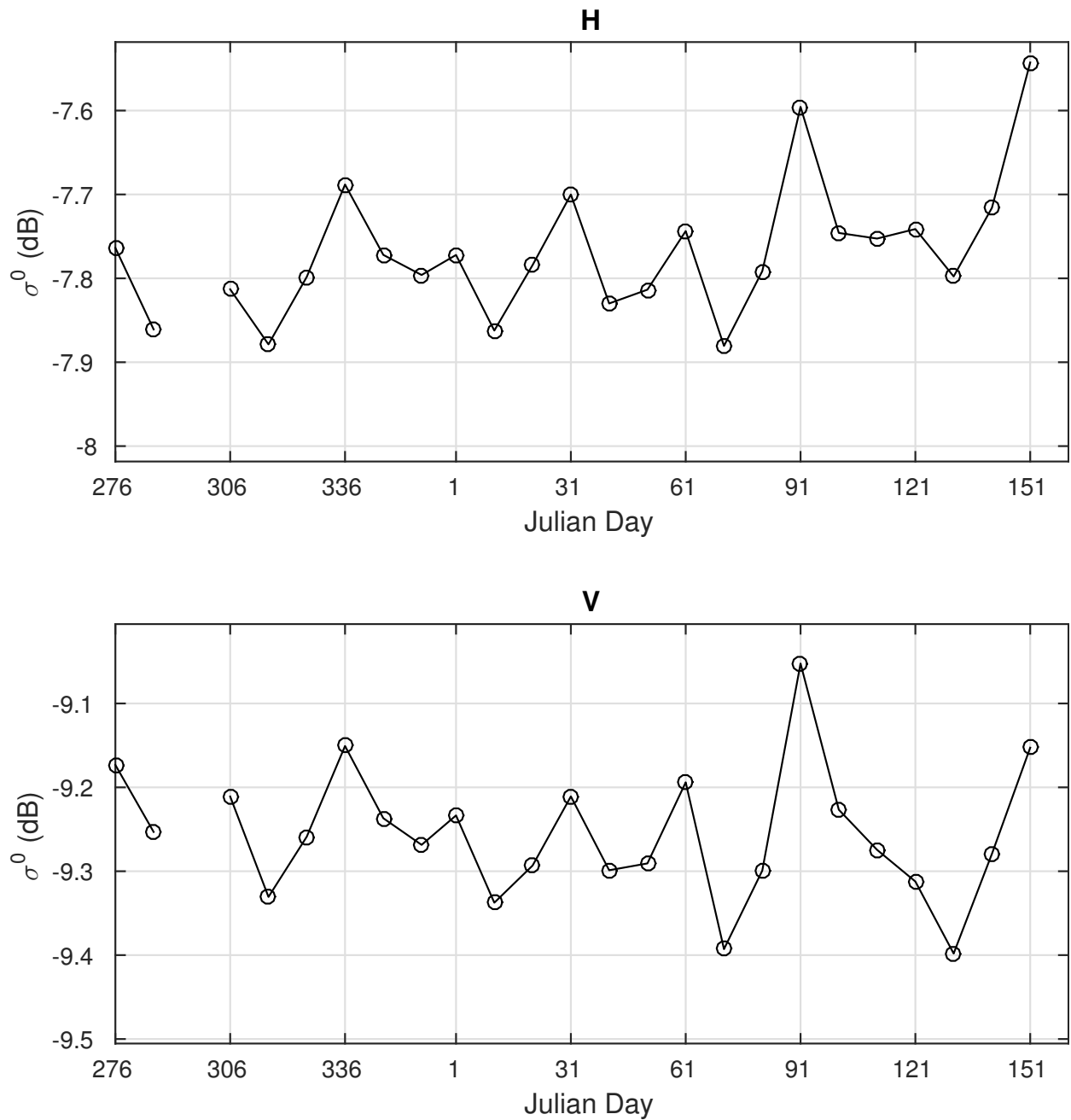
Figure 5.2: Ten day average σ^0 measured by RapidScat over the Amazon. The values have been corrected for incidence.
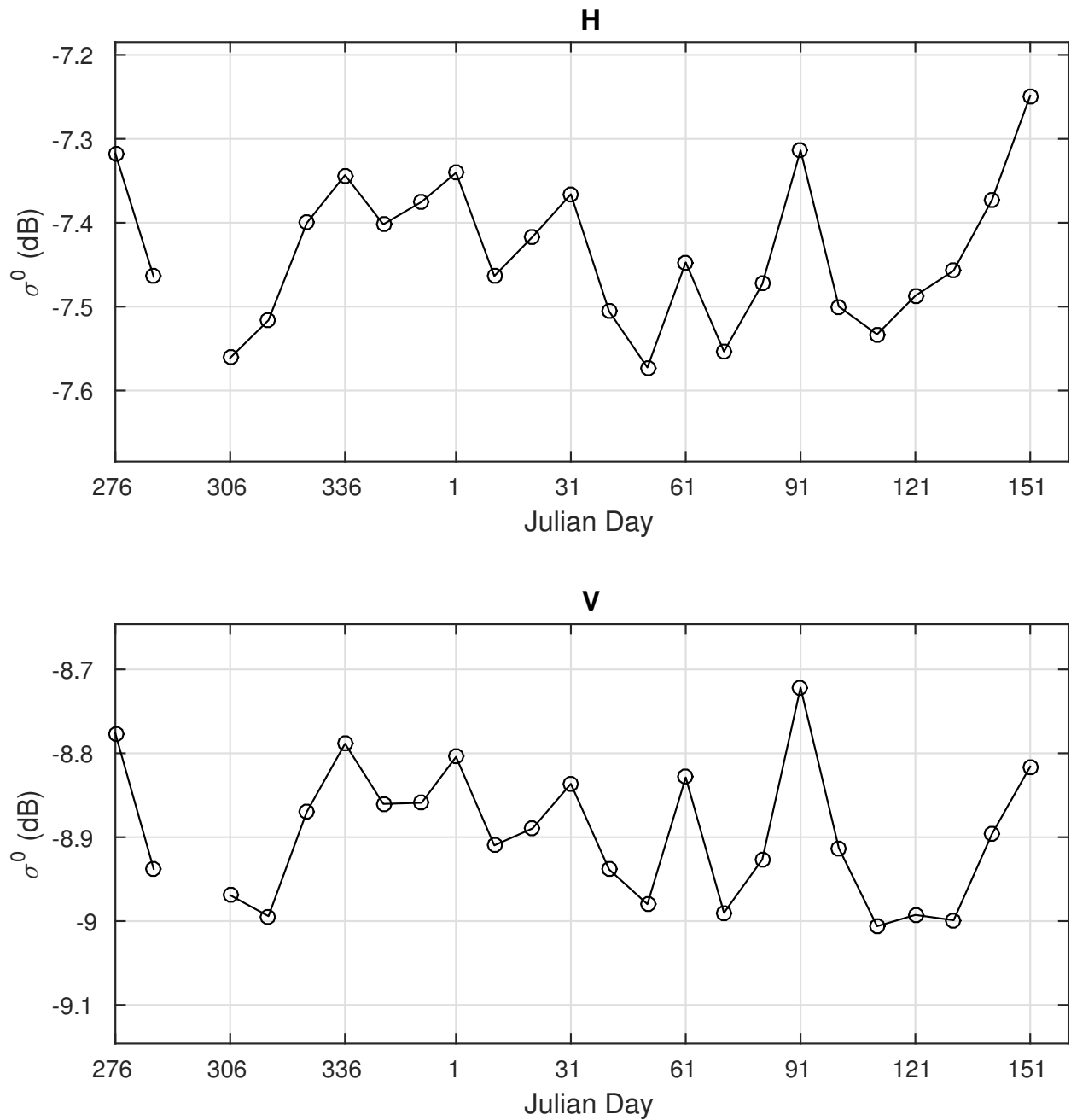
Figure 5.3: Ten day average σ^0 measured by RapidScat over the Congo. The values have been corrected for incidence.
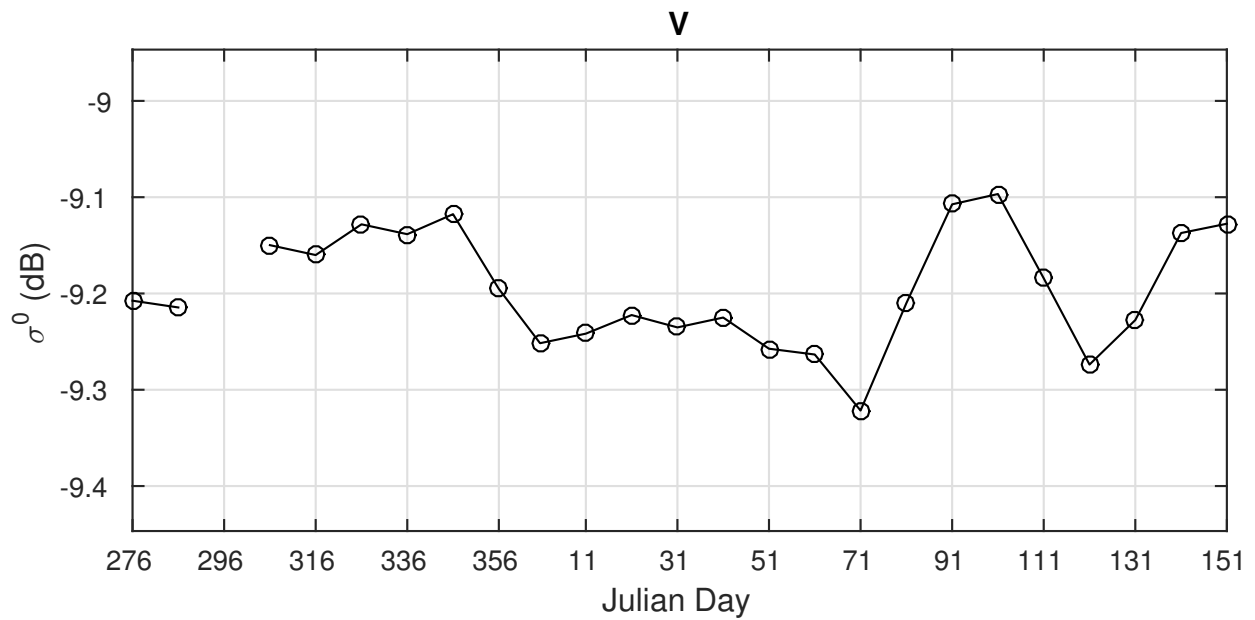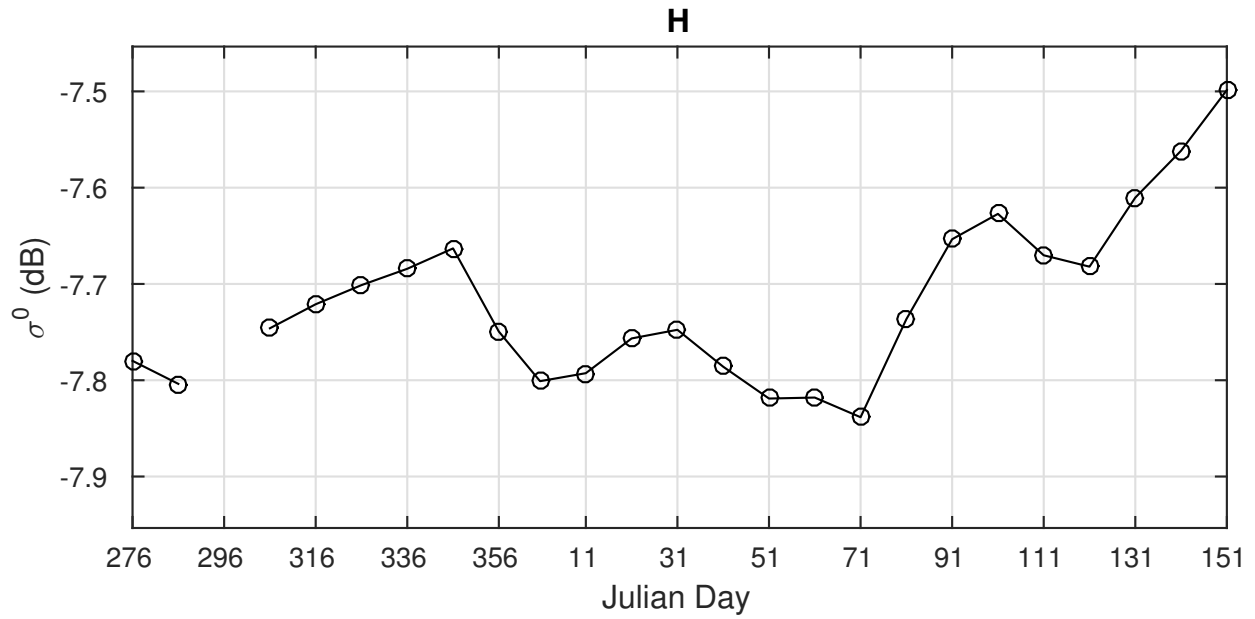
Figure 5.4: Ten day average σ^0 measured by RapidScat over the Amazon. The values have been corrected for incidence, seasonal, and diurnal variation.
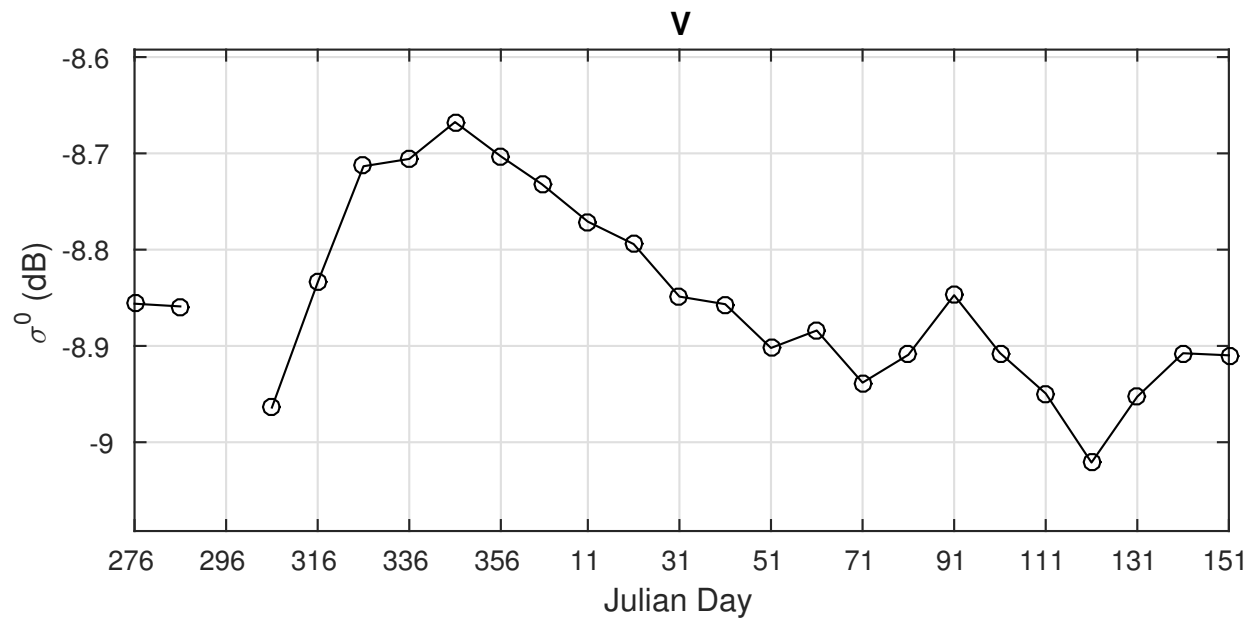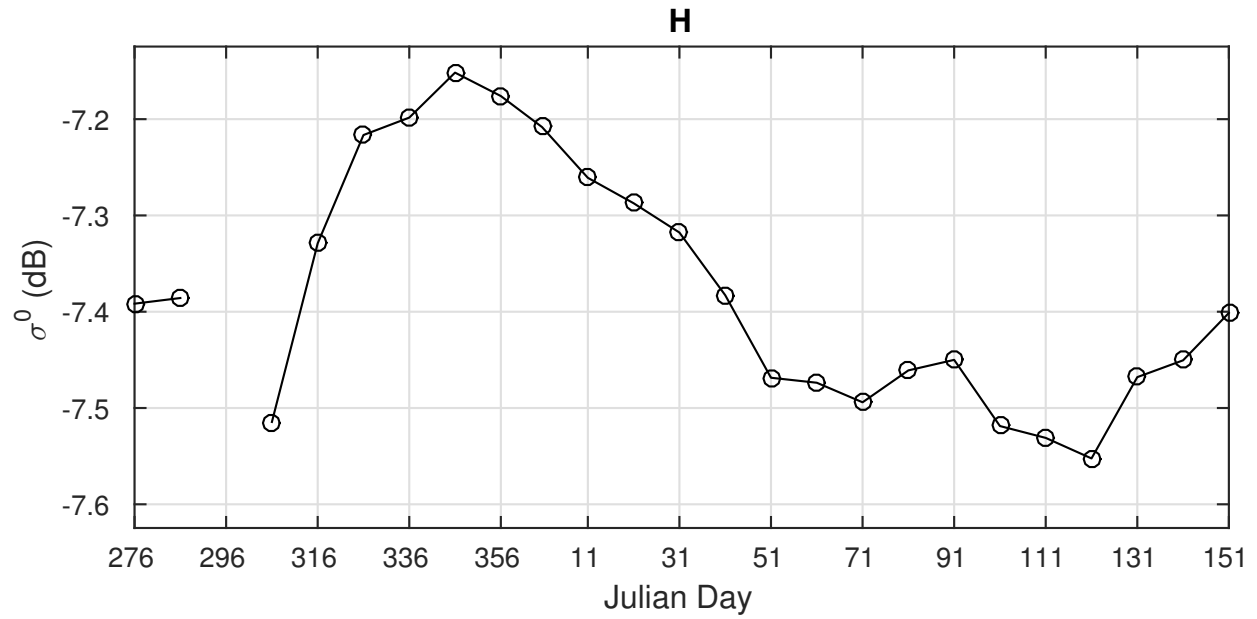
Figure 5.5: Ten day average σ^0 measured by RapidScat over the Congo. The values have been corrected for incidence, seasonal, and diurnal variation.
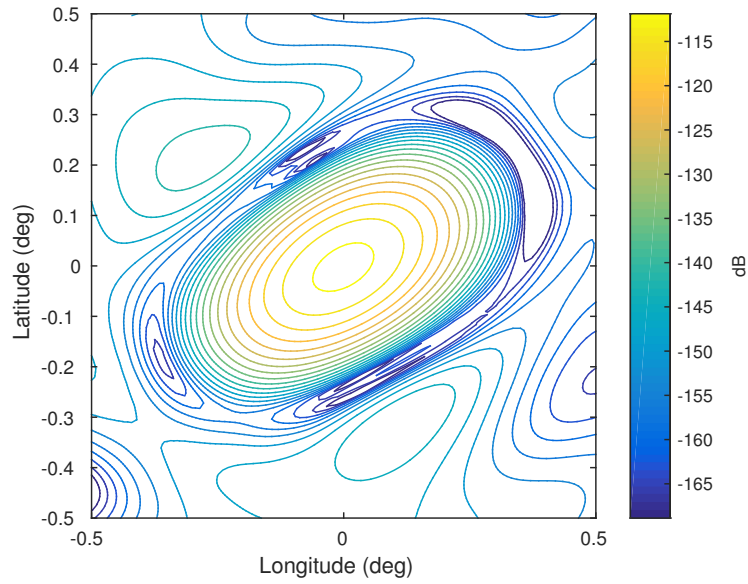
Figure 5.6: Contour plot of the spatial response function for a RapidScat egg measurement.
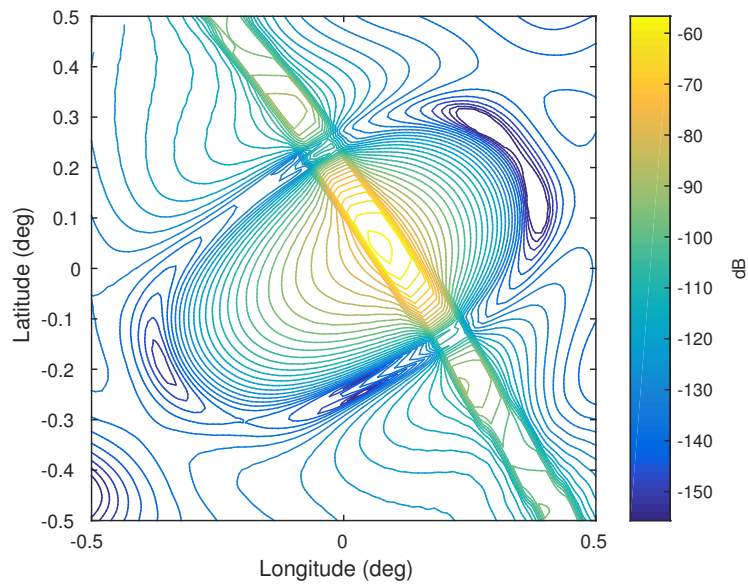
Figure 5.7: Contour plot of the spatial response function for a particular RapidScat slice measurement.
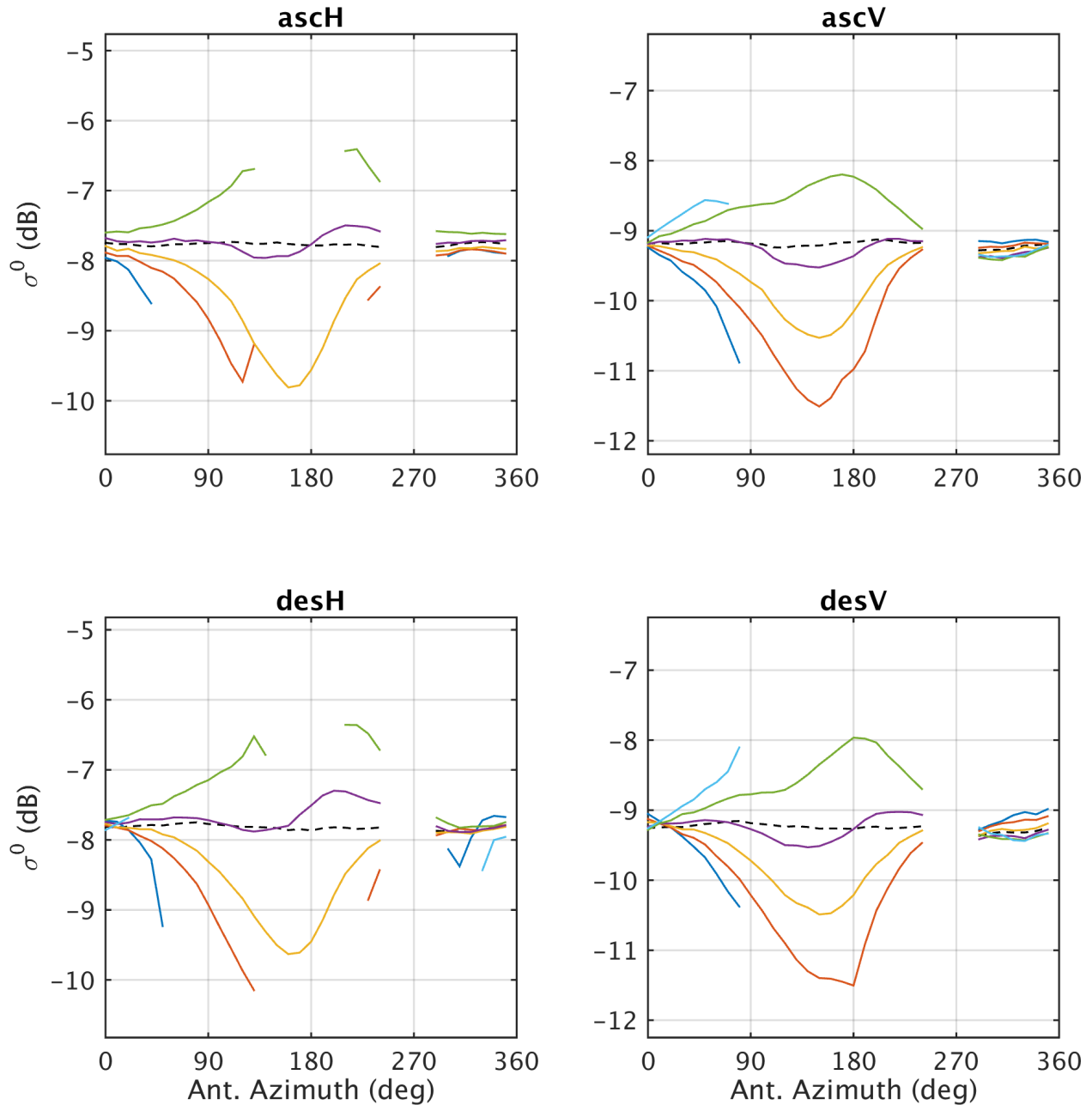
Figure 5.8: Average σ^0 over the Amazon for the six inner slices and the egg measurement (dotted line) for days 276-330, 2014. This period is before slice balancing was performed. The mean ISS pitch during this period is 0.53° The data has been corrected for incidence.

almost directly aft. A similar bias pattern occurred in QuikSCAT data at the beginning of its mission [6].

As with QuikSCAT an azimuth dependent bias correction is applied to the RapidScat data by JPL. Unfortunately the correction is not as effective as the QuikSCAT correction.

This is in a large measure attributable to variations in the pitch of the ISS. Figure 5.9 shows the azimuth response for each slice at a time when the ISS pitch fall within a range for which the correction was designed. Note how much smaller the differences are between the slices. The variation between slices is kept to about 1 dB. However when the ISS pitch is several degrees off what the slice balancing is set for, the balancing does not perform as well. The azimuth response for each slice at such a time is shown in Figure 5.10. Here we see even larger variations than were seen before slice balancing. Figure 5.11 shows QuikSCAT average σ^0 for each slice for comparison with RapidScat.

Another problematic symptom of the high pitch is the azimuth dependence in the egg measurement visible in Figure 5.10, particularly for V-pol. It can be seen that there are low points in the azimuth response. In Figure 5.12 it can be seen that these points correspond to the maximum and minimum incidence angles. Figure 5.13 shows the σ^0 incidence response for the same period of extreme pitch. The incidence response is expected to be similar to Figure 4.9 where the σ^0 increases approximately linearly with decreasing σ^0, but instead we see the σ^0 decreasing at either end of its range. The lower values for σ^0 at these extreme incidence angles can possible be attributed to range-gate clipping. Range-gate clipping is the loss of signal power that occurs when all of the returned pulse does not fall within the receive window.

5.4   Sensor Inter-Calibration

How RapidScat σ^0 compares with other sensors is of great interest. Understanding the differences between different sensors and their respective datasets allows the datasets to be used together in long-term studies. However, comparison is complicated by characteristics that differ between datasets such as azimuth angle, incidence angle, local time of day, and time of year. In this section, we discuss strategies to account for such dependencies, bias estimates between QuikSCAT and RapidScat, and then average σ^0 values for all Ku-band scatterometers.
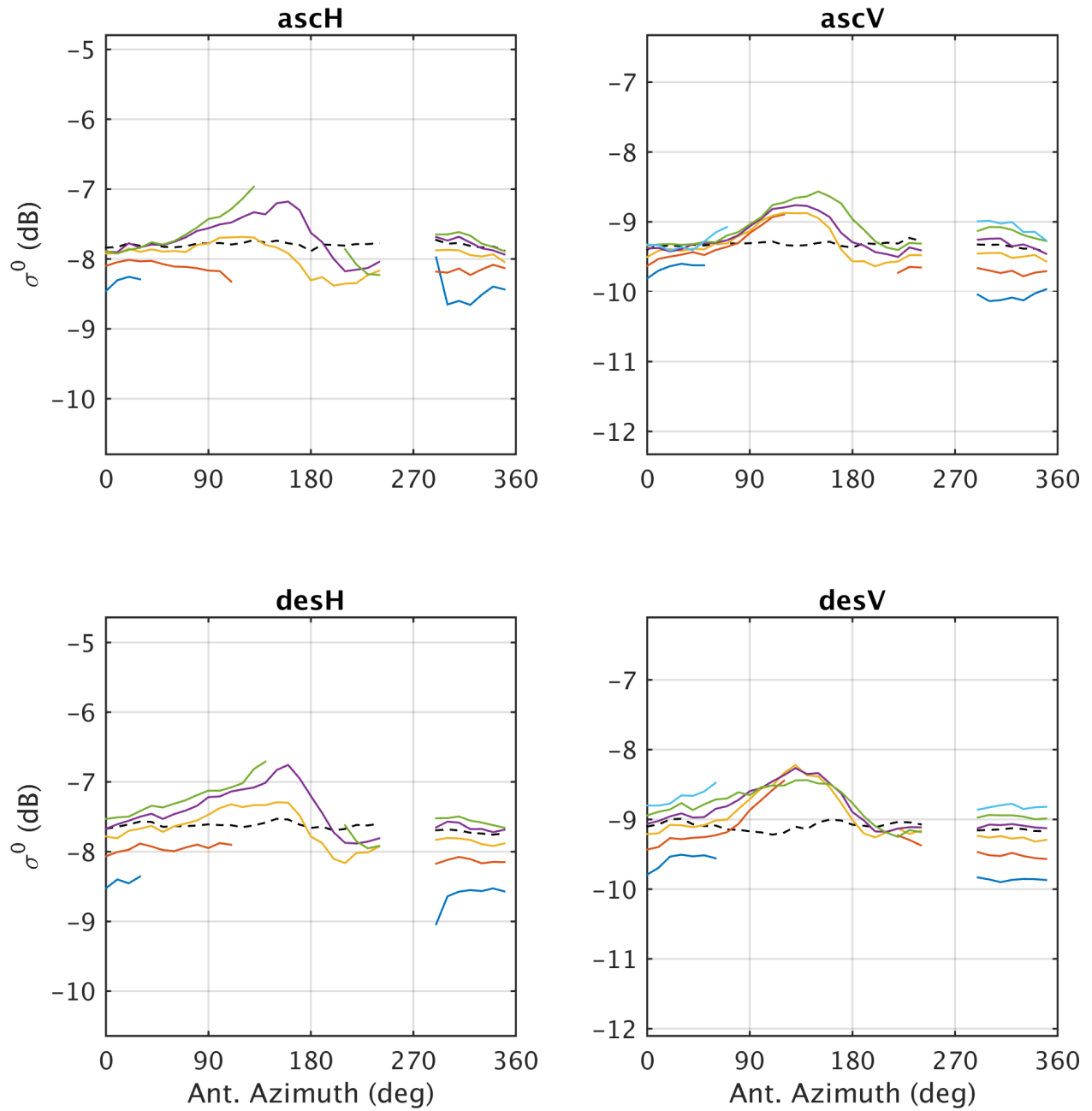
Figure 5.9: Average σ^0 over the Amazon for the six inner slices and the egg measurement (dotted line) for days 109-114, 2015. This period is after slice balancing and the mean pitch of 0.64° is close to that for which the slice balancing is based. The σ^0 has been normalized to QuikSCAT incidence.
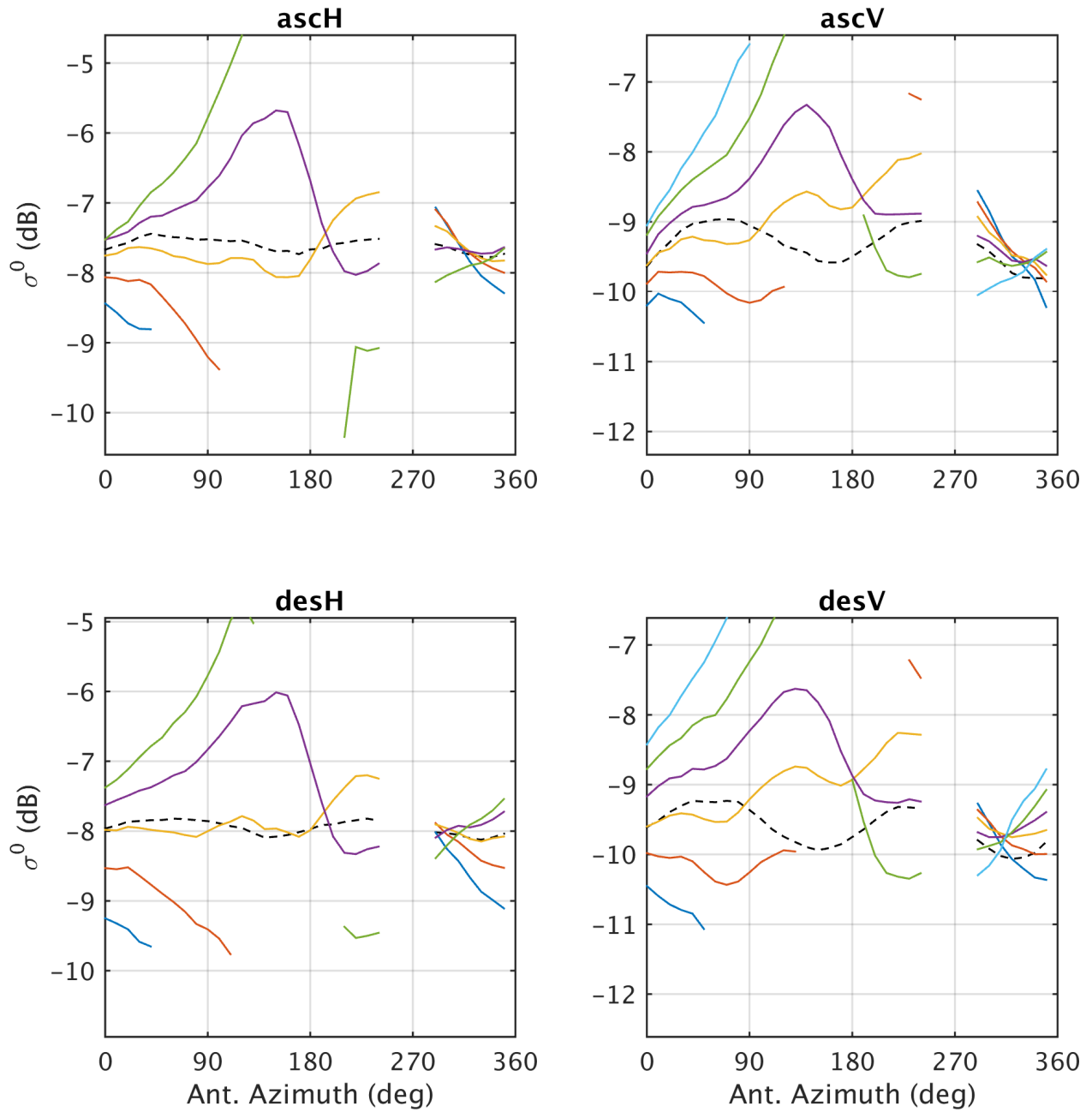
Figure 5.10: Average σ^0 over the Amazon for the six inner slices and the egg measurement (dotted line) for days 169-185, 2015. This period is after slice balancing and the mean pitch of 2.74° is far from that for which the slice balancing is based. The σ^0 has been normalized to QuikSCAT incidence.
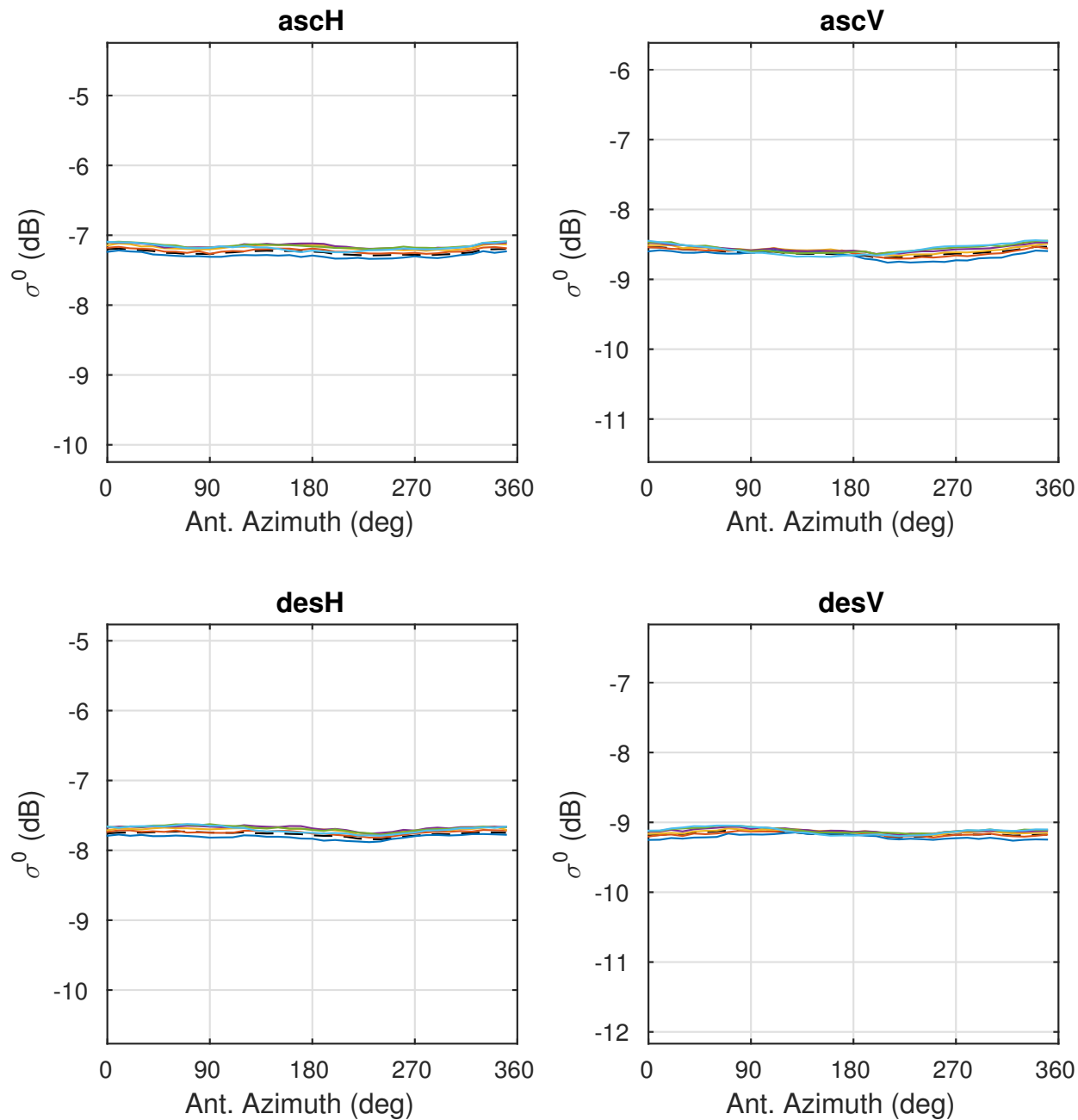
Figure 5.11: Average σ^0 over the Amazon as measured by QuikSCAT in 2009 for the six inner slices and the egg measurement (dotted line) as a function of azimuth.
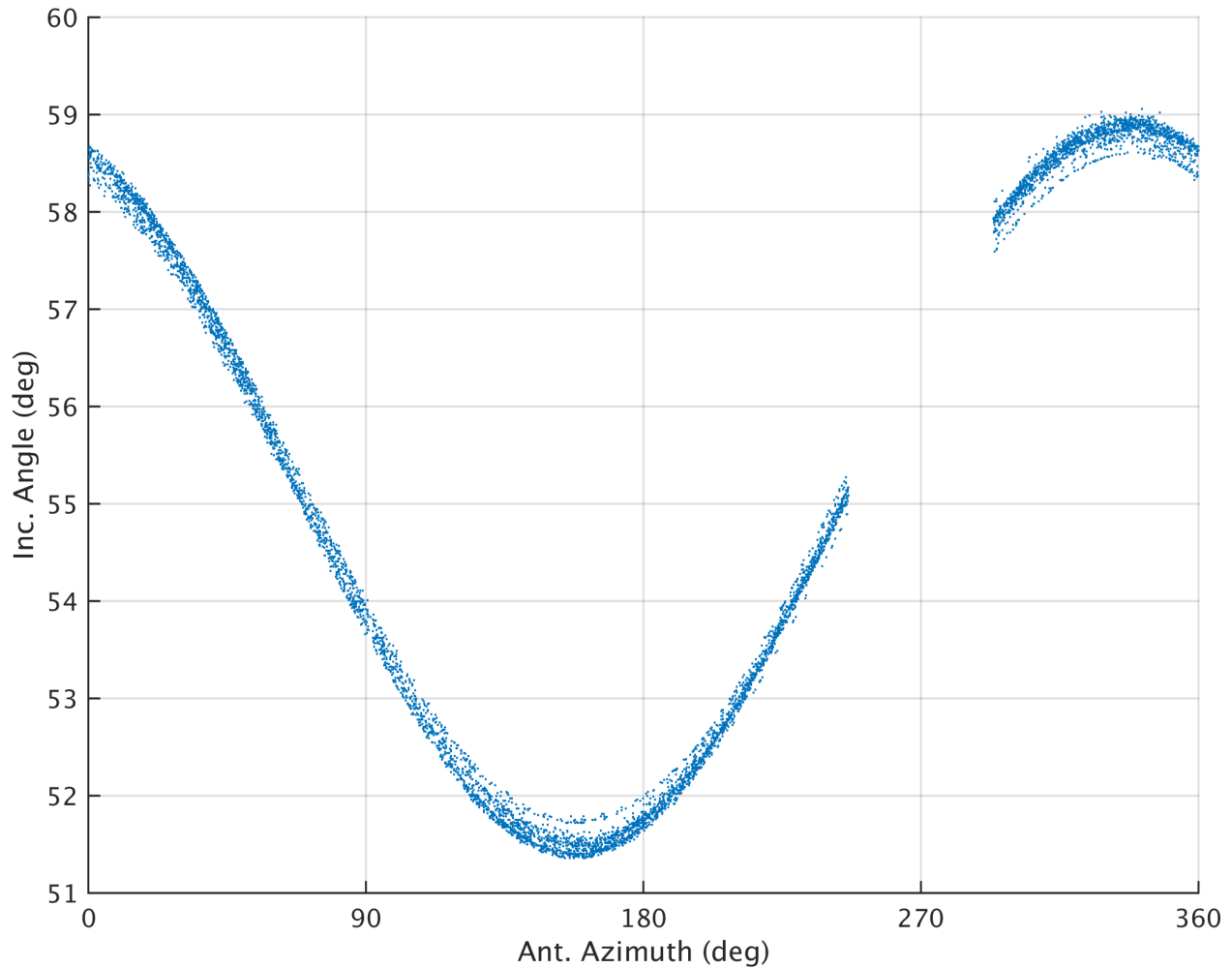
Figure 5.12: Scatter plot of incidence angle and antenna azimuth angle for V-pol measurements for days 169-185, 2015., The average pitch for this time period is 2.74°.

5.4.1 Dependency Correction

The response of the calibration targets exhibit dependencies on azimuth angle, incidence angle, location, season, and local time. When trying to estimate potential biases between two datasets, these dependencies all must be accounted for. There are different strategies that can be used to account for dependencies.

One strategy is to limit the data used for comparison. For example, QuikSCAT only measures σ^0 at two distinct local times of day while RapidScat measures σ^0 at all local times. To compare the two sensors RapidScat measurements with local times near the QuikSCAT local times are used for comparison. The rest of the data is not used to compare RapidScat

60
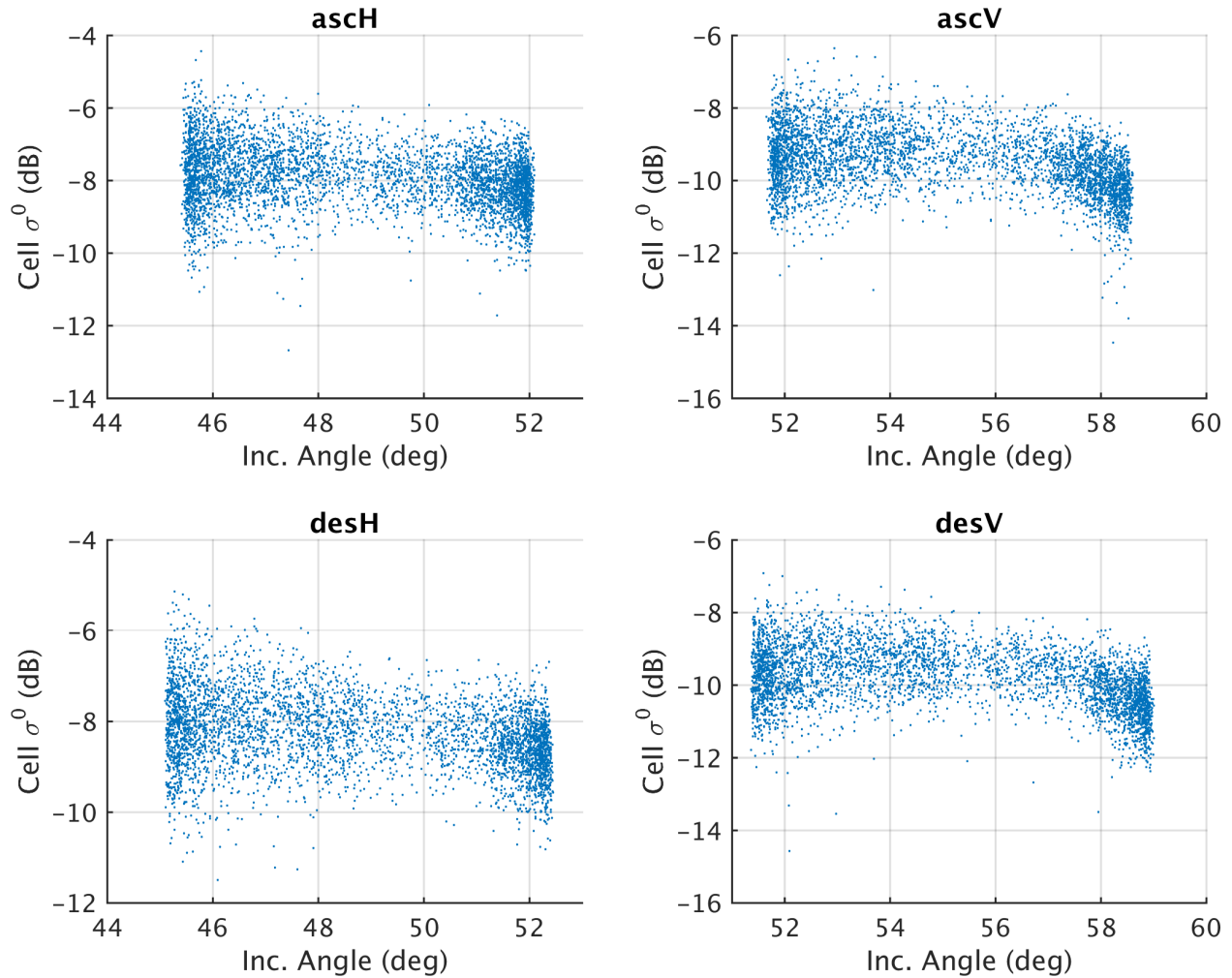
Figure 5.13: Scatter plot of σ^0 and incidence angle for days 169-185, 2015. The average pitch for this time period is 2.74°.

and QuikSCAT. This approach throws away a lot of data, but is useful because the diurnal dependence is still not completely understood.

Another strategy is to average out the dependency. This is ideal for a case like azimuth angle. Azimuth angles are sampled relatively uniformly with respect to all the other dependencies. As a result, sample sets selected for short time periods or limited areas usually contain a full range of azimuth angles. The azimuth dependence is also very small, so any imbalances in the sampling do not create a large bias.

The third strategy is to apply a correction factor to bring both datasets to a nominal value. This is often the last choice, but is necessary when the previous strategies are not

feasible. This is what is done for incidence angle. A nominal incidence angle is chosen and all measurements are normalized to that value. This is the method applied to incidence dependence. The nominal QuikSCAT incidence angles are chosen and each RapidScat measurement is normalized to that value. It works well because there is a good understanding of the incidence angle dependence at the RapidScat and QuikSCAT incidence angles and it does not change significantly with other variables.

The strategy can also depend on the dataset. The QuikSCAT PWM dataset has limited spatial sampling and for months at a time, the data is limited to a single incidence angle, a single azimuth angle, and two local times. There are no common viewing angles for different years so the first strategy cannot be used. The dependencies cannot be averaged out using the second strategy. As a result each of these variables must be normalized by applying a correction.

5.4.2 Bias Estimation Between QuikSCAT and RapidScat

QuikSCAT is the standard scatterometer to which other Ku-band scatterometers are compared. As such it is desirable to know what kind of biases may exist between RapidScat and QuikSCAT σ^0. We use four different methods to estimate the biases between QuikSCAT and RapidScat.

The first method produces a single RapidScat average σ^0 corresponding to the mission average for each flavor of QuikSCAT σ^0. Incidence angle is corrected using the correction factor estimated for RapidScat according to Equation 4.5. RapidScat measurements are limited to within one hour of 6 a.m. local time for comparison with QuikSCAT ascending and 6 p.m. for QuikSCAT descending. Spatial variations and azimuthal variations are averaged out. Since the RapidScat dataset does not yet cover a full year, we apply seasonal corrections based off Figures 4.14 and 4.15. QuikSCAT is also limited to ten complete years in estimating its average σ^0. These result in an average σ^0 value for each flavor and mask for both sensors which can then be compared. The results for such a comparison are shown in Table 5.1 under "correct season." This same method is used for the yearly averages in Subsection 5.4.3.

The second method is very similar to the first, except the QuikSCAT data used is limited to the times of year covered by RapidScat. This way both datasets cover the same

seasons and any seasonal dependencies can be averaged out instead of applying a seasonal correction to RapidScat. The resulting bias estimates can be seen in Table 5.1 under "limit season."

In the third method instead of averaging over the mask, we account for spatial variability by splitting the data into 0.2° by 0.2° latitude-longitude bins then comparing. This produces a different estimate of the bias for each spatial bin within the mask. The results are shown in Figures 5.14 and 5.15. It can be seen that there is considerable variance in the differences between corresponding spatial averages in QuikSCAT and RapidScat. This variance can be attributed to differences in weather or vegetation from year to year for certain regions, as well as the smaller number of samples that go into each comparison. A bias is clearly visible between the two sets of spatial averages, with the exception of H-pol measurements in the Congo. Also, extremely high or low spatial σ^0 averages have less correlation than those in the middle suggesting that these may be the result of extreme local weather or vegetation effects. Averaging the bias estimates with a weighting of the product of the number of QuikSCAT and RapidScat samples in the estimate gives overall bias estimates shown in Table 5.1 under "split spatially."

Another benefit of a spatial comparison is the identification of regions that experience significant change between the QuikSCAT and RapidScat missions, such as deforestation. For this we can examine the difference between QuikSCAT 2008 averages and RapidScat 2015 averages plotted as an image in Figures 5.16 and 5.17. In these images no significant regional differences are seen. This suggests that between 2008 and 2015, no regions in the mask experienced enough deforestation to noticeably decrease the backscatter response [7].

The fourth method is to split the RapidScat data by time of year and then compare those averages with QuikSCAT averages taken from the same time of year. Since data used for comparison is limited to certain local times of day, samples for comparison are taken only once per month as seen in Figure 5.18. The dotted lines indicate the range of RapidScat local times that are used for comparison with QuikSCAT. Each monthly clump of measurements is taken at a distinct time of year, averaged, and compared with the QuikSCAT average for that time of year. The results are shown in Figures 5.19 and 5.20. This gives a separate estimate of bias between QuikSCAT and RapidScat every month during the RapidScat mission life
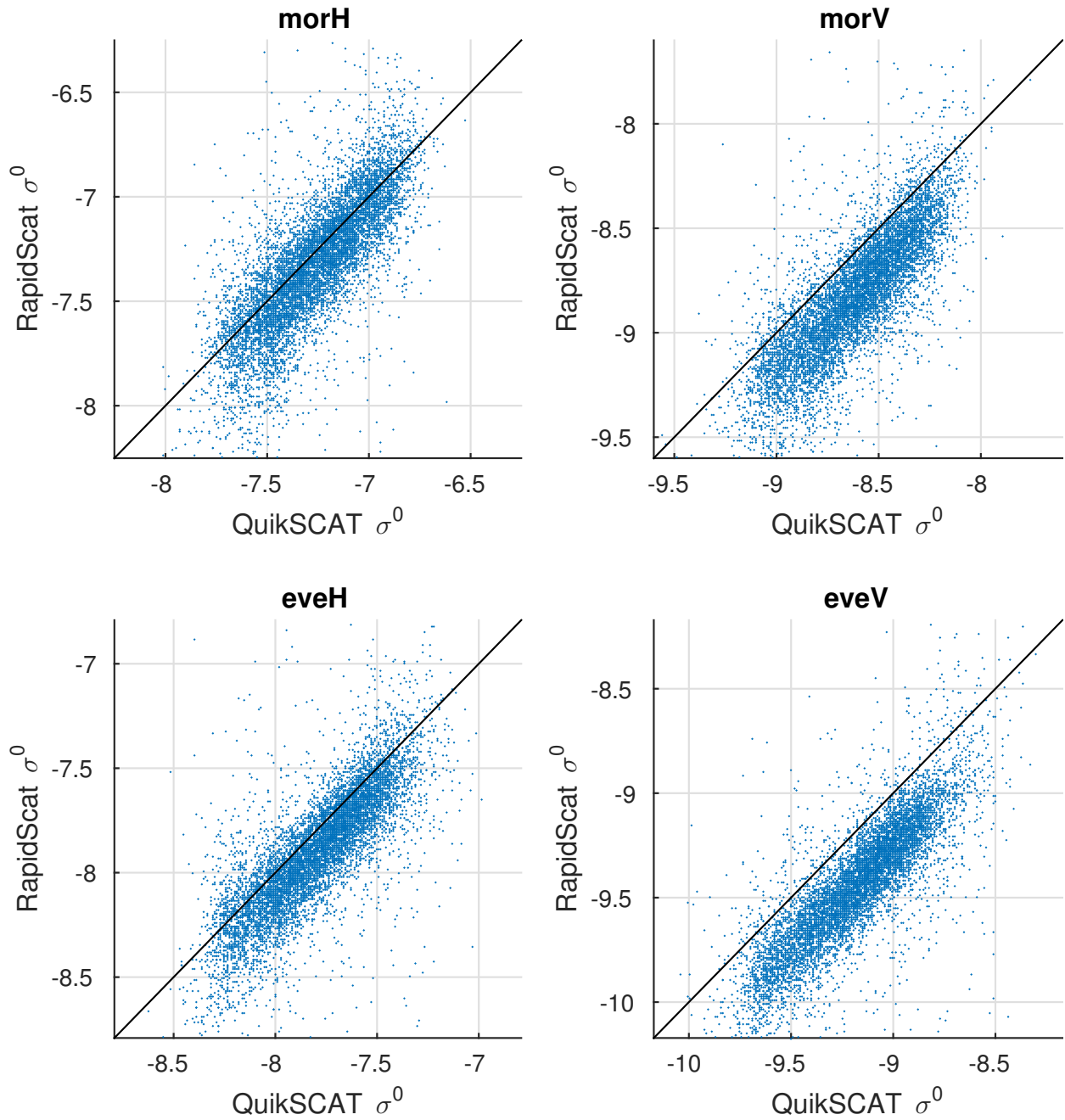
Figure 5.14: Scatter plots of QuikSCAT average σ^0 versus RapidScat average σ^0 for each 0.2° by 0.2° latitude-longitude bin within the Amazon mask. Separate plots are included for morning and evening measurements as well as H-pol and V-pol.
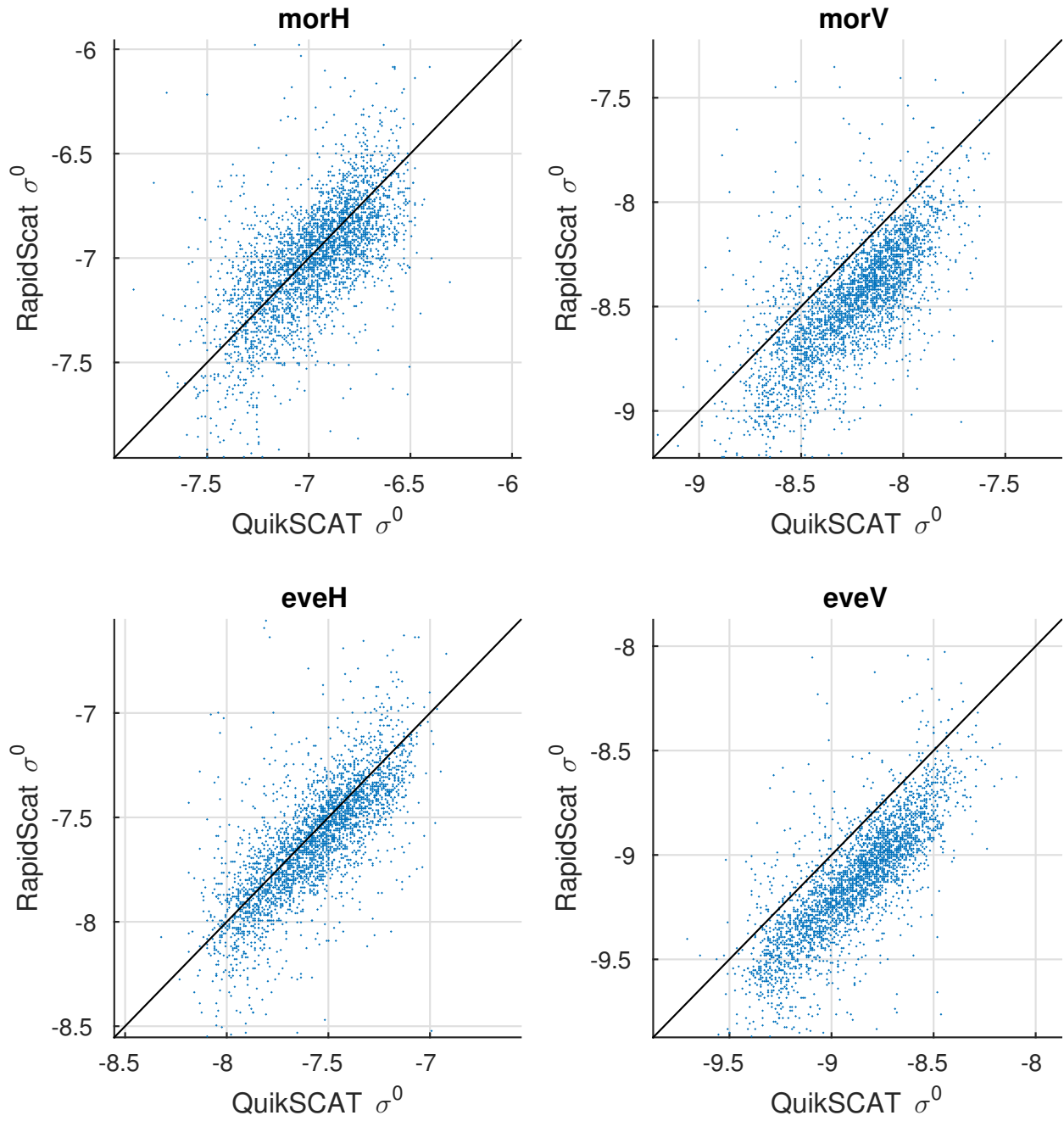
Figure 5.15: Scatter plots of QuikSCAT average σ^0 versus RapidScat average σ^0 for each $0.2°$ by $0.2°$ latitude-longitude bin within the Congo mask. Separate plots are included for morning and evening measurements as well as H-pol and V-pol.
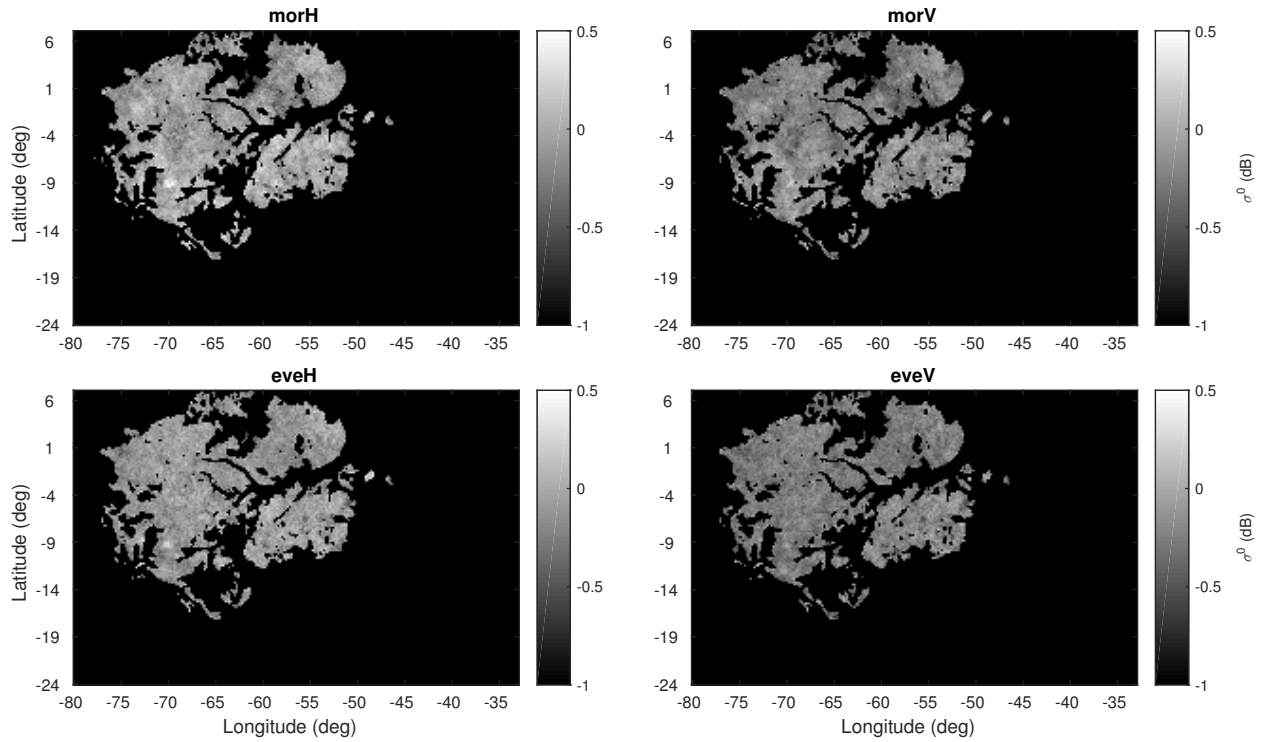
Figure 5.16: Images of QuikSCAT average σ^0 in 2008 versus RapidScat average σ^0 for each $0.2°$ by $0.2°$ latitude-longitude bin within the Amazon mask. Separate plots are included for morning and evening measurements as well as H-pol and V-pol.
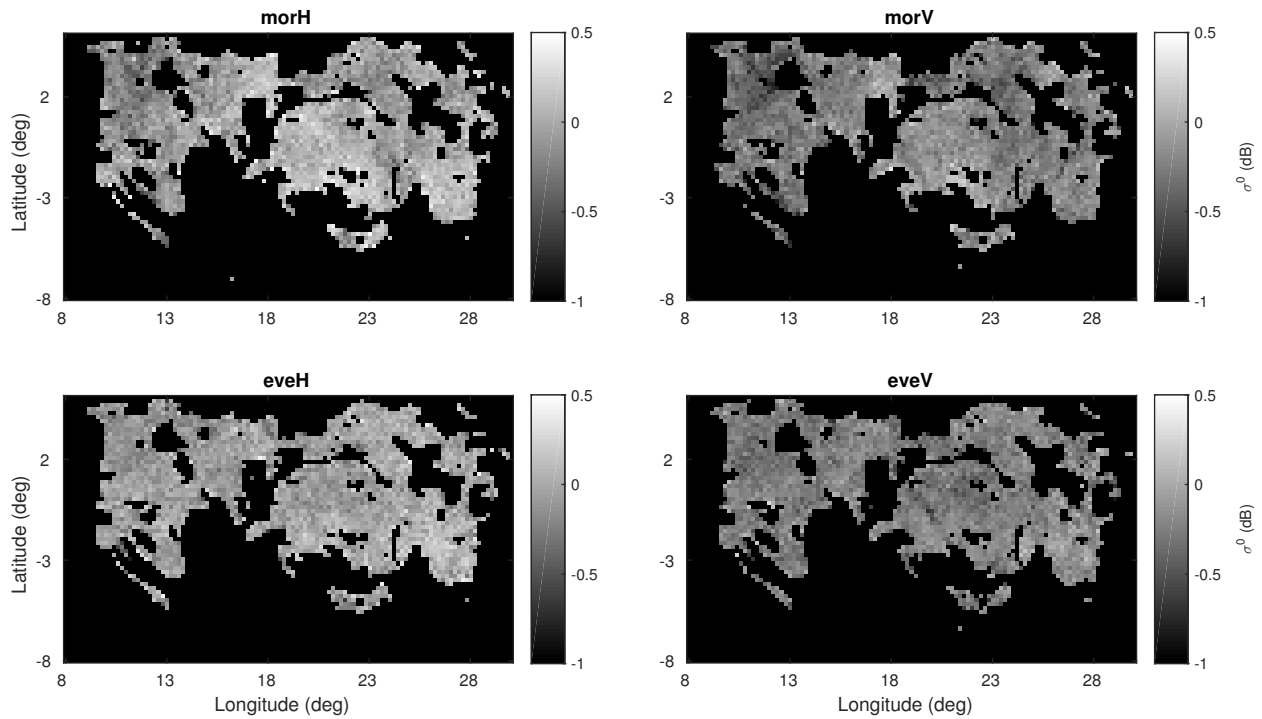
Figure 5.17: Images of QuikSCAT average σ^0 in 2008 versus RapidScat average σ^0 for each $0.2°$ by $0.2°$ latitude-longitude bin within the Congo mask. Separate plots are included for morning and evening measurements as well as H-pol and V-pol.

66
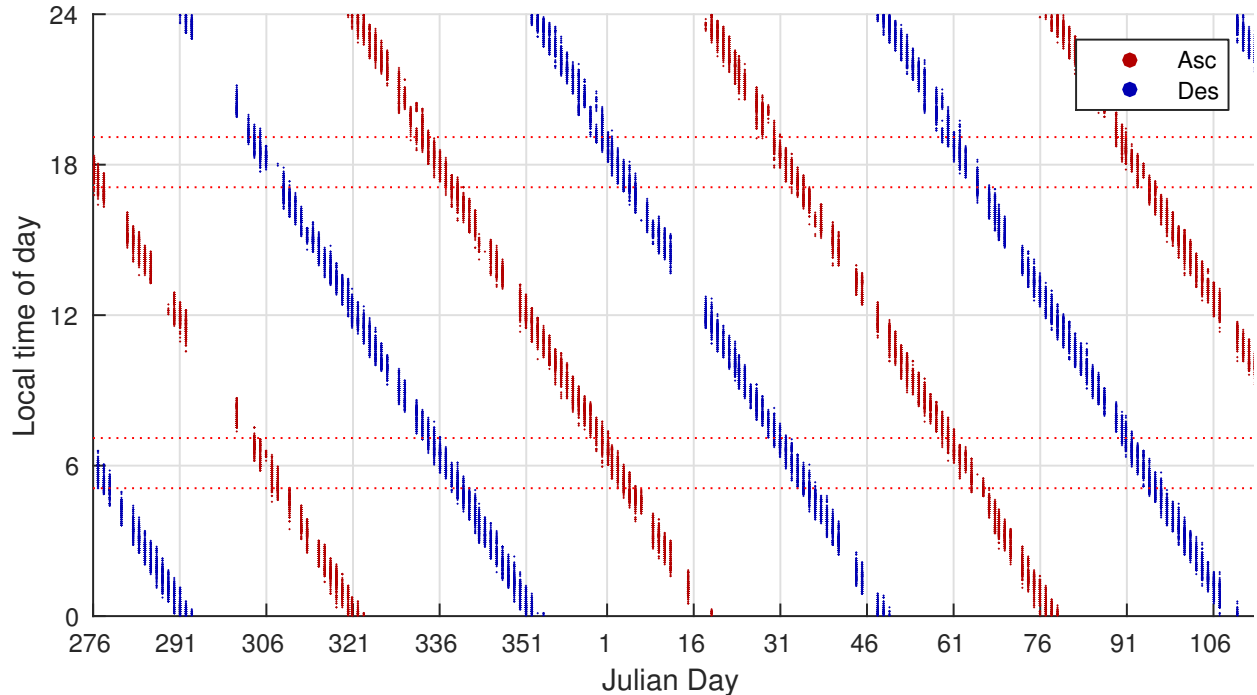
Figure 5.18: Local time of RapidScat measurements over the Amazon throughout RapidScat's mission life. Dotted lines indicate range of measurements used for comparison with QuikSCAT.

and so can also be used to estimate instrumental drift in RapidScat. There are no clear trends in the bias, though it agrees with former estimates that RapidScat is biased low compared to QuikSCAT. By averaging the bias estimates we obtain a single mean bias offset for each mask and "flavor" shown in Table 5.1.

Four different methods have been used to estimate the biases between QuikSCAT and RapidScat with all the results shown in Table 5.1. While each apply the same strategy for azimuthal, diurnal, and incidence dependencies they have varied strategies with regard to seasonal and spatial dependencies. All the estimates are consistent in that they estimate that RapidScat is biased low compared with QuikSCAT. All also agree that the bias is smaller for the H-pol (0-0.2 dB) than it is for the V-pol (0.2-0.3 dB).

5.4.3   Yearly Averages

When comparing QuikSCAT and RapidScat there is the possibility that the scattering characteristics of the targets may have changed in the time between the missions. Though there are no regions that stand out in Figures 5.16 and 5.17, there is the possibility of overall

67
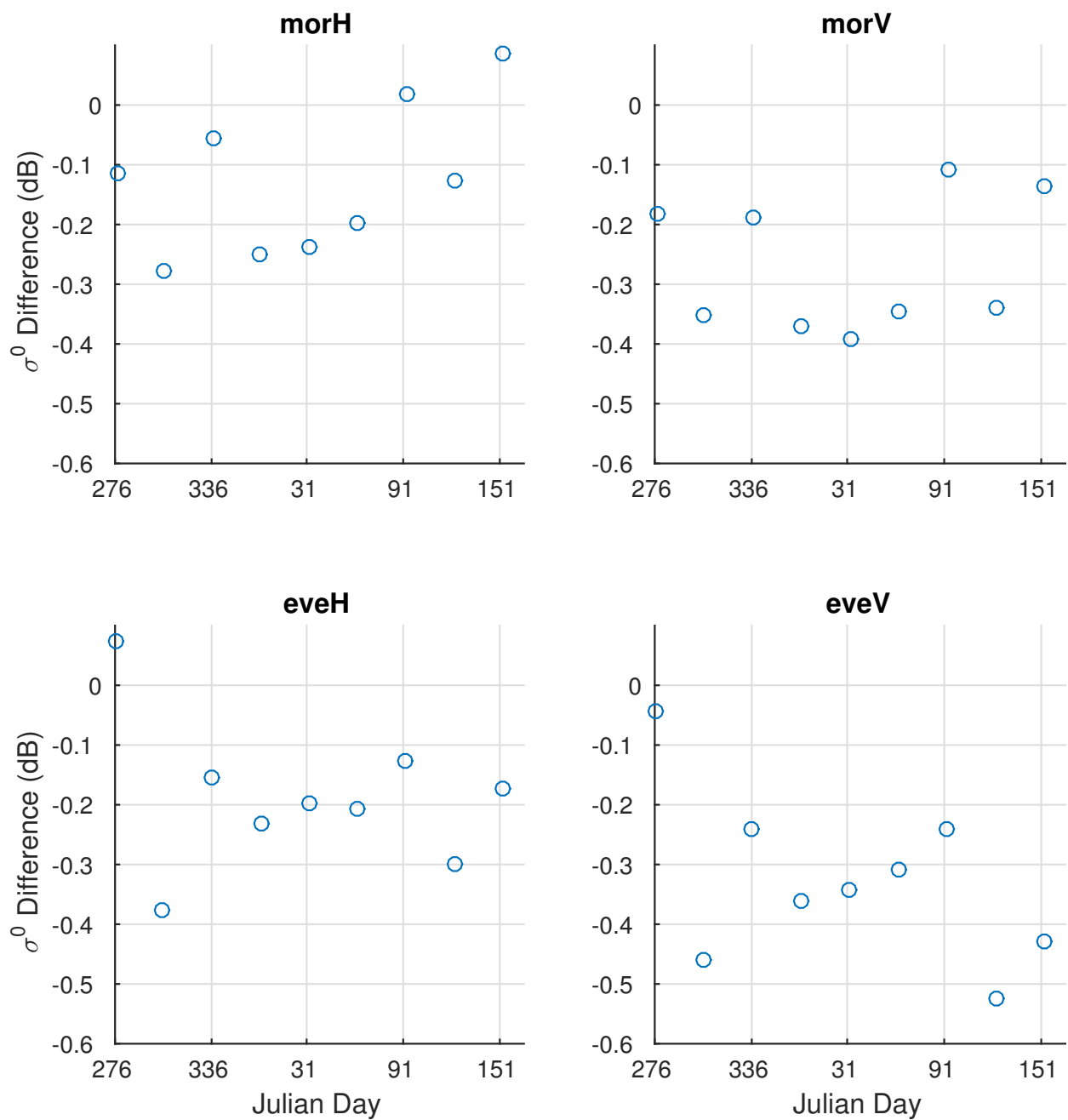
Figure 5.19: Difference between RapidScat mean σ^0 for different times of year and the QuikSCAT average for that time of year. RapidScat is normalized to QuikSCAT incidence before comparison. Amazon.
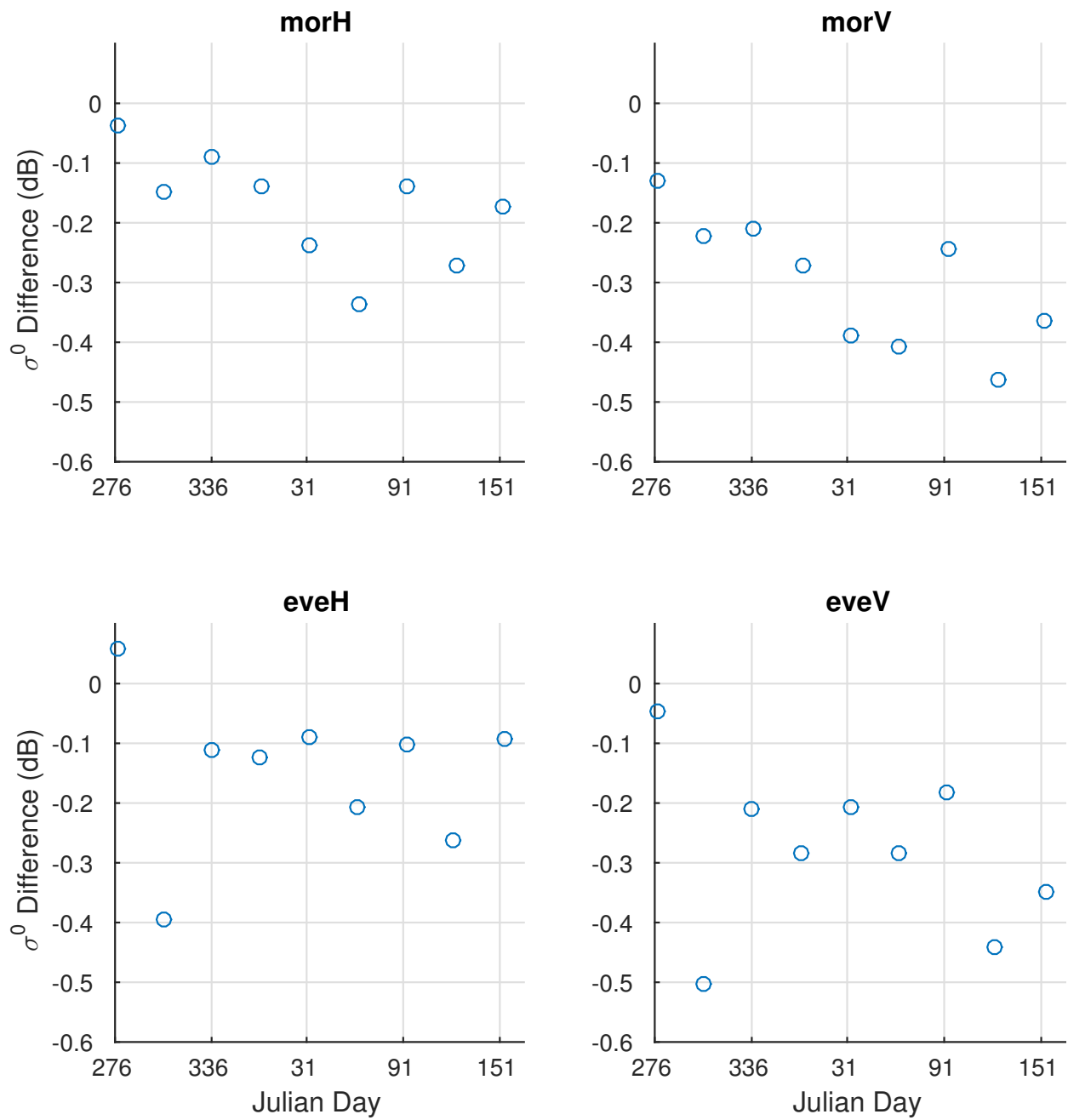
Figure 5.20: Difference between RapidScat mean σ^0 for different times of year and the QuikSCAT average for that time of year. RapidScat is normalized to QuikSCAT incidence before comparison. Congo.

Table 5.1: Difference between RapidScat average σ^0 for 6 a.m. and 6 p.m. and QuikSCAT mean ascending and descending σ^0 using a variety of methods.

Method	Region	MorH	MorV	EveH	EveV
Correct Season	Ama	-0.1163	-0.2289	-0.1686	-0.2937
	Con	-0.0652	-0.2089	-0.0999	-0.2542
Limit Season	Ama	-0.0838	-0.2240	-0.1444	-0.2933
	Con	-0.0282	-0.1993	-0.0760	-0.2563
Split Spatially	Ama	-0.0807	-0.2311	-0.1437	-0.2949
	Con	-0.0309	-0.2154	-0.0756	-0.2612
Split Seasonally	Ama	-0.1282	-0.2678	-0.1869	-0.3278
	Con	-0.1749	-0.3004	-0.1518	-0.2854

vegetation or climate changes that affect the whole region. In order to address this, and also to compare σ^0 from different Ku-band scatterometers, we look at the year to year behavior of the calibration targets as measured by NSCAT, QuikSCAT, QuikSCAT PWM, OSCAT, and RapidScat.

The most obvious choice for evaluating possible target variation between the QuikSCAT and the RapidScat wind missions is the QuikSCAT post wind mission dataset. However, this dataset has some characteristics that must be accounted for. First, the data is limited to certain times of year as shown in Table 2.1. A seasonal correction based in the results in Section 4.4 must be applied to this data. Next, since the azimuth angle is fixed over those same time periods, an azimuth correction is also applied based in the results in Section 4.2. An incidence angle correction is applied using the same correction factor derived from RapidScat data. Lastly, due to its extremely narrow swath width it does not spatially sample the entire target like the other sensors. As a result a spatial correction is also applied based on the results in Section 4.5. Each of these corrections have their own empirical errors, and may have inter-dependencies that are not accounted for, which can introduce biases into the yearly averages.

We estimate yearly average σ^0 for RapidScat, NSCAT, and OSCAT. Each must have their σ^0 adjusted for different variables to correspond with QuikSCAT σ^0. RapidScat is normalized as discussed in the previous subsection. NSCAT and OSCAT have two primary variables to consider. The first is incidence. NSCAT measurements used for comparison are first limited to measurements within 2° of QuikSCAT incidence and then the linear correction

factor estimated from NSCAT data is applied. OSCAT uses the RapidScat correction factor due to the similarities between the RapidScat and OSCAT systems. The NSCAT and OSCAT yearly averages are then adjusted to the QuikSCAT local time of day using the diurnal cycle measured by RapidScat in Section 4.4.

After applying these corrections the averages shown in Figures 5.21 and 5.22 are obtained. The continuous chain of 10 years of QuikSCAT averages are relatively consistent, with more variation for the H-pol ascending averages. The NSCAT averages are shown to be biased high by 0.5-0.7 dB. The QuikSCAT PWM averages are not very consistent, showing considerably different behavior for the four different flavors over the three years of data available. This is likely due to the relatively small number of samples used to create these averages, and the large number of corrections applied to the data. OSCAT is shown to be relatively consistent during the three years of data (2011-2013) used for these averages. There are, however, definite biases that are dependent on the flavor. The differences between ascending and descending passes could be due to imperfections in the diurnal correction. RapidScat is consistently biased low compared to QuikSCAT as shown in Subsection 5.4.2.
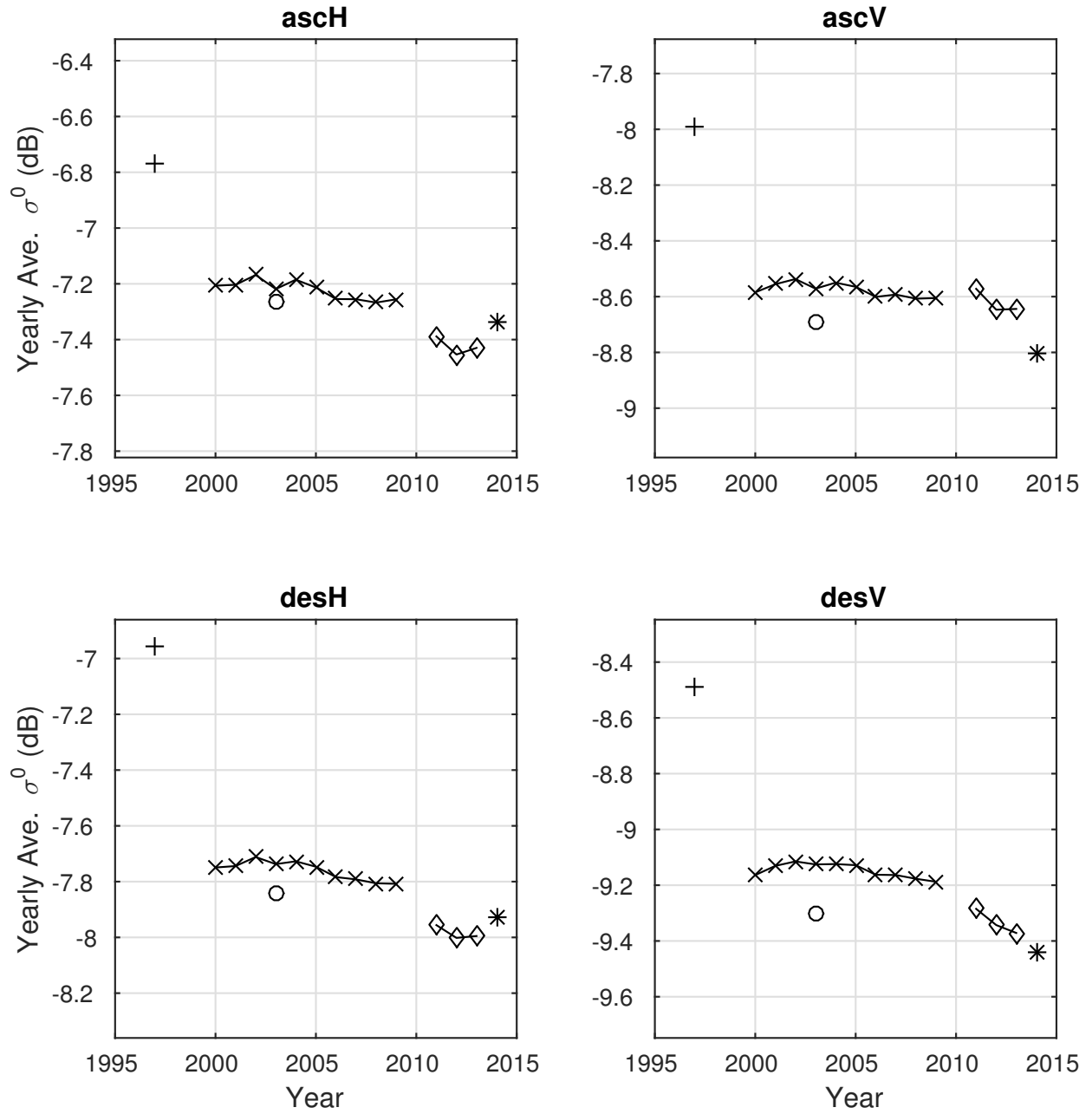
Figure 5.21: Yearly average σ^0 for QuikSCAT ($\times$), QuikSCAT PWM data ($\square$), RapidScat ($*$), OSCAT ($\lozenge$), and NSCAT ($+$) over the Amazon.

72
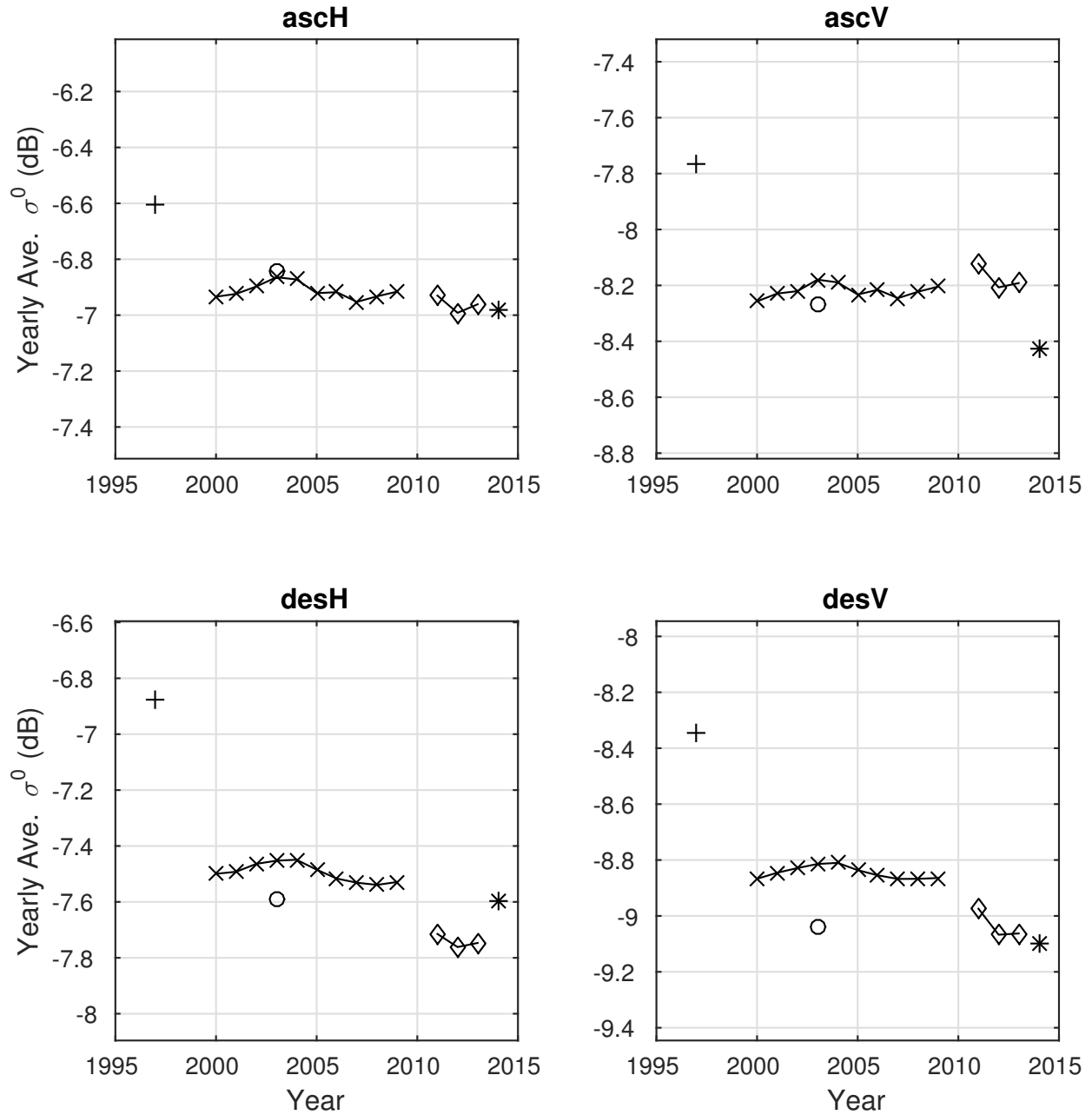
Figure 5.22: Yearly average σ^0 for QuikSCAT ($\times$), QuikSCAT PWM data ($\square$), RapidScat ($*$), OSCAT ($\Diamond$), and NSCAT ($+$) over the Congo.

73

Chapter 6

Conclusions

Data from three different Ku-band scatterometers, NSCAT, QuikSCAT and Rapid-Scat, are used to characterize the azimuth, incidence, spatial, seasonal, and diurnal dependencies present in two natural land targets, the Amazon and Congo rainforests. These dependencies are then used to compare σ^0 readings between different scatterometers, in particular RapidScat and QuikSCAT.

The land targets are selected to be homogeneous targets with minimal dependencies. The spatial dependency is limited to a single dB in the mask selection process. Azimuthal dependency is measured using QuikSCAT and is found to be less than ±0.1 dB. It is likely to have components related to azimuthal dependencies in the target itself as well azimuthal biases in the instrument itself. Incidence dependence is measured using RapidScat, NSCAT, and QuikSCAT post-wind mission data. The estimates agree reasonably well. Differences between the RapidScat and NSCAT measurements can be attributed to differences in σ^0 retrieval and incidence balancing between the two systems. The seasonal dependency is measured over multiple years using QuikSCAT and is estimated to be less than ±0.25 dB. For the first time, the diurnal dependency of the Amazon and Congo rainforests are measured. The diurnal signal is found to be almost ±0.5 dB in magnitude. The measured diurnal cycle explains differences seen between QuikSCAT ascending and descending passes. These dependencies are all used to create an observation model for σ^0 measurements over the target.

The empirical observation model is used to validate the RapidScat data record. Slice balancing is evaluated applying an incidence angle correction and examining the azimuth response of each slice. The slice balancing is found to have reduced the slice dependency significantly, but dependencies still exist on the order of 1 dB. The effectiveness also depends strongly on the pitch of the ISS. The long term stability of RapidScat is evaluated by applying

a diurnal, seasonal, and incidence angle correction to RapidScat data. It is shown that the RapidScat average varies by less that 0.3 dB over the mission life.

Inter-calibration is performed by using the observation model to account for differences in characteristics between sensors. Yearly average σ^0 values are found for QuikSCAT, QuikSCAT PWM, RapidScat, OSCAT, and NSCAT after compensating for differences in incidence angle, azimuth angle, local time of day, and time of year. Different methods are explored for estimating mean biases between RapidScat and QuikSCAT. RapidScat is estimated to be biased low compared to QuikSCAT. The magnitude of the bias varies with the estimation method, but ranges from 0.02–0.19 dB for H-pol and 0.20–0.33 dB for V-pol.

Overall RapidScat is shown to be a consistent scatterometer, with a small negative σ^0 bias compared to QuikSCAT.

6.1 Contributions

The primary contributions of this thesis are:

1. The ability of RapidScat to accurately measure diurnal signals is demonstrated over the Amazon and Congo.

2. RapidScat cell σ^0 is found to be generally accurate and to exhibit the same behavior over the calibration targets as previous scatterometers.

3. The slice balancing is shown to be highly dependent on the current pitch of the platform which should be considered before using the data. Slice balancing for different pitches is recommended.

4. RapidScat instrument drift is found to be less than 0.3 dB over the mission life.

5. RapidScat σ^0 is shown to be biased slightly low compared to QuikSCAT. For those interested in combining the two datasets this bias can be corrected for in the RapidScat dataset to give a more consistent data record. This record can then be used for long term studies of geophysical parameters such as soil moisture or vegetation density.

6.2 Future Work

Potential future research includes:

1. Results enumerated in this thesis can be confirmed by using other calibration targets. Targets with different behavior than tropical rainforests may reveal other behavior in the instruments not seen using only the Amazon and the Congo.

2. Previous calibration attempts can be reviewed in light of the diurnal response characterized in this thesis.

3. The observation model in this thesis is entirely empirical. A more accurate and perhaps simpler model could be developed by considering geophysical parameters and their effect on the backscatter. Variations and biases in our empirical model could be explained by fluctuations in the geophysical parameters.

Bibliography

[1] F. T. Ulaby and D. G. Long, *Microwave radar and radiometric remote sensing.* University of Michigan Press Ann Arbor, 2014.

[2] D. G. Long and M. R. Drinkwater, "Azimuth variation in microwave scatterometer and radiometer data over Antarctica," *Geoscience and Remote Sensing, IEEE Transactions on*, vol. 38, no. 4, pp. 1857–1870, 2000.

[3] M. W. Spencer, C. Wu, and D. G. Long, "Improved resolution backscatter measurements with the SeaWinds pencil-beam scatterometer," *Geoscience and Remote Sensing, IEEE Transactions on*, vol. 38, no. 1, pp. 89–104, 2000.

[4] Brandir, "Heliosynchronous orbit.svg," Online: https://commons.wikimedia.org/wiki/File:Heliosynchronous_orbit.svg, April 2014, creative Commons Attibution-Share Alike 3.0 Unported License.

[5] F. Naderi, M. Freilich, and D. Long, "Spaceborne radar measurement of wind velocity over the ocean-an overview of the NSCAT scatterometer system," *Proceedings of the IEEE*, vol. 79, no. 6, pp. 850–866, 1991.

[6] J. N. Huddleston, W. Tsai, M. W. Spencer, B. W. Stiles, and R. S. Dunbar, "SeaWinds on QuikSCAT: Postlaunch calibration and validation," in *Geoscience and Remote Sensing Symposium, 2000. Proceedings. IGARSS 2000. IEEE 2000 International*, vol. 3. IEEE, 2000, pp. 1024–1026.

[7] S. Jaruwatanadilok and B. W. Stiles, "Trends and variation in Ku-band backscatter of natural targets on land observed in QuikSCAT data," *Geoscience and Remote Sensing, IEEE Transactions on*, vol. 52, no. 7, pp. 4383–4390, 2014.

[8] I. S. Ashcraft, D. G. Long, A. Anderson, S. L. Richards, M. Spencer, and B. Jones, "σ retrieval from SeaWinds on QuikScat," in *SPIE's International Symposium on Optical Science, Engineering, and Instrumentation.* International Society for Optics and Photonics, 1999, pp. 171–178.

[9] T. Yu and R. D. Mcpherson, "Global data assimilation experiments with scatterometer winds from SEASAT-A," *Monthly Weather Review*, vol. 112, no. 2, pp. 368–376, 1984.

[10] D. Anderson, A. Hollingsworth, S. Uppala, and P. Woiceshyn, "A study of the use of scatterometer data in the European Centre for Medium-Range Weather Forecasts operational analysis-forecast model: 1. quality assurance and validation," *Journal of Geophysical Research: Oceans (1978–2012)*, vol. 96, no. C2, pp. 2619–2634, 1991.

[11] R. Atlas, R. Hoffman, S. Leidner, J. Sienkiewicz, T. Yu, S. Bloom, E. Brin, J. Ardizzone, J. Terry, D. Bungato, *et al.*, "The effects of marine winds from scatterometer data on weather analysis and forecasting," *Bulletin of the American Meteorological Society*, vol. 82, no. 9, pp. 1965–1990, 2001.

[12] D. B. Chelton, M. H. Freilich, J. M. Sienkiewicz, and J. M. Von Ahn, "On the use of QuikSCAT scatterometer measurements of surface winds for marine weather prediction," *Monthly Weather Review*, vol. 134, no. 8, pp. 2055–2071, 2006.

[13] J. D. Hawkins and P. G. Black, "Seasat scatterometer detection of gale force winds near tropical cyclones," *Journal of Geophysical Research: Oceans (1978–2012)*, vol. 88, no. C3, pp. 1674–1682, 1983.

[14] Y. Quilfen, B. Chapron, T. Elfouhaily, K. Katsaros, and J. Tournadre, "Observation of tropical cyclones by high-resolution scatterometry," *Journal of Geophysical Research: Oceans (1978–2012)*, vol. 103, no. C4, pp. 7767–7786, 1998.

[15] W. Wagner, G. Lemoine, and H. Rott, "A method for estimating soil moisture from ERS scatterometer and soil data," *Remote Sensing of Environment*, vol. 70, no. 2, pp. 191–207, 1999.

[16] Q. P. Remund and D. G. Long, "Sea ice extent mapping using Ku band scatterometer data," *Journal of Geophysical Research: Oceans (1978–2012)*, vol. 104, no. C5, pp. 11 515–11 527, 1999.

[17] Q. P. Remund, D. G. Long, and M. R. Drinkwater, "An iterative approach to multisensor sea ice classification," *Geoscience and Remote Sensing, IEEE Transactions on*, vol. 38, no. 4, pp. 1843–1856, 2000.

[18] S. Nghiem, I. Rigor, D. Perovich, P. Clemente-Colon, J. Weatherly, and G. Neumann, "Rapid reduction of Arctic perennial sea ice," *Geophysical Research Letters*, vol. 34, no. 19, 2007.

[19] L. Prevot, I. Champion, and G. Guyot, "Estimating surface soil moisture and leaf area index of a wheat canopy using a dual-frequency (C and X bands) scatterometer," *Remote Sensing of Environment*, vol. 46, no. 3, pp. 331–339, 1993.

[20] W. Wagner, G. Lemoine, M. Borgeaud, and H. Rott, "A study of vegetation cover effects on ERS scatterometer data," *Geoscience and Remote Sensing, IEEE Transactions on*, vol. 37, no. 2, pp. 938–948, 1999.

[21] D. G. Long and P. J. Hardin, "Vegetation studies of the Amazon basin using enhanced resolution Seasat scatterometer data," *Geoscience and Remote Sensing, IEEE Transactions on*, vol. 32, no. 2, pp. 449–460, 1994.

[22] S. Frolking, K. McDonald, J. Kimball, J. Way, R. Zimmermann, and S. Running, "Using the space-borne NASA scatterometer (NSCAT) to determine the frozen and thawed seasons," *Journal of Geophysical Research: Atmospheres (1984–2012)*, vol. 104, no. D22, pp. 27 895–27 907, 1999.

[23] R. R. Forster, D. G. Long, K. C. Jezek, S. D. Drobot, and M. R. Anderson, "The onset of Arctic sea-ice snowmelt as detected with passive-and active-microwave remote sensing," *Annals of Glaciology*, vol. 33, no. 1, pp. 85–93, 2001.

[24] M. R. Drinkwater, D. G. Long, and A. W. Bingham, "Greenland snow accumulation estimates from satellite radar scatterometer data," *Journal of Geophysical Research: Atmospheres (1984–2012)*, vol. 106, no. D24, pp. 33 935–33 950, 2001.

[25] S. V. Nghiem and W. Tsai, "Global snow cover monitoring with spaceborne Ku-band scatterometer," *Geoscience and Remote Sensing, IEEE Transactions on*, vol. 39, no. 10, pp. 2118–2134, 2001.

[26] M. Gade, W. Alpers, H. Hühnerfuss, V. R. Wismann, and P. A. Lange, "On the reduction of the radar backscatter by oceanic surface films: Scatterometer measurements and their theoretical interpretation," *Remote Sensing of Environment*, vol. 66, no. 1, pp. 52–70, 1998.

[27] R. D. Lindsley and D. G. Long, "Mapping surface oil extent from the Deepwater Horizon oil spill using ASCAT backscatter," *Geoscience and Remote Sensing, IEEE Transactions on*, vol. 50, no. 7, pp. 2534–2541, 2012.

[28] K. Stuart and D. Long, "Tracking large tabular icebergs using the SeaWinds Ku-band microwave scatterometer," *Deep Sea Research Part II: Topical Studies in Oceanography*, vol. 58, no. 11, pp. 1285–1300, 2011.

[29] Jet Propulsion Laboratories. (2015) Winds: Measuring ocean winds from space. [Online]. Available: https://winds.jpl.nasa.gov

[30] W. Tsai, J. E. Graf, C. Winn, J. N. Huddleston, S. Dunbar, M. H. Freilich, F. J. Wentz, D. G. Long, and W. L. Jones, "Postlaunch sensor verification and calibration of the NASA scatterometer," *Geoscience and Remote Sensing, IEEE Transactions on*, vol. 37, no. 3, pp. 1517–1542, 1999.

[31] A. Elyouncha and X. Neyt, "C-band satellite scatterometer intercalibration," *Geoscience and Remote Sensing, IEEE Transactions on*, vol. 51, no. 3, pp. 1478–1491, 2013.

[32] A. Stoffelen, "A simple method for calibration of a scatterometer over the ocean," *Journal of atmospheric and oceanic technology*, vol. 16, no. 2, pp. 275–282, 1999.

[33] M. Satake and H. Hanado, "Diurnal change of Amazon rain forest $\sigma 0$ observed by Ku-band spaceborne radar," *Geoscience and Remote Sensing, IEEE Transactions on*, vol. 42, no. 6, pp. 1127–1134, 2004.

[34] I. Birrer, E. Bracalente, G. Dome, J. Sweet, and G. Berthold, "σ^0 signature of the Amazon rain forest obtained from the Seasat scatterometer," *Geoscience and Remote Sensing, IEEE Transactions on*, no. 1, pp. 11–17, 1982.

[35] R. G. Kennett and F. K. Li, "Seasat over-land scatterometer data. II. selection of extended area and land-target sites for the calibration of spaceborne scatterometers," *Geoscience and Remote Sensing, IEEE Transactions on*, vol. 27, no. 6, pp. 779–788, 1989.

[36] D. G. Long and G. B. Skouson, "Calibration of spaceborne scatterometers using tropical rain forests," *Geoscience and Remote Sensing, IEEE Transactions on*, vol. 34, no. 2, pp. 413–424, 1996.

[37] J. Zec, D. G. Long, and W. L. Jones, "NSCAT normalized radar backscattering coefficient biases using homogenous land targets," *Journal of Geophysical Research: Oceans (1978–2012)*, vol. 104, no. C5, pp. 11 557–11 568, 1999.

[38] J. Zec, W. L. Jones, and D. G. Long, "SeaWinds beam and slice balance using data over Amazonian rainforest," in *Geoscience and Remote Sensing Symposium, 2000. Proceedings. IGARSS 2000. IEEE 2000 International*, vol. 5. IEEE, 2000, pp. 2215–2217.

[39] L. B. Kunz and D. G. Long, "Calibrating SeaWinds and QuikSCAT scatterometers using natural land targets," *Geoscience and Remote Sensing Letters, IEEE*, vol. 2, no. 2, pp. 182–186, 2005.

[40] J. C. Barrus, "Intercalibration of QuikSCAT and OSCAT land backscatter," Master's thesis, Brigham Young University, 2013.

[41] S. A. Bhowmick, R. Kumar, and A. K. Kumar, "Cross calibration of the OceanSAT-2 scatterometer with QuikSCAT scatterometer using natural terrestrial targets," *Geoscience and Remote Sensing, IEEE Transactions on*, vol. 52, no. 6, pp. 3393–3398, 2014.

[42] M. A. Bourassa, E. Rodriguez, and R. Gaston, "NASA's ocean vector winds science team workshops," *Bulletin of the American Meteorological Society*, vol. 91, no. 7, pp. 925–928, 2010.

[43] Wikipedia, "Sun-synchronous orbit — Wikipedia, the free encyclopedia," 2015, [Online; accessed 9-July-2015]. [Online]. Available: https://en.wikipedia.org/w/index.php?title=Sun-synchronous_orbit

[44] A. C. Paget, D. G. Long, and N. M. Madsen, "RapidSCAT diurnal cycles over land," *Geoscience and Remote Sensing, IEEE Transactions on*, submitted.

[45] D. G. Long, P. J. Hardin, and P. T. Whiting, "Resolution enhancement of spaceborne scatterometer data," *Geoscience and Remote Sensing, IEEE Transactions on*, vol. 31, no. 3, pp. 700–715, 1993.

[46] J. A. Marengo, B. Liebmann, V. E. Kousky, N. P. Filizola, and I. C. Wainer, "Onset and end of the rainy season in the Brazilian Amazon Basin," *Journal of Climate*, vol. 14, no. 5, pp. 833–852, 2001.

[47] B. Liebmann and J. Marengo, "Interannual variability of the rainy season and rainfall in the Brazilian Amazon Basin," *Journal of Climate*, vol. 14, no. 22, pp. 4308–4318, 2001.

Appendix A

RapidScat X-factor Tabulation

A scatterometer transmits a microwave pulse at a target and measures the power of the returned signal. The relation between the returned power and the variable of interest, the normalized radar cross-section (σ^0), can be summarized in a single term, X. At the time of the SeaWinds scatterometer's design in the late 1990s, it was not feasible to calculate this term "on the fly" for every pulse. As a result, a look-up table was developed at the BYU MERS laboratory that gives an accurate X with the input of only four parameters. This table was used for the entire mission when SeaWinds was launched aboard QuikSCAT.

In preparation for the launch of RapidScat, another SeaWinds scatterometer, the MERS laboratory was tasked with adapting the code used to generate the X-table for the new system. An X-table of the same format was required to avoid changes to the processing code. In Sections A.1 and A.2, a brief overview is given of X-factor calculation and tabularization as performed for QuikSCAT. The changes needed to adapt X tabularization for the RapidScat system are explained in Section A.3.

A.1 X-factor Calculation

The X-factor is used to relate the power received (P_r) by the scatterometer to the σ^0 of the target. It is calculated using the radar equation:

$$P_r = \sigma^0_{\text{avg}} \frac{P_t}{(4\pi)^3} \iint \frac{G(x,y)^2 F(x,y) g(x,y)}{R(x,y)^4} \, dx \, dy, \tag{A.1}$$

where σ^0_{avg} is the weighted average of σ^0 over the footprint, G is the antenna gain, R is the slant range to the target, P_t is the transmitted power, g is a loss term related to range-gate clipping, and F is a term related to range-Doppler processing. The terms g and F are unique to the RapidScat system. The integral and all other terms can be combined into the term X leaving the relation:

$$P_r = \sigma^0_{\text{avg}} X,$$
$$X = \frac{P_t}{(4\pi)^3} \iint \frac{G(x,y)^2 F(x,y) g(x,y)}{R(x,y)^4} \, dx \, dy. \tag{A.2}$$

X, in general, changes with each pulse as the position and the viewing angle of the sensor change.

In order to calculate X, the integral in Equation A.2 is numerically evaluated. This is done by calculating $\frac{G(x,y)^2 F(x,y)}{R(x,y)^4}$ for each point in a grid covering the footprint, then nu-
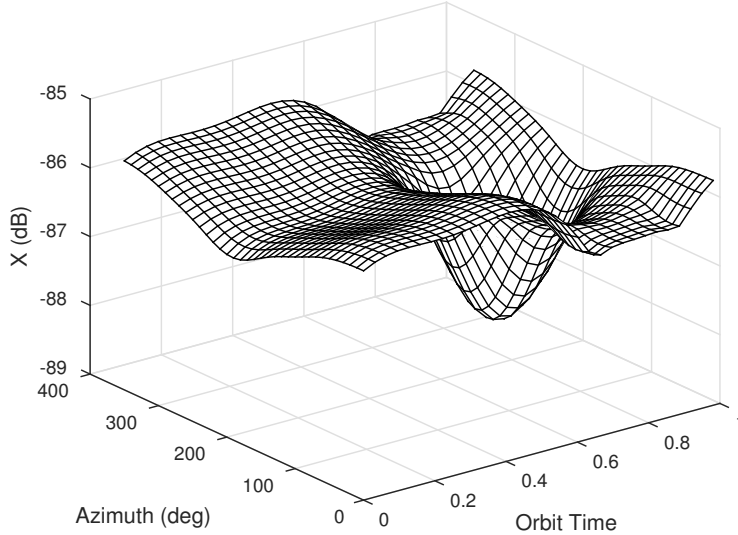
Figure A.1: X_{nom} for "egg" measurements calculated at 36 azimuth angles by 32 orbit times.

merically integrating. The range-gating term, g, was not included in the calculation for QuikSCAT because its effect was found to be insignificant [8].

The antenna gain G and the range R can easily be calculated using standard orbital geometry, but the processor response F is unique to the instrument. SeaWinds employs a chirped signal and a digital processor to give range discrimination. The frequency of the returned signal after being mixed to baseband depends on the range of the scatterer from the sensor. In addition, relative motion of the scatterer causes a Doppler shift in frequency. The FFT of the baseband signal is calculated and the power in a range of FFT bins are summed to give a power measurement for each "slice." The processor gain, F, is the sum of several squared sinc function corresponding to the baseband frequency and FFT bins in a slice. The squared sinc function shape is due to the rectangular window on the pulse. Summing the power from the inner ten slices gives the "egg" measurement [3].

A.2 X-factor Tabularization for QuikSCAT

Most variations in X are easily parameterized for the QuikSCAT system with just two parameters, the antenna azimuth angle, and the orbit time (time since the ascending node crossing) [8]. Figure A.1 shows X calculated for 36 azimuth angles by 32 orbit times. Note the smooth continuous response to orbit time and azimuth angle. These values for X are referred to as nominal X or X_{nom}.

This parameterization was generally effective, but in order to increase the accuracy of the table a perturbation correction was added. Perturbations in the instrument's attitude or orbit during the mission alter the actual X resulting in an inaccurate table. To correct for these inaccuracies another parameter was needed. Such a parameter was found in Δf, the difference between the predicted and the actual baseband frequency at electrical boresight (point of highest antenna gain). The relation between Δf and X was found to be smooth for various perturbations to orbit parameters and attitude. This smooth relation can be seen
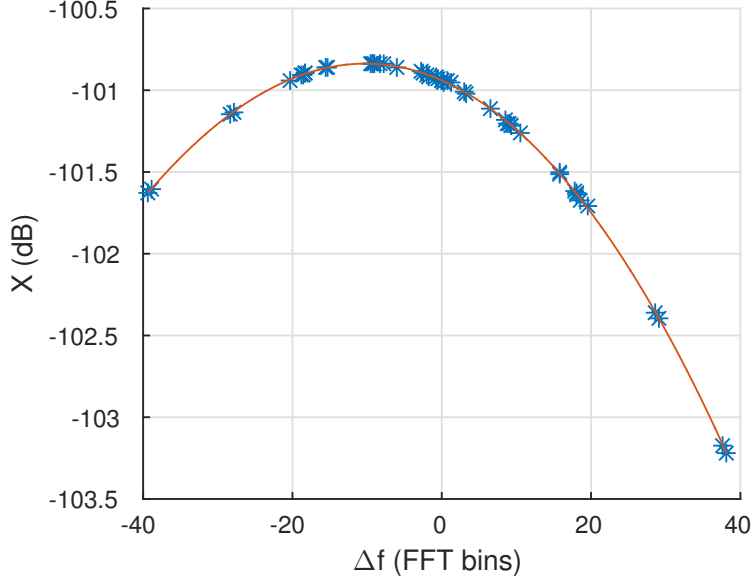
Figure A.2: X and Δf for various perturbations of orbit and attitude for an orbit time of 0 and antenna azimuth angle of 0. A third-order polynomial is fit to the points.

in Figure A.2. This relation can be approximated using a third-order polynomial:

$$X_{\text{pert}} = X_{\text{nom}} + A + B\Delta f + C\Delta f^2 + D\Delta f^3, \tag{A.3}$$

where X_{pert} is the X value after the perturbation correction and the coefficients A–D are the coefficients of the polynomial fit of X to Δf.

The shape of this polynomial is generally different for each orbit time and azimuth angle, so the coefficient A–D are calculated for each azimuth angle and orbit time. This is done by perturbing the position and attitude at each point, calculating X and Δf, then finding the coefficients of the third-order polynomial. During QuikSCAT operation, X_{nom}, A, B, C, and D are found by bilinearly interpolating the table using the pulse's orbit time and azimuth angle. The Δf value calculated for the pulse is then entered into Equation A.3 to give the estimate for X.

All the calculations of X are performed assuming a perfect ellipsoid earth, without regard for the local topographical height. This topographical height can also affect X. A linear correction S for the topographical height, Sh_{topo}, can be used to adjust Δf according to:

$$\Delta f_{\text{tot}} = \Delta f + Sh_{\text{topo}}. \tag{A.4}$$

Using the Δf_{tot} that has been adjusted for topography in Equation A.3 yields an estimate for X that meets QuikSCAT mission requirements. Thus X can be accurately estimated with four parameters, the orbit time, the antenna azimuth angle, Δf, and the topographical height.

A.3 Adaptation to RapidScat

A number of changes were necessary to adapt the X-table generation code for the RapidScat system. The changes were for the most part not necessitated by changes in the instrument (which was almost identical), but rather by changes in the platform. The QuikSCAT scatterometer had a dedicated satellite, set in a stable orbit with few, small perturbations in its orbit and its attitude. RapidScat, on the other hand, is mounted on the International Space Station (ISS), a satellite intended for much more than simply providing a platform for a sensor.

The orbit and attitude for the ISS is not as simple as QuikSCAT's. The QuikSCAT X-table code defines the orbit with the five Keplerian parameters and assumes zero roll, pitch, and yaw for the nominal X. The ISS orbit on the other hand precesses at five times the rate of QuikSCAT's orbit, and the roll and pitch regularly vary by several degrees within a single orbit. In order to accommodate this, the X-table generation code is adjusted to accept input files giving actual position and attitude data from an ISS orbit in the form of a sequence of Cartesian position and velocity values with roll, pitch, and yaw. This data is then used to calculate the X_{nom}-table, instead of assuming an ideal Keplerian orbit with zero roll, pitch, and yaw. Perturbations are performed around these points to calculate the coefficients in Equation A.3. The size of the perturbations used is increased to account for the larger range of perturbations expected on the ISS.

A table specifically designed for a particular orbit of the ISS loses accuracy as the ISS orbit and attitude change. This is opposed to QuikSCAT where a single table was used for the entire mission. Operations occurring on the ISS can affect the orbit and the attitude. The ISS altitude is also low enough that it loses altitude quickly without regular boosts. With all these factors, an X-table quickly loses its accuracy. Figure A.3 shows the increase in tabularization errors as the same table is used for subsequent orbits. After two and a half days the RMS error for slices goes beyond 0.1 dB. It is recommended to update the table with new orbit and attitude data often to maintain accuracy.

Range-gate clipping also is a major concern with RapidScat, unlike with QuikSCAT. This is due in part to the fact that SeaWinds was intended for a higher orbit (RapidScat is at approximately half altitude of QuikSCAT). Range-gate clipping is the loss of signal power that occurs when all of the returned pulse does not fall within the receive window. As an approximation for this phenomena, the term $g(x, y)$ is added to the radar equation. It is the proportion of the returned pulse that falls within the range-gate for each point in the footprint. For QuikSCAT the term was essentially always one, but it can vary considerably for RapidScat.

The above changes were made to the BYU X-table generation code and the performance was evaluated by comparing tabulated values with values that were directly computed. Tabulation errors can be kept under 0.1 dB by updating the X-table daily. The table generation code has been incorporated into the JPL processing code and is used to generate the standard JPL data products.
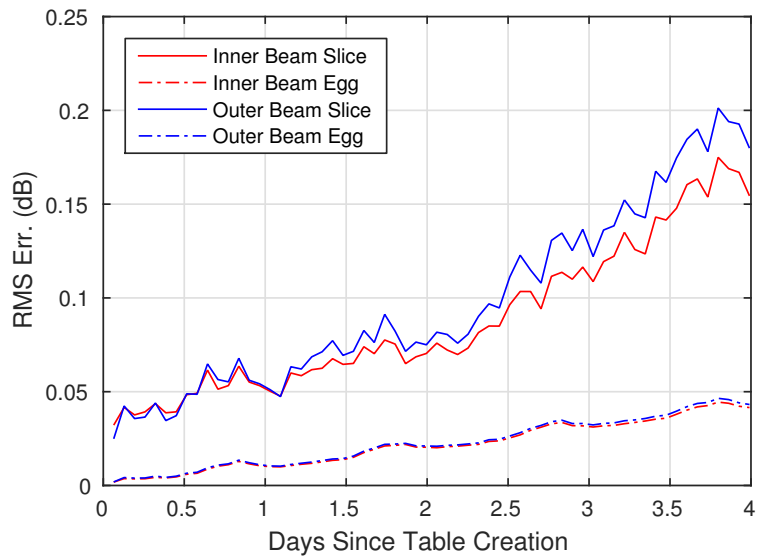
Figure A.3: RMS errors for using the same table for multiple days after creation. Four days of consecutive ISS ephemeris data used. X-table is created with ephemeris data on day 0. Directly computed X is compared with X retrieved from table to generate the RMS errors.

Appendix B

Sub-mask Dependencies

In Chapter 4, the σ^0 dependencies on time and viewing angle are estimated for the two calibration targets. In this section, we estimate whether such dependencies are characteristic of all regions within the mask. In order to do this we define smaller regions within both the Amazon and Congo masks and evaluate the dependencies for each smaller region.

Two strategies for splitting the mask are explored. The first is to divide by mean σ^0. The reasoning is that areas with similar mean σ^0 also have similar vegetation or climate that results in similar behavior with respect to time and viewing angle. Three masks are created. One mask with mean σ^0 values within ± 0.1 dB of the mean for the entire mask, one with higher means, and one with lower means. The 0.1 dB boundary was chosen so that each mask had approximately the same number of samples. The second strategy is to select distinct contiguous regions, since adjacent areas tend to have similarities in vegetation type and climate. The regions selected by each strategy are shown for the Amazon and Congo in Figures B.1 and B.2 respectively.

Azimuth dependency for each sub-region is estimated by dividing the data into azimuth bins and averaging. The results are shown in Figures B.3 and B.4 for sub-regions based on contiguous regions and in Figures B.5 and B.6 for sub-regions based on mean σ^0 response. Figures B.3 and B.4 show that that different regions can have different azimuth responses suggesting that the azimuth response is can vary considerably throughout the mask, but is still of the same magnitude. The regions split by mean σ^0 all show very similar azimuth responses that are also very similar to the overall average, suggesting that factors that contribute to azimuth dependency are not well correlated with the average σ^0 response. The responses are also much smoother reflecting the larger sample size.

Next the different sub-regions are investigated for differences in incidence dependence. The dependencies measured by NSCAT for each sub-region are shown in Table B.1. There is not much variation in the incidence dependence estimates with sub-region though there is marginally more variation amongst sub-regions divided by contiguous regions as opposed to those divided by σ^0.

The next inter-dependency is between area and season. Again the procedure is simple, select data from each region over the QuikSCAT mission, bin by time of year and then subtract out the average. Figures B.7 and B.8 show results for regions divided into contiguous areas and Figures B.9 and B.10 show results for areas divided by mean σ^0. A possible explanation for the differences seen in B.7 and B.8 is differences in local climate patterns. For example, [46] and [47] have found that the onset of the rainy season can vary by as much as six months across the Amazon. Unfortunately, the findings in these papers do not explain
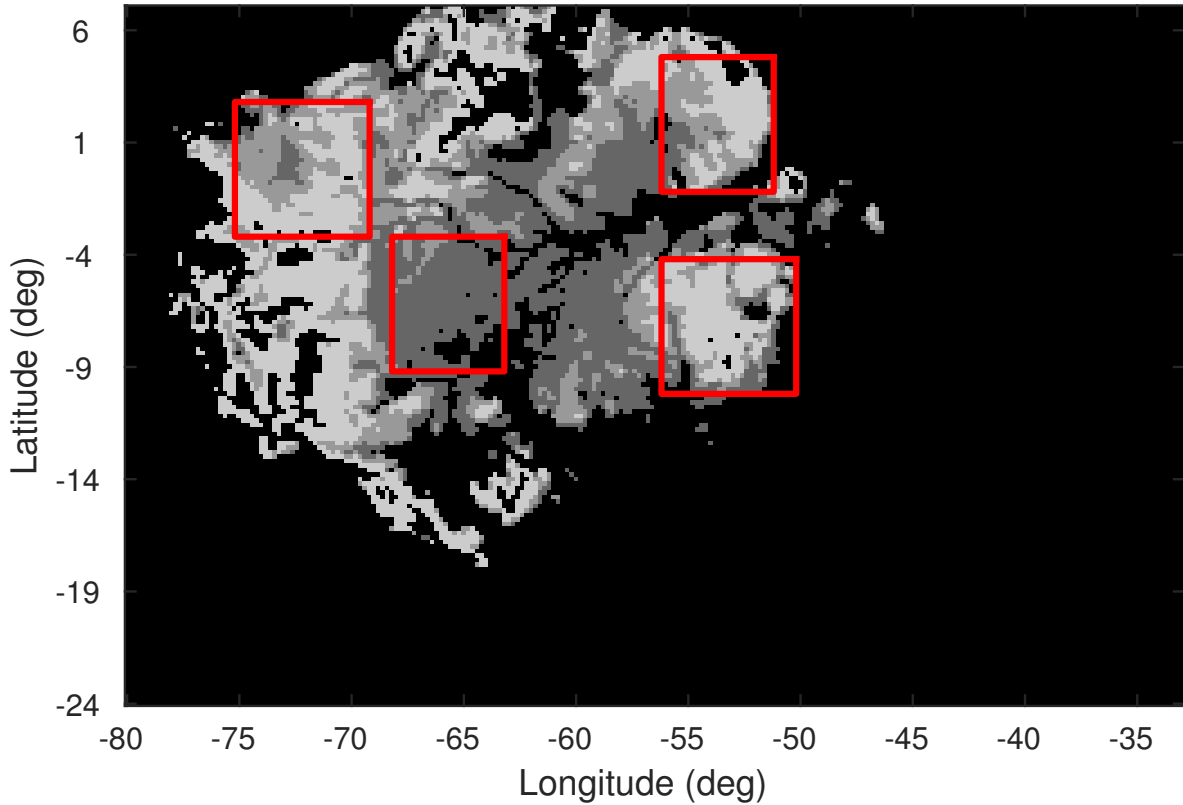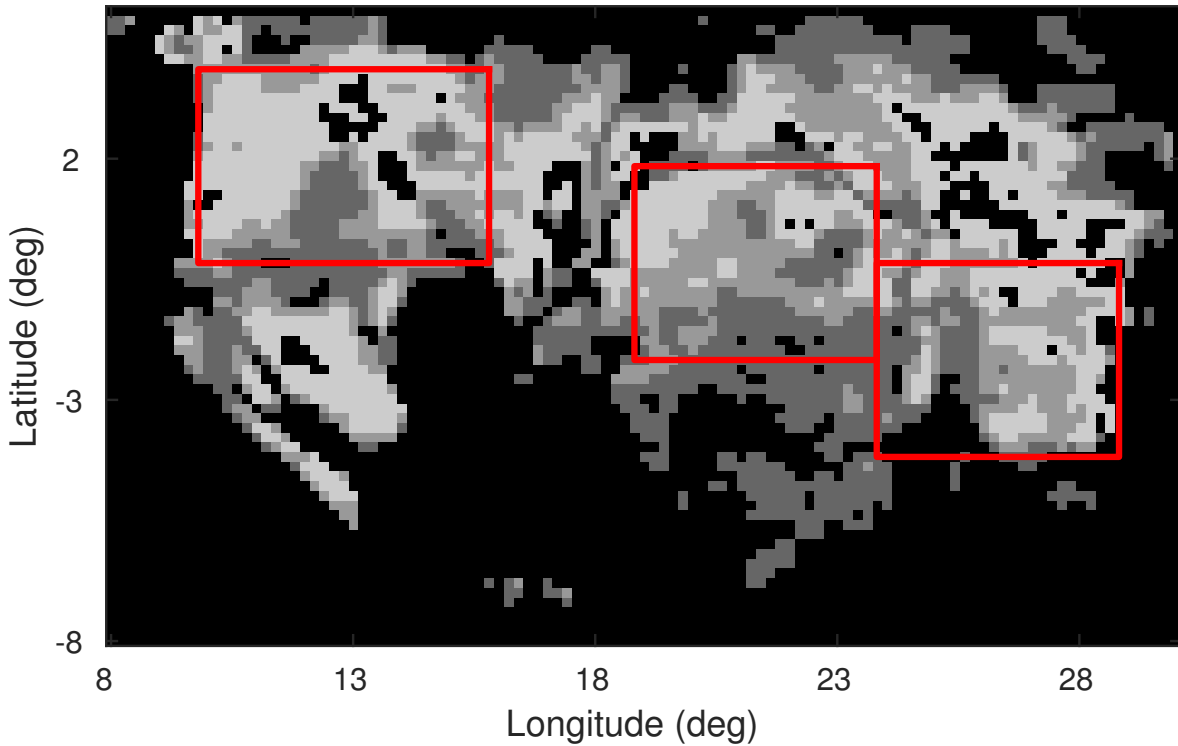
Figure B.1: Sub-masks of the Amazon. The three shades of gray indicate sub-masks based on QuikSCAT average σ^0. Darker shades indicate lower σ^0. Red boxes indicate sub-masks based on region.

Table B.1: Incidence angle dependence as measured by NSCAT for different sub-regions within the Amazon and Congo masks. Least-squares line calculated for each beam then averaged for each polarization.

Region	Sub-reg.	AscH	DesH	AscV	DesV
Ama	SE	-0.1437	-0.1213	-0.1437	-0.1482
	Cen.	-0.1421	-0.1310	-0.1447	-0.1547
	NE	-0.1239	-0.1202	-0.1389	-0.1516
	NW	-0.1384	-0.1210	-0.1518	-0.1563
	Low σ^0	-0.1384	-0.1217	-0.1405	-0.1508
	Mid σ^0	-0.1335	-0.1199	-0.1434	-0.1513
	High σ^0	-0.1340	-0.1201	-0.1437	-0.1528
Con	NW	-0.1287	-0.1283	-0.1407	-0.1584
	Cen.	-0.1071	-0.1073	-0.1212	-0.1411
	SE	-0.1140	-0.1026	-0.1265	-0.1350
	Low σ^0	-0.1177	-0.1145	-0.1266	-0.1432
	Mid σ^0	-0.1196	-0.1102	-0.1291	-0.1410
	High σ^0	-0.1218	-0.1149	-0.1361	-0.1459

Figure B.2: Sub-masks of the Congo. The three shades of gray indicate sub-masks based on QuikSCAT average σ^0. Darker shades indicate lower σ^0. Red boxes indicate sub-masks based on region.

the behavior seen in this appendix, particularly the large dip in σ^0 seen around day 230 in the Amazon for ascending passes in the southeast Amazon.

Lastly, the diurnal response for each sub-region is found using RapidScat data. Figures B.11 and B.12 show the results for sub-regions divided by location and Figures B.13 and B.14 show the results for sub-regions divided by mean σ^0. Again more variation between the regions is seen between regions based on location, though not nearly so much as seen with the seasonal variation.

Overall, dependencies on different variables differed more with the regions divided somewhat arbitrarily into rectangular regions. Sub-regions divided by σ^0 all behaved very similarly with regards to time and viewing angle. This similarity in behavior suggests that a spatial correction based off the results in Section 4.5 can be applied independently of other corrections. Another point to note is that the sub-regions based on locations also have considerably fewer samples, and so the differences in responses could partially be showing the effects of a smaller sample size.
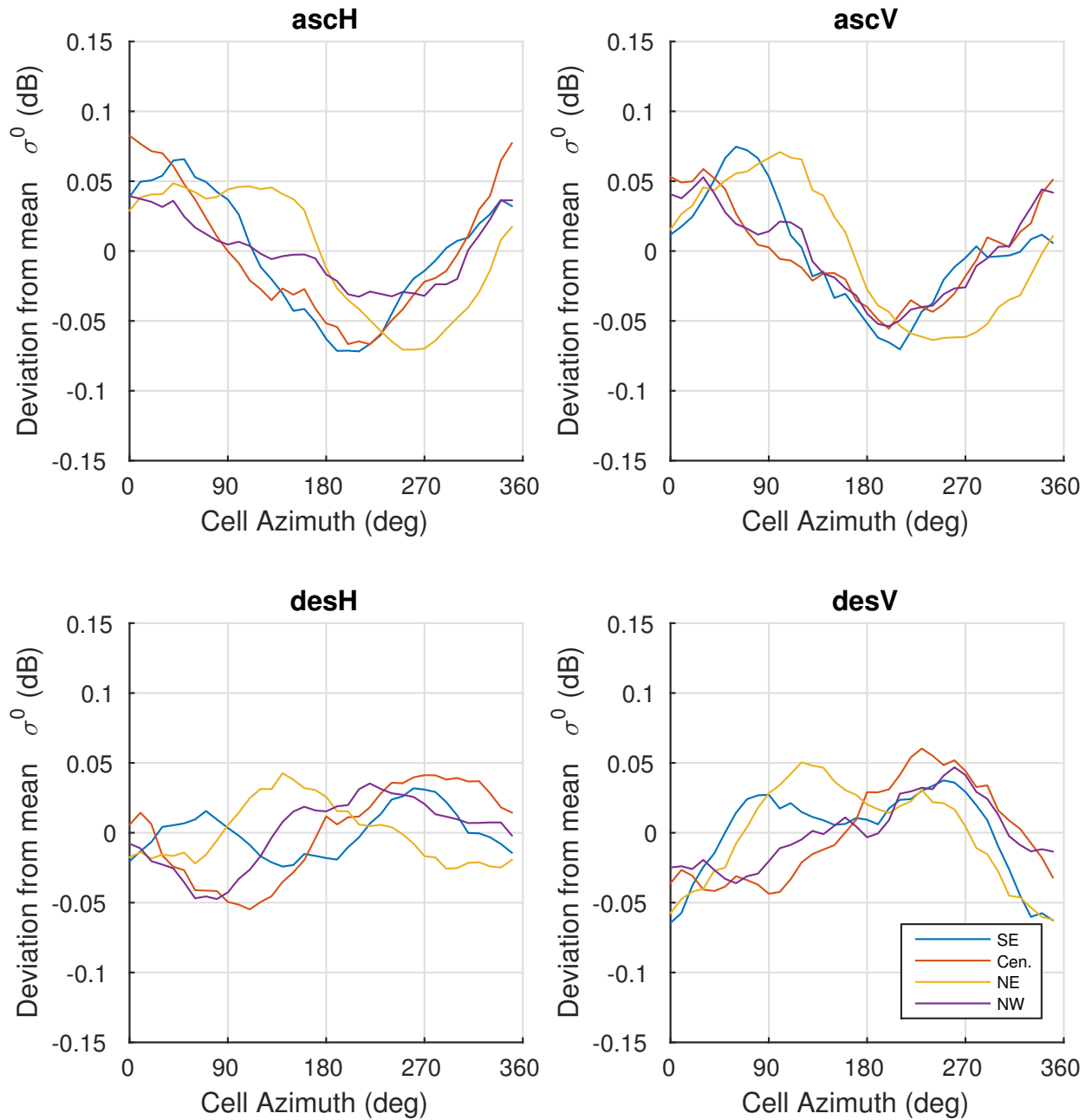
Figure B.3: Average QuikSCAT σ^0 as a function of azimuth. Each line represents a different region within the Amazon. Regions divided based on location. The average for the region is subtracted out. Azimuth angle is measured clockwise from north.
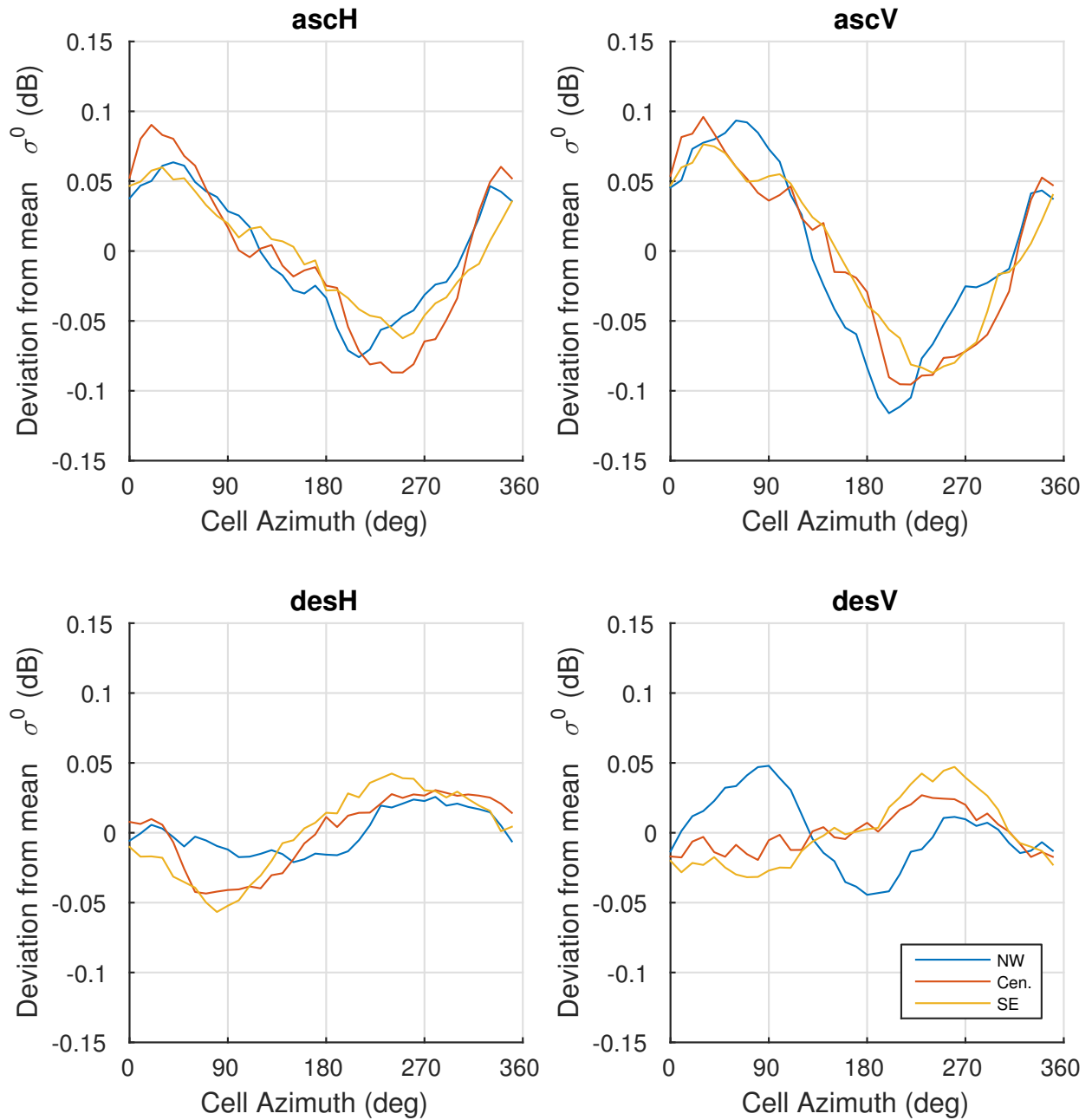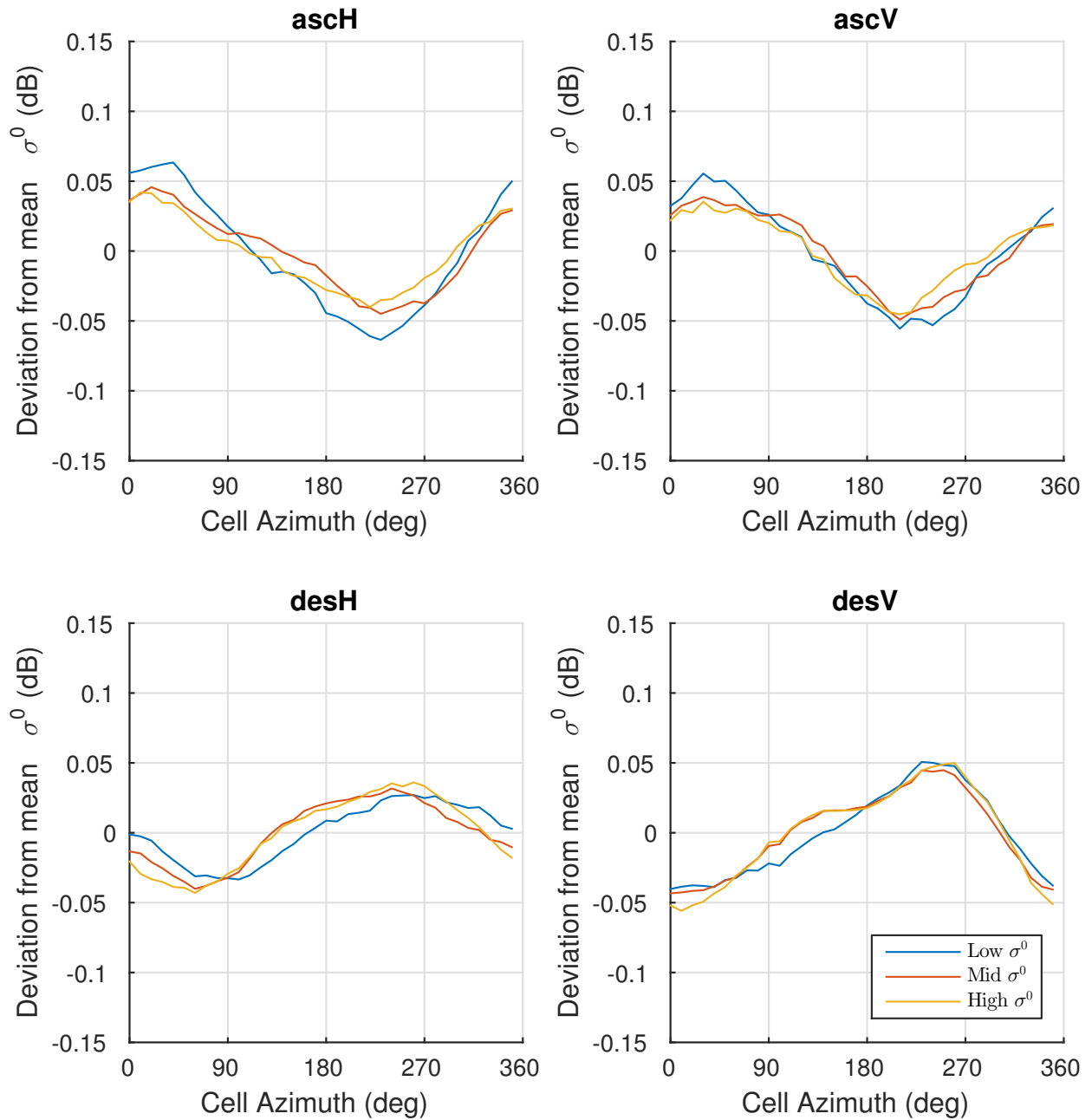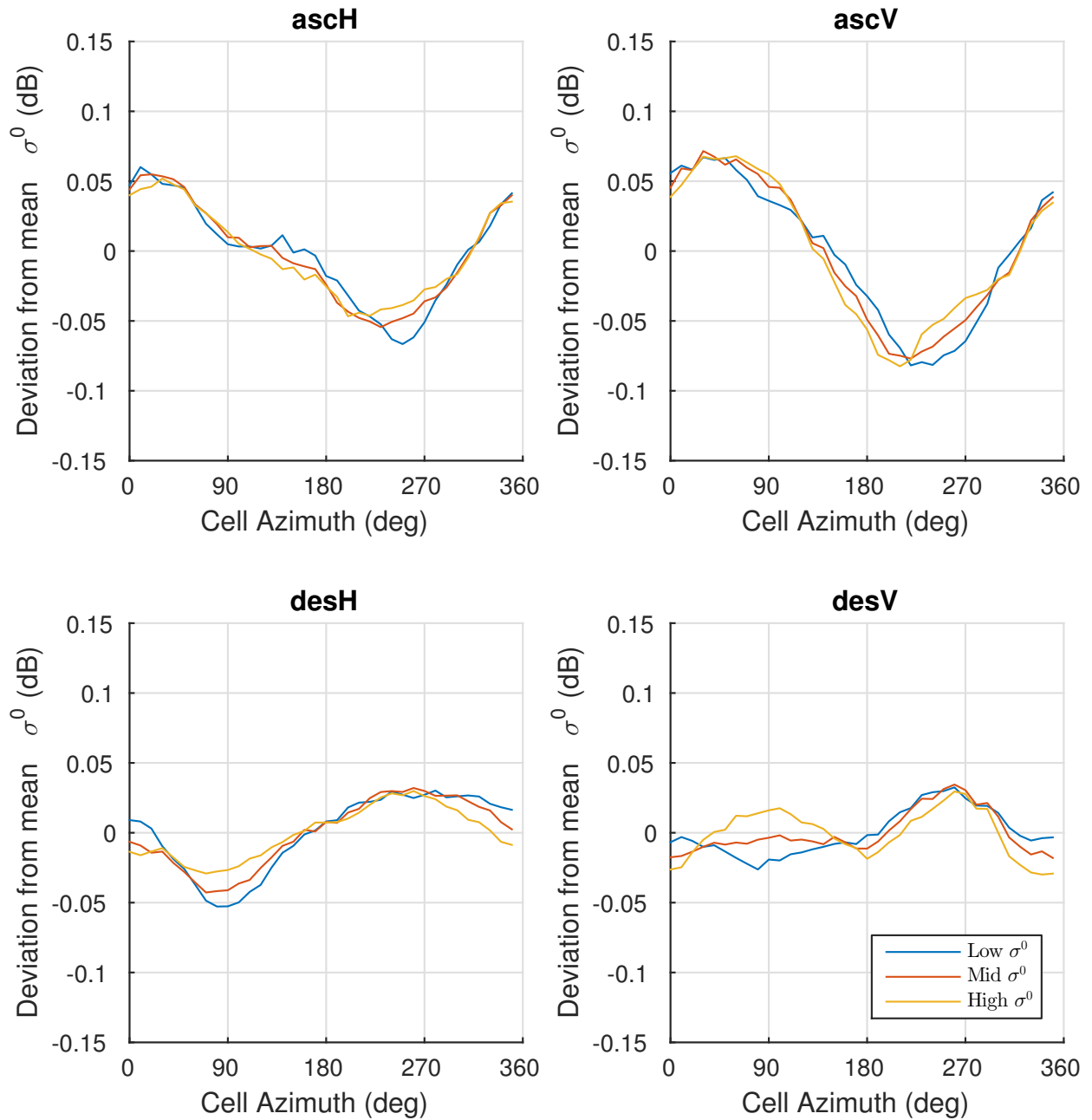
Figure B.4: Average QuikSCAT σ^0 as a function of azimuth. Each line represents a different region within the Congo. Regions divided based on location. The average for the region is subtracted out. Azimuth angle is measured clockwise from north.

Figure B.5: Average QuikSCAT σ^0 as a function of azimuth. Each line represents a different region within the Amazon. Regions divided based on mean backscatter response. The average for the region is subtracted out. Azimuth angle is measured clockwise from north.
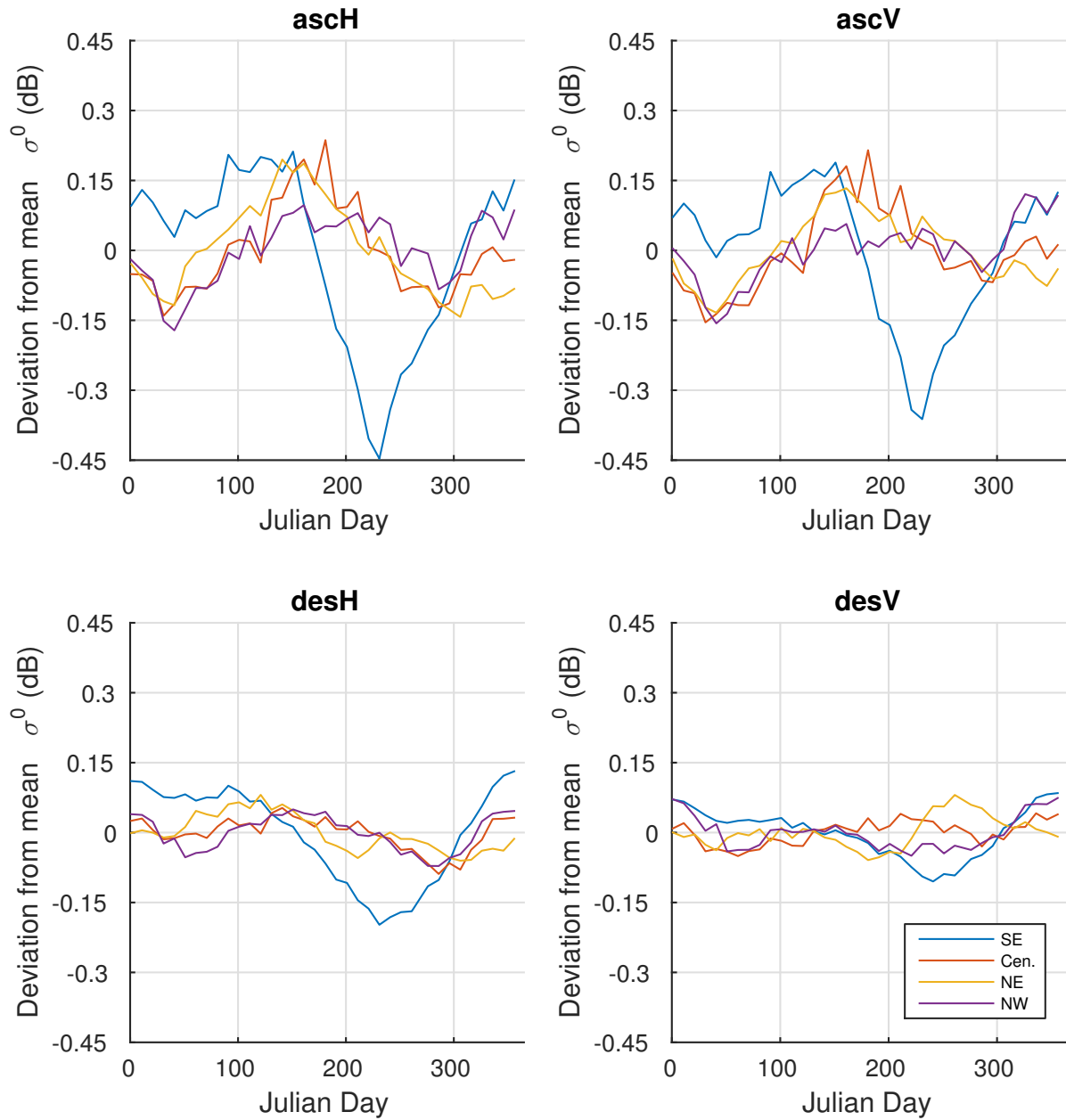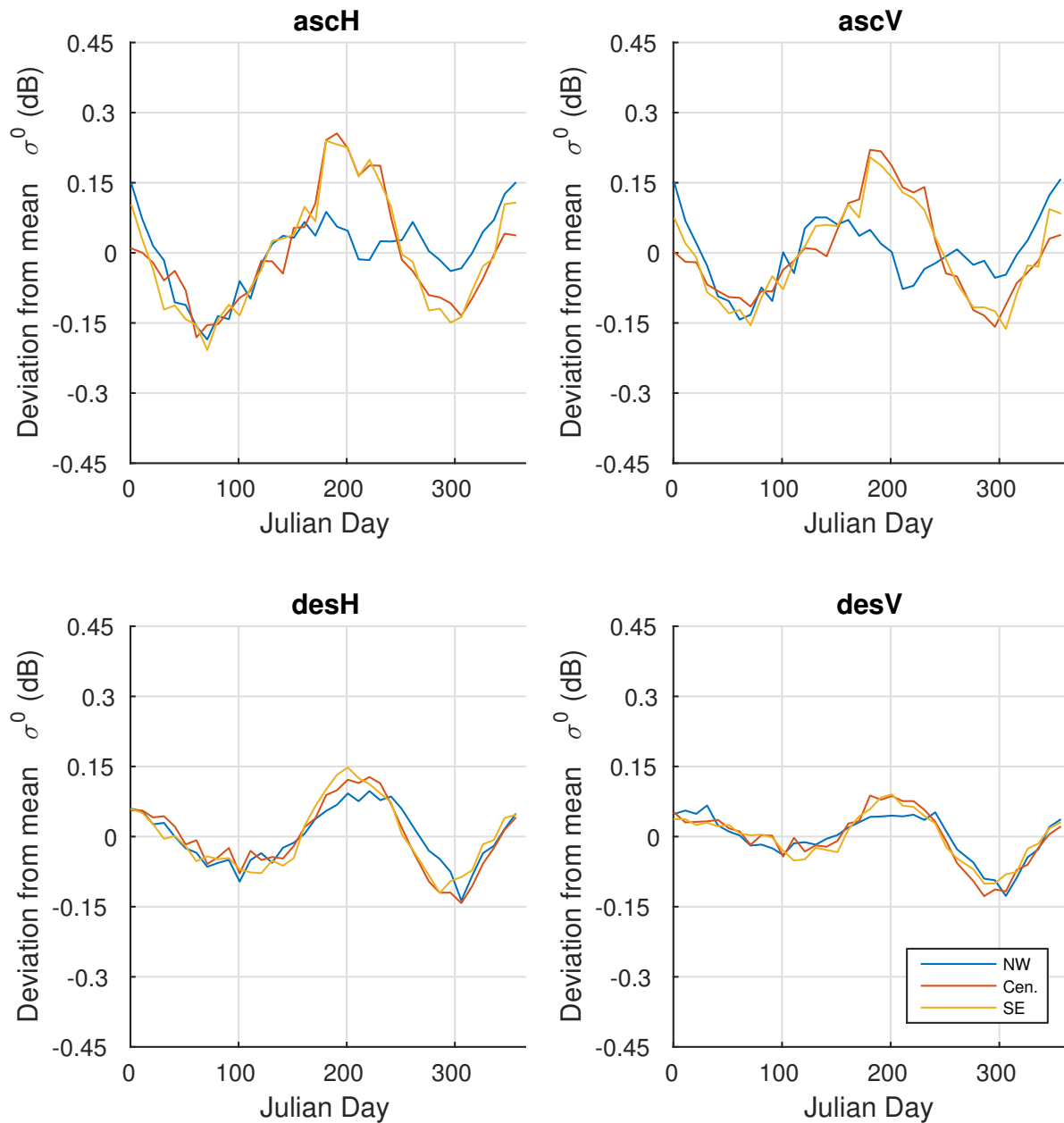
Figure B.6: Average QuikSCAT σ^0 as a function of azimuth. Each line represents a different region within the Congo. Regions divided based on mean backscatter response. The average for the region is subtracted out. Azimuth angle is measured clockwise from north.

Figure B.7: Average QuikSCAT σ^0 as a function of time of year. Each line represents a different region within the Amazon. Regions divided based on location. The average for the region is subtracted out.
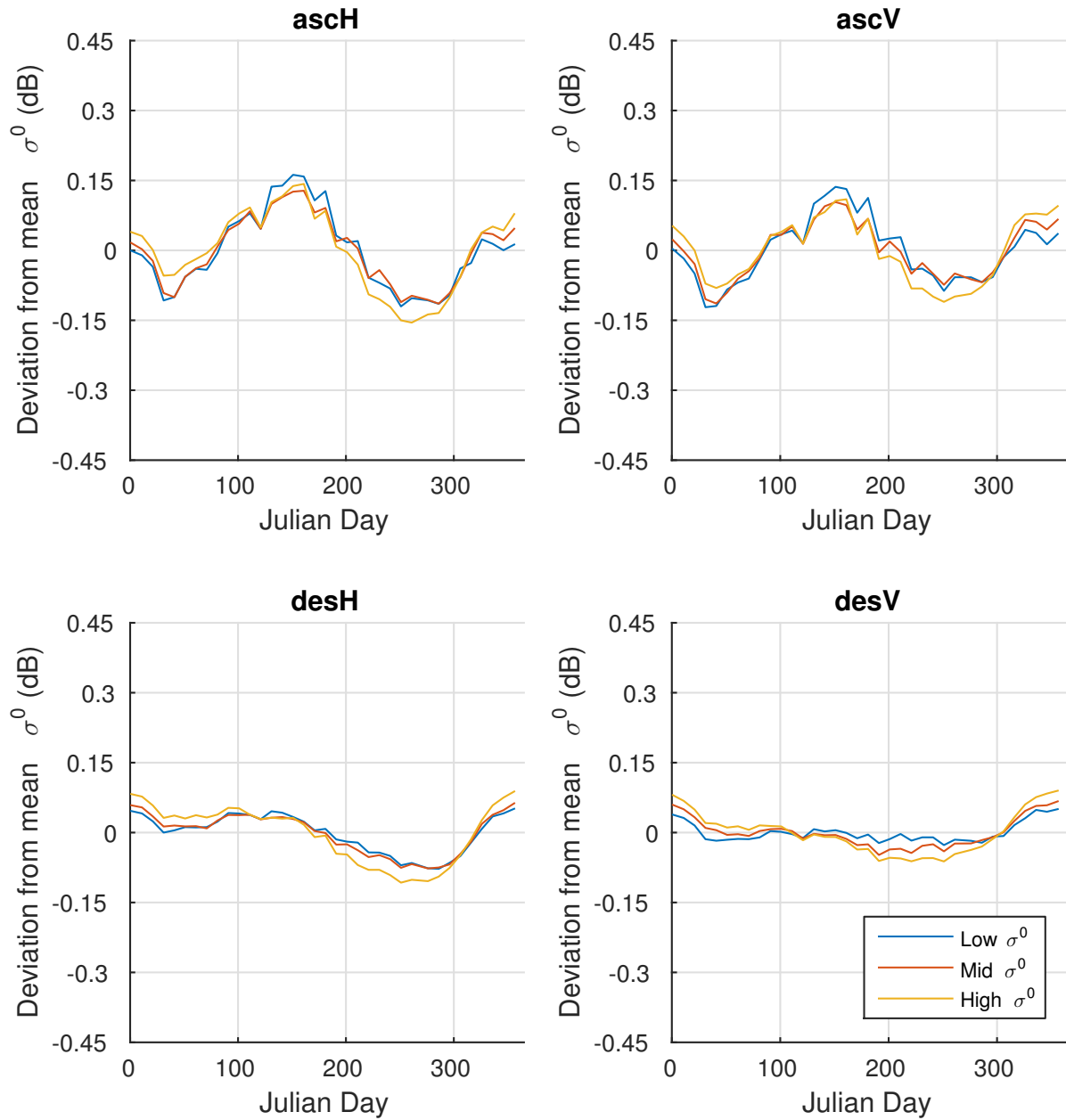
Figure B.8: Average QuikSCAT σ^0 as a function of time of year. Each line represents a different region within the Congo. Regions divided based on location. The average for the region is subtracted out.

Figure B.9: Average QuikSCAT σ^0 as a function of time of year. Each line represents a different region within the Amazon. Regions divided based on mean backscatter response. The average for the region is subtracted out.
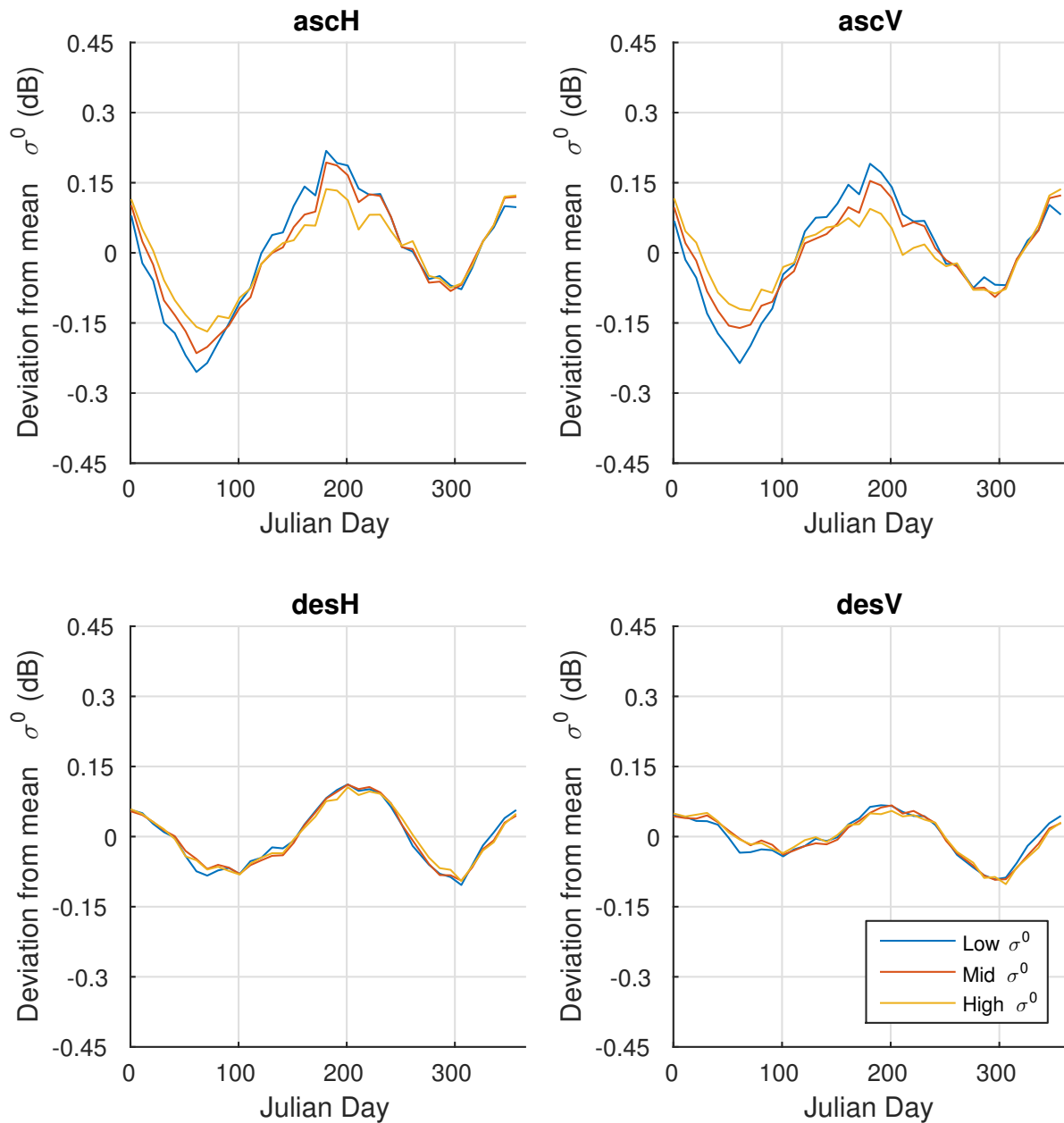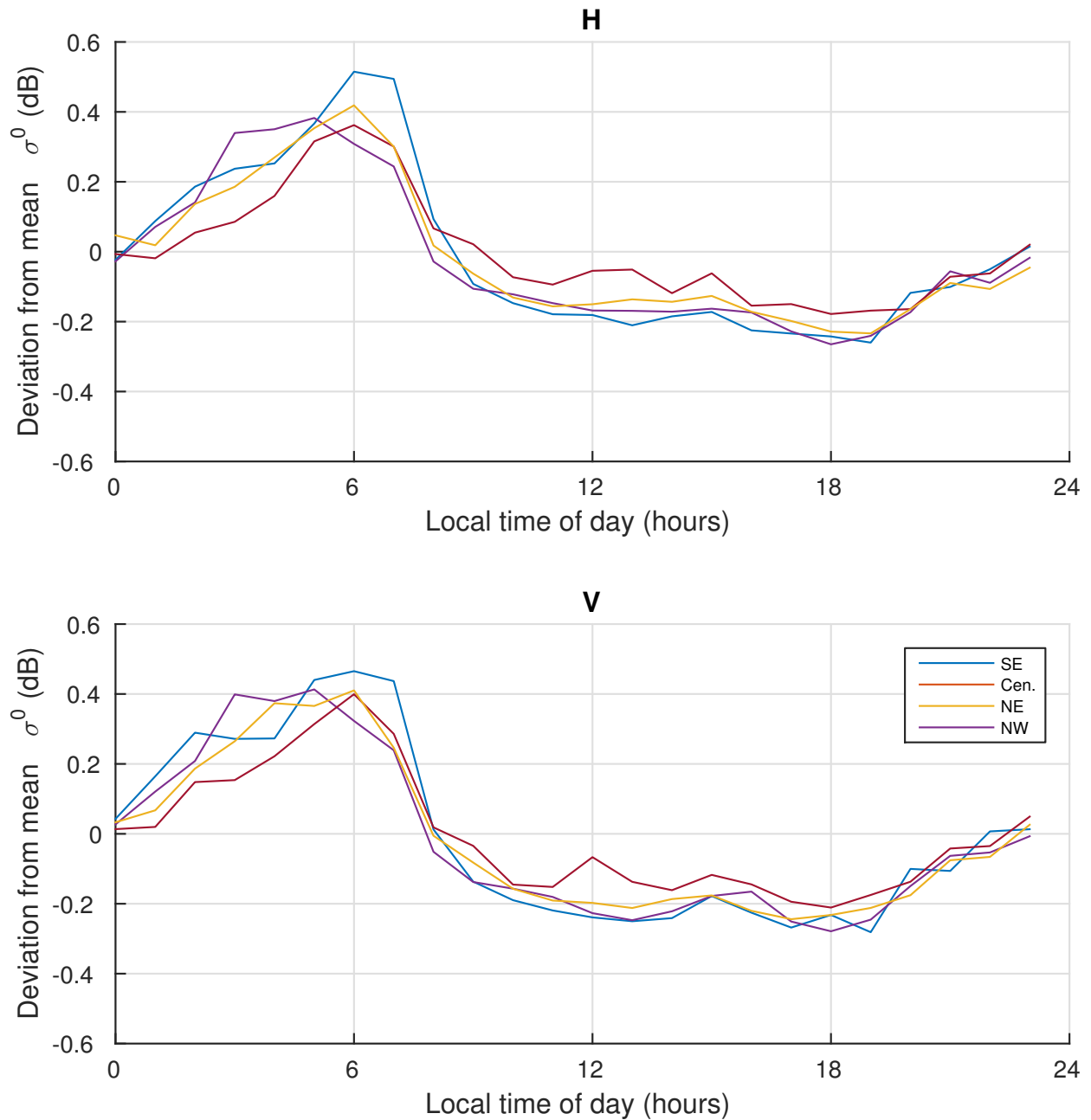
Figure B.10: Average QuikSCAT σ^0 as a function of time of year. Each line represents a different region within the Congo. Regions divided based on mean backscatter response. The average for the region is subtracted out.

Figure B.11: Average RapidScat σ^0 normalized to QuikSCAT incidence as a function of time of local time of day. Each line represents a different region within the Amazon. Regions divided based on location. The average for the region is subtracted out.
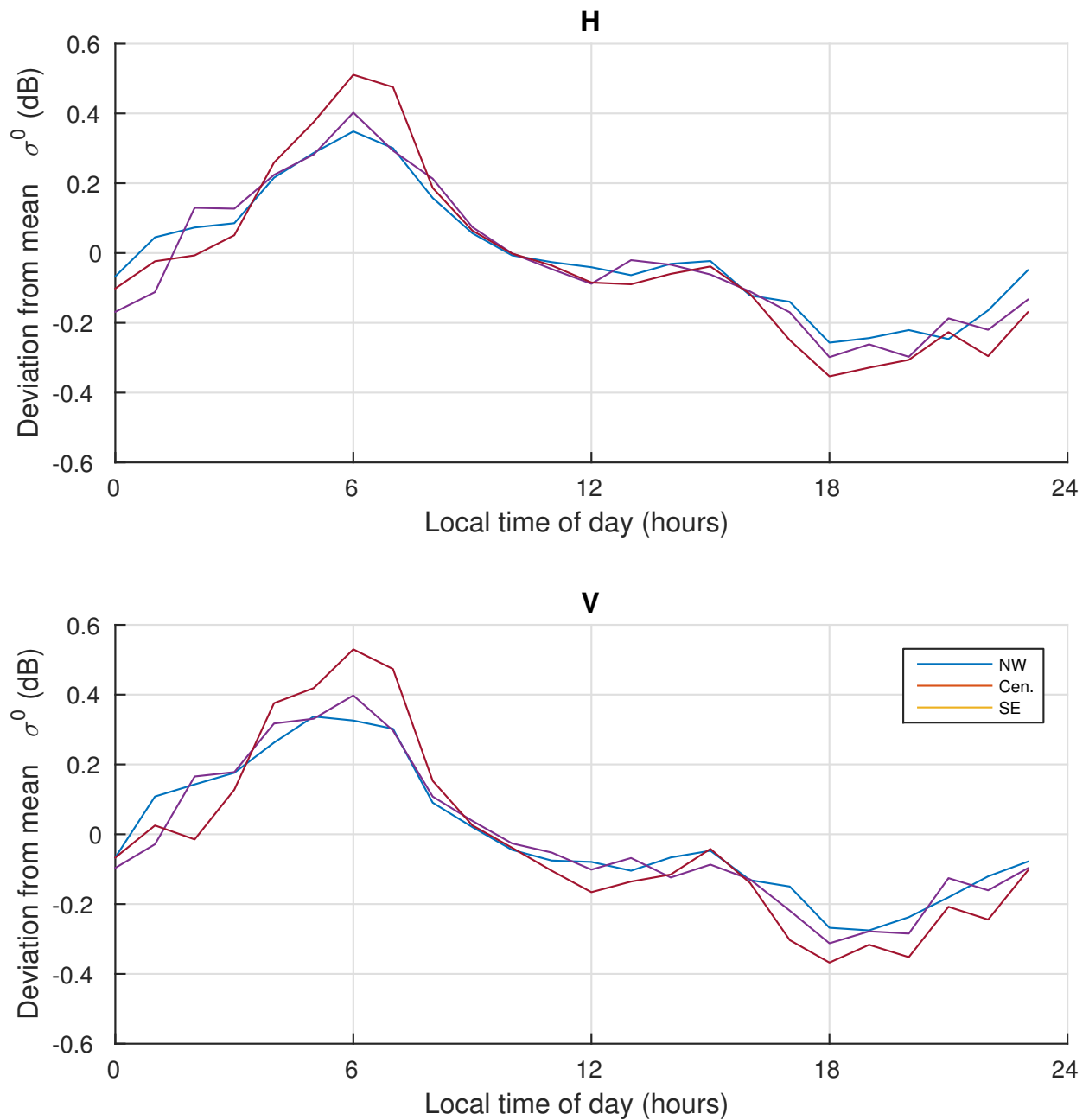
Figure B.12: Average RapidScat σ^0 normalized to QuikSCAT incidence as a function of time of local time of day. Each line represents a different region within the Congo. Regions divided based on location. The average for the region is subtracted out.
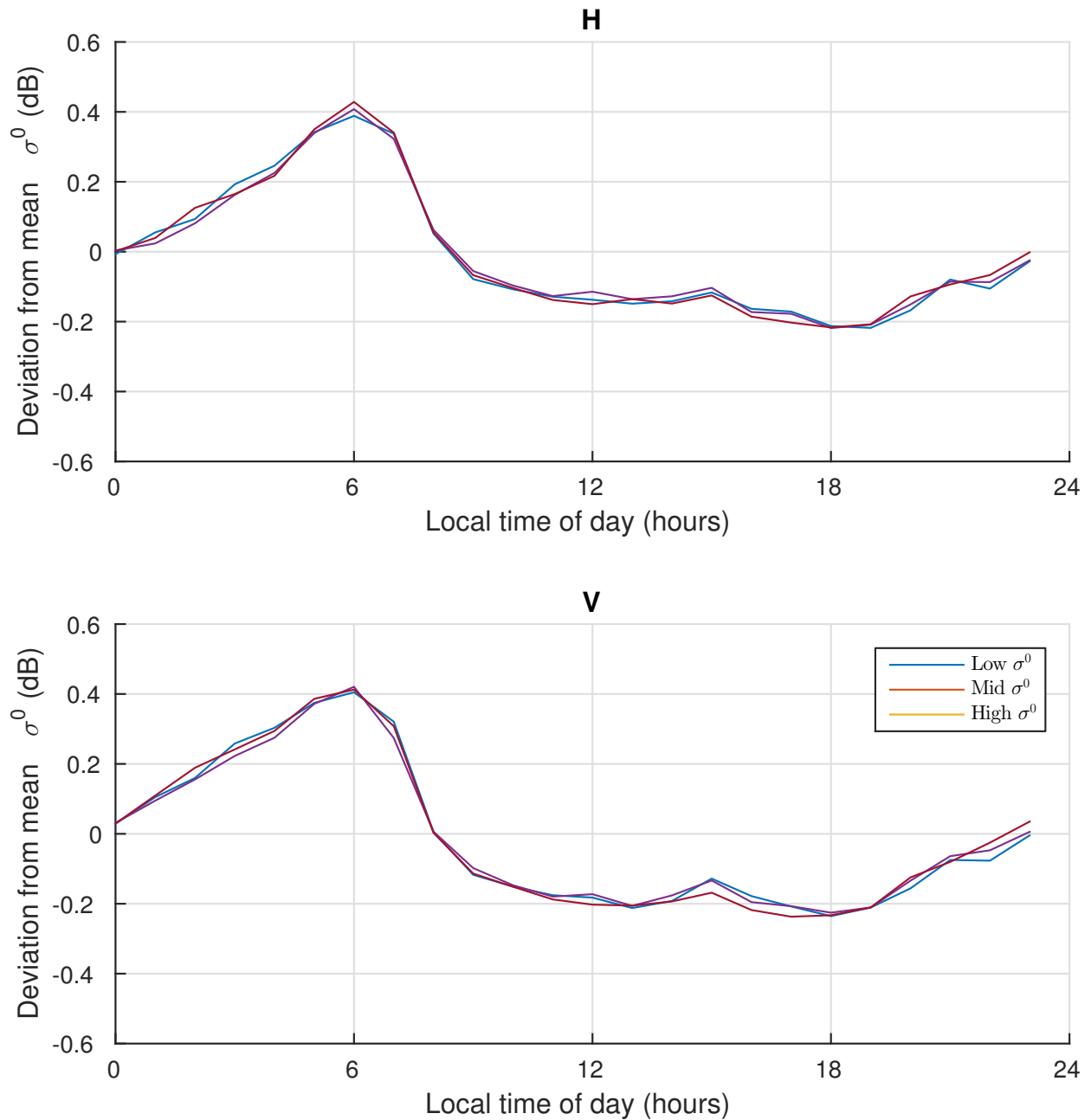
Figure B.13: Average RapidScat σ^0 normalized to QuikSCAT incidence as a function of time of local time of day. Each line represents a different region within the Amazon. Regions divided based on mean backscatter response. The average for the region is subtracted out.
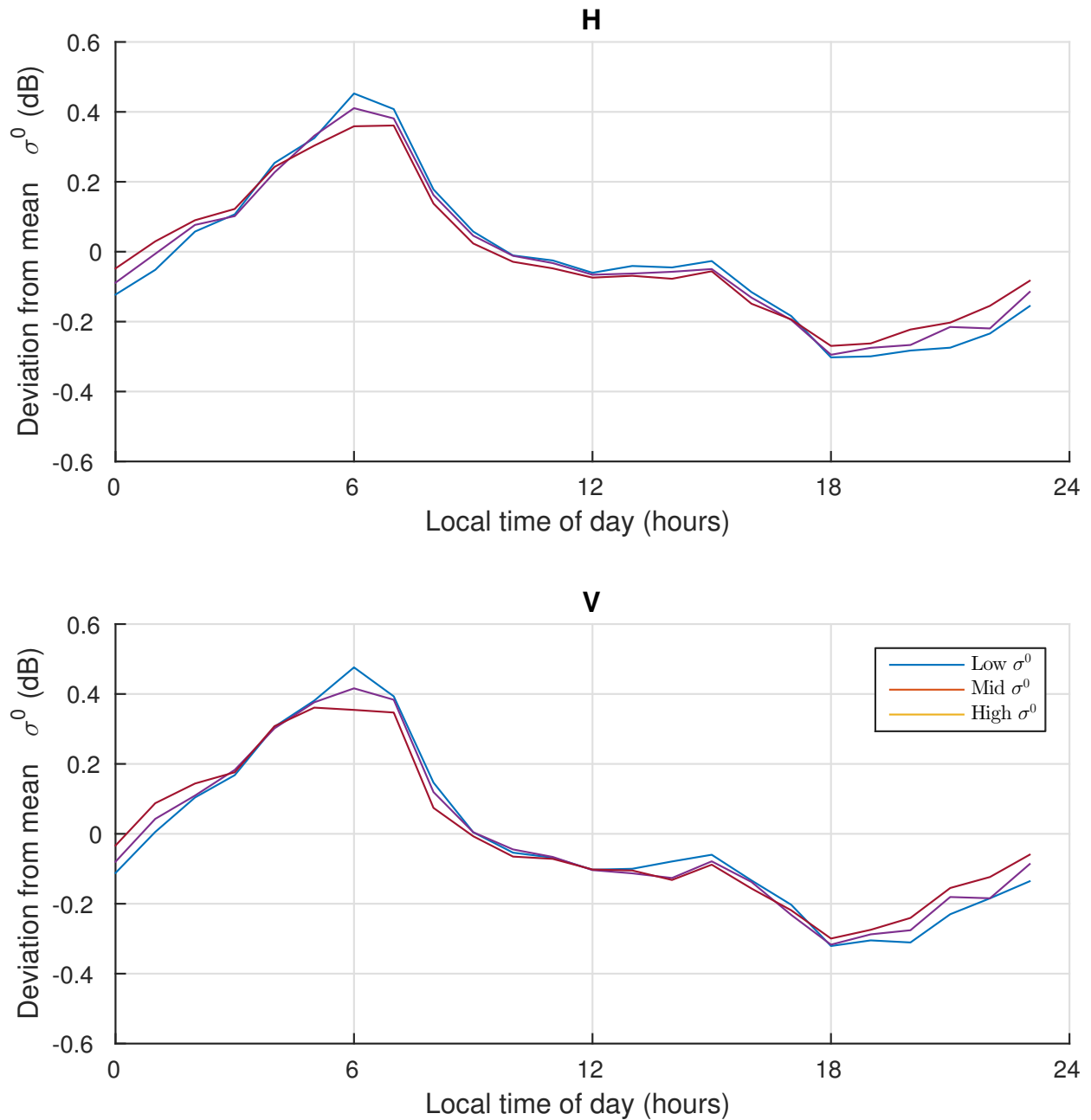
Figure B.14: Average RapidScat σ^0 normalized to QuikSCAT incidence as a function of time of local time of day. Each line represents a different region within the Congo. Regions divided based on mean backscatter response. The average for the region is subtracted out.